DOI:
10.1016/j.stem.2019.02.017

Document Version
Peer reviewed version

Neocortical expansion due to increased proliferation of basal progenitors is linked to changes in their morphology

Nereo Kalebic[1], Carlotta Gilardi[1], Barbara Stepien[1], Michaela Wilsch-Bräuninger[1], Katherine R. Long[1], Takashi Namba[1], Marta Florio[1§], Barbara Langen[1], Benoit Lombardot[1], Anna Shevchenko[1], Manfred W. Kilimann[2], Hiroshi Kawasaki[3], Pauline Wimberger[4], Wieland B. Huttner[1,5,*]

[1] Max Planck Institute of Molecular Cell Biology and Genetics, Dresden, Germany

[2] Max Planck Institute for Experimental Medicine, Göttingen, Germany

[3] Department of Medical Neuroscience, Graduate School of Medical Sciences, Kanazawa University, Ishikawa, Japan

[4] Technische Universität Dresden, Universitätsklinikum Carl Gustav Carus, Klinik und Poliklinik für Frauenheilkunde und Geburtshilfe, Dresden, Germany

[§] Present address: Department of Genetics, Harvard Medical School, Boston, USA

[5] Lead Contact

*Correspondence: huttner@mpi-cbg.de

SUMMARY

The evolutionary expansion of the mammalian neocortex (Ncx) is thought to be linked to increased proliferative capacity of basal progenitors (BP) and their neurogenic capacity. Here, by quantifying BP morphology in the developing Ncx of mouse, ferret, and human, we show that increased BP proliferative capacity is linked to an increase in BP process number. We identify human membrane-bound PALMDELPHIN (PALMD-Caax) as an underlying factor and show that it drives BP process growth and proliferation when expressed in developing mouse and ferret Ncx. Conversely, CRISPR/Cas9-mediated disruption of PALMD or its binding partner ADDUCIN-γ in fetal human Ncx reduces BP process numbers and proliferation. We further show that PALMD-induced processes enable BPs to receive pro-proliferative integrin-dependent signals. These findings provide a link between BP morphology and proliferation, suggesting that changes in BP morphology may have contributed to the evolutionary expansion of the Ncx.

INTRODUCTION

The evolutionary expansion of the mammalian Ncx is thought to underlie the increased cognitive abilities of humans. The size of Ncx is primarily determined by the developmental production of neurons, which is generally governed by the proliferative capacity of neural stem and progenitor cells (Borrell and Reillo, 2012; Dehay et al., 2015; Florio and Huttner, 2014; Lui et al., 2011; Molnar et al., 2006; Rakic, 2009; Sousa et al., 2017).

Neural progenitors can be divided into two classes: apical progenitors (APs) and basal progenitors (BPs). APs reside in the ventricular zone (VZ), are highly proliferative across mammals and upon division can generate other APs, BPs or, rarely, neurons (Götz and Huttner, 2005; Rakic, 2003).

BPs reside in the subventricular zone (SVZ) and show great variability in their proliferative capacity across mammals. In species with a small and lissencephalic (smooth) Ncx, such as mouse (embryonic mouse Ncx hereafter referred to as mNcx), BPs exhibit a low proliferative capacity, dividing typically once to generate two neurons (Haubensak et al., 2004; Miyata et al., 2004; Noctor et al., 2004). In species with an expanded and gyrencephalic (folded) Ncx, such as ferret (developing ferret Ncx hereafter referred to as fNcx) or human (fetal human Ncx hereafter referred to as hNcx), BPs are more proliferative and can undergo several cycles of proliferative divisions to generate further BPs before dividing to generate neurons (reviewed in (Florio and Huttner, 2014; Lui et al., 2011)). A specific type of BPs, called basal (or outer) radial glia (bRG), are particularly important in this context. In mouse, bRG are very rare and mostly neurogenic (Shitamukai et al., 2011; Wang et al., 2011), whereas in ferret and primates, bRG are more abundant and highly proliferative, (Betizeau et al., 2013; Fietz et al., 2010; Hansen et al., 2010; Reillo et al., 2011; Smart et al., 2002). The increased proliferative capacity of BPs, and in particular bRG, in species with an enlarged Ncx leads to SVZ expansion, resulting in the generation of two distinct zones: inner and outer SVZ (ISVZ and OSVZ) (Dehay et al., 2015; Smart et al., 2002). Thus, BPs, and particularly bRG, are considered the major progenitor cell type underlying the evolutionary expansion of the Ncx (Borrell and Reillo, 2012; Florio and Huttner, 2014; Lui et al., 2011).

BPs in ferret and primates show diverse morphologies (Betizeau et al., 2013; Reillo et al., 2017), some of which have also been observed in mNcx (Pilz et al., 2013; Wong et al., 2015). bRG were originally described as monopolar cells with a long basal process that often contacts the basal lamina (Fietz et al., 2010; Hansen et al., 2010; Reillo et al., 2011). A seminal study in macaque (Betizeau et al., 2013) has shown that bRG come in several different morphotypes and that the morphotype with an additional, apically directed, process might be more proliferative than the monopolar morphotype (Dehay et al., 2015). However, the molecular mechanisms regulating BP morphology and, in particular, its influence on the BP proliferative capacity remain largely unknown.

Here we have examined the diversity of BP morphologies in three different mammalian species, exploring whether manipulating BP morphology will result in a modification of BP proliferative capacity. We propose a mechanism of how cell morphology contributes to the proliferative capacity of neocortical progenitors.

RESULTS

Morphological heterogeneity of human proliferative BPs

We first investigated the diversity of BP morphologies in the hNcx at mid-neurogenesis. We defined a cell in the SVZ with a SOX2+ nucleus as a proliferative BP (Figures 1A, S1A). Immunofluorescence (IF) for HOPX , which was found to be present in the entire cell body and in cell protrusions (Figures 1A, S1A), enabled us to determine BP morphology.

Using these criteria, we identified 6 different morphotypes of human proliferative BPs, 5 of which were radial in morphology (constituting different bRG morphotypes) and the remaining one was multipolar (multipolar BP hereafter referred to as mBP, Figure 1A). Of the 5 radial morphotypes, 3 have been described previously (Betizeau et al., 2013; Fietz et al., 2010; Hansen et al., 2010; Reillo et al., 2011), (i) bRG with a basal process (hereafter referred to as bRG-b), (ii) bRG with an apical process (bRG-a), and (iii) bRG with both apical and basal processes (bRG-ab, Figure 1A). In addition, we also identified bRG with a bifurcated basal process (bRG-b_{bf}) and bRG with an apical process plus a bifurcated basal process (bRG-ab_{bf}). The mBPs which exhibited small processes extending in various directions also expressed markers of proliferative BPs and we, hence, refer to them as proliferative mBP (mBP-p) to collectively comprise progenitor types previously referred to as proliferative basal intermediate progenitors, transit amplifying progenitors, or transient bRG (Betizeau et al., 2013; Florio and Huttner, 2014; Lui et al., 2011). The mBP-p morphotype as well as the bRG-b_{bf} and bRG-ab_{bf} (collectively termed bRG-(a)b_{bf}) were corroborated by IF for BLBP (Figure S1B, C).

To further corroborate the bRG-(a)b_{bf} morphotypes by an independent approach, we applied DiI to the basal side of hNcx tissue. This revealed all the bRG morphotypes that exhibited contact with the basal lamina (bRG-b, bRG-ab and bRG-(a)b_{bf}, Figures 1B, S1D-G; see also supplemental movies S1-3 showing 3D representations of cells). For a more detailed cell biological analysis of the human bRG-(a)$b_{bf,}$ please refer to Figure S1H-H" and the respective figure legend. For the analysis of the morphology of 15-wpc human gliogenic progenitors, please refer to the Figure S1I-N and the respective figure legend.

In conclusion, we provide evidence for a morphological heterogeneity of human BPs that is larger than previously reported, with two additional morphotypes identified – bRG-b_{bf} and bRG-ab_{bf}. The presence of two basal processes makes these morphotypes particularly interesting in the context of the proliferative capacity of BPs, considering that a long basal process has been considered a landmark of proliferative bRG (Fietz et al., 2010; Hansen et al., 2010).

Quantitative analysis of BP morphotypes across different mammals

In light of the above observations, we (i) explored whether there were any differences in BP morphotypes between mammalian species, and (ii) sought to develop a quantitative method for analyzing BP morphology. To this end, we expressed membrane-targeted GFP (mGFP) and tracked BP morphology. We compared (i) the lissencephalic mouse with a small Ncx, (ii) the gyrencephalic ferret with an enlarged Ncx and (iii) hNcx tissue (Figure 2A-C). In both mNcx and fNcx, we performed *in utero* electroporations (IUE) of mGFP, whereas hNcx tissue was subjected to *ex vivo* electroporation of mGFP (for details including the developmental stages and markers used to identify BPs, see Methods and Figures 2A-C, S2C, D). Using the mGFP signal on 3D stacks of sufficiently thick vibratome sections, we tracked the morphology of the targeted BPs in order to generate 2D cell masks representing the cell shape, which were then used to quantify a set of morphological parameters (for details of sectioning and tracking, see Methods and Figure S2A, B).

We first examined the relative proportion of the two major morphological classes – mBPs and bRG. Whereas human and ferret exhibited a roughly similar proportion of mBPs and bRG, only 8% of the mouse BPs were bRG (Figure 2D), which was consistent with previously published data for mNcx (Wang et al., 2011; Wong et al., 2015).

Next, we analyzed the morphology of mBPs in all three species. Human mBPs exhibited more primary processes (i.e. those that originate from the cell body) than mouse mBPs. Furthermore, human mBPs had significantly more of all processes (primary processes plus their branches) than mouse and ferret (Figure 2E). The branching index, calculated as the number of all processes divided by the number of primary processes, was also increased between mouse and human (Figure S2E).

We then analyzed the morphology of bRG. Distinguishing between the 5 bRG morphotypes (see Figure 1A) we observed significant differences in their distributions across the 3 species (Figure 2F). Additionally, when collectively quantifying bRG morphotypes with two or more processes vs. bRG with a single process, hNcx and fNcx showed a significantly higher proportion of the former than mNcx (see Methods for details). All 5 bRG morphotypes originally described using SOX2 and HOPX IF (see Figure 1A) were confirmed in the hNcx by mGFP tracking, and no additional morphotypes were identified (for examples of a bRG-b_{bf}, see Figure 2C', C'', supplemental movie S4; Figure S2F). Quantification of human bRG morphotypes using HOPX and SOX2 IF (Figure S2G) showed very similar distribution to the one obtained using mGFP tracking (see Figure 2F right). Interestingly, all 5 bRG morphotypes were also detected in fNcx, albeit at different proportions compared to hNcx, but not in mNcx, which by mGFP tracking appeared to lack bRG-(a)b_{bf} (Figure 2F). We corroborated the latter finding by IF for Sox2 and Hopx in mNcx (Figure S2H-J). Of note, the occurrence of specific bRG morphotypes does not appear to be linked to specific phases of the cell cycle, as the same morphotypes in similar relative proportions were found in mitotic and interphase bRG (Figure S2K-N).

We also examined the number of radial processes per single bRG (irrespective of morphotype) in mNcx, fNcx and hNcx (Figure 2G). bRG in hNcx exhibited a greater average number of radial processes than bRG in fNcx and mNcx. In addition to the radial processes, we detected a number of smaller protrusions of bRG, previously termed lamellate expansions (Rakic, 1972; Reillo et al., 2017) in hNcx and fNcx, but not mNcx (Figures 2C'', S2O, P).

Taken together, these data indicate an increase (i) in the diversity of BP (especially bRG) morphotypes and (ii) in the number of processes that BPs grow, from mouse to ferret to human. This is particularly interesting for bRG in light of the differences across species in bRG proliferative capacity, which are thought to underlie the evolutionary expansion of the Ncx (Florio and Huttner, 2014; Lui et al., 2011).

Cellular distribution and subcellular localization of the morpho-regulatory protein PALMDELPHIN (PALMD)

We then sought to identify molecular players that might govern BP morphology. To this end, we examined the published transcriptome dataset from hNcx (Fietz et al., 2012) and searched for genes (i) whose expression is enriched in the SVZ compared to VZ and cortical plate (CP), and (ii) whose protein product might have a morpho-regulatory role. This way we identified *PALMDELPHIN* (*PALMD*) (Figure 3A, Table S1; see Methods for details and Figure S3A for *Palmd* mRNA expression), a gene whose protein product belongs to the paralemmin family of morpho-regulatory proteins. Paralemmins have been shown to be implicated in the control of cell shape, neurite growth and filopodia extension (Arstikaitis et al., 2008; Hu et al., 2001; Kutzleb et al., 1998). Previous studies on Palm1, the founding member of this family, suggest that these functions depend on its attachment to the plasma membrane (PM) (Kutzleb et al., 1998). Expression of the Palmd protein (Figure S3B-D) in mNcx, fNcx and hNcx was consistent with the published mRNA expression pattern.

In all three species the *Palmd* gene is predicted to give rise to two mRNA splice variants (Hu et al., 2001) that we term *Palmd-CaaX* and *Palmd-KKVI*, corresponding to the 4 C-terminal amino acid residues. Palmd-CaaX shares the CaaX box with Palm1, which has been shown to be attached to the PM via CaaX box-dependent palmitoylation (Gauthier-Campbell et al., 2004; Hu et al., 2001). This in turn suggests that Palmd-CaaX may also be PM-bound. In contrast, Palmd-KKVI is not likely to exhibit a PM localization. Examination of the transcriptome dataset from mNcx and hNcx (Florio et al., 2015) revealed that in hNcx both isoforms are expressed in roughly equal amounts, whereas in mouse only the *Palmd-KKVI* mRNA exhibits robust expression (Figure S3E).

To investigate the subcellular localization of the human PALMD protein isoforms, we generated three different constructs encoding human PALMD-CaaX, PALMD-KKVI and PALMD-Δ, which is a truncated version of human PALMD lacking the 14 C-terminal residues (Figure 3B), and expressed these proteins in mouse EpH4 cells. PALMD-CaaX showed a clear association with the PM, whereas PALMD-KKVI and PALMD-Δ exhibited a cytoplasmic localization (Figure 3C, D).

We next examined the subcellular localization of the endogenous Palmd protein in the SVZ cells of mNcx and hNcx by electron microscopy (EM). In mNcx (Figure 3E left) we detected

Palmd in the cytoplasm. In hNcx (Figure 3E right), in addition to cytoplasmic localization, we detected PALMD at the PM, particularly on cell processes. We corroborated these data by IF analysis (see Figure S3F, G for details).

Taken together, these data suggest that the expression levels of the Palmd-CaaX, which in contrast to the Palmd-KKVI is characteristically associated with the PM, are higher in the SVZ of species with a greater abundance of BPs extending numerous processes. We therefore chose to examine the potential ability of human PALMD-CaaX to induce BP process growth.

PALMD-CaaX induces BP process growth in mNcx and fNcx

We performed IUE of human PALMD-CaaX along with mGFP in E13.5 mNcx and observed a subcellular localization pattern reminiscent of association with PM (Figure S3H). We identified BPs by Ki67 IF (Figure 3F) and examined the effects of PALMD-CaaX on mouse BP morphology. The proportion of mBP and bRG was not altered (Figure S3I). However, we detected a marked increase in the number of both primary and total mBP processes upon IUE of PALMD-CaaX (Figure 3G), which was accompanied by an increase in mBP process branching (Figure S3J). In contrast, no significant differences were found when analyzing bRG radial processes (Figure 3H). Both, a Sholl analysis and measuring the length of mBP processes, revealed that the PALMD-CaaX predominantly induced short process (Figure S3K, L).

We then examined the ability of PALMD-CaaX to induce bRG process growth in a potentially more conducive environment by expressing it in the fNcx (Figure S3M, N). Indeed, PALMD-CaaX changed the distribution of bRG morphotypes in fNcx (Figure 3J, see Figure 3I for an example of a bRG-b_{bf}), rendering it similar to the distribution in hNcx (see Figure 2F right). Furthermore, quantification of BP processes revealed an almost 2-fold increase in both mBP and bRG process numbers (Figure 3K, L) and mBP branching index (Figure S3O). These findings indicate that in contrast to mNcx, PALMD-CaaX is sufficient to increase bRG processes in fNcx. Of note, PALMD-CaaX did not induce new radial process of APs in either mNcx or fNcx (Figure S3P), suggesting that this increase is specific to BPs.

Comparing the effects of PALMD-CaaX, PALMD-KKVI and PALMD-Δ in mNcx, we found that the latter two were not able to increase the number of BP processes (Figure 3M), indicating

that the ability to elicit this feature is specific for PALMD-CaaX. Finally, analysis of mitotic mBPs (using PhVim IF) in mNcx revealed that the PALMD-CaaX–induced processes persisted through mitosis (Figure 3N). PALMD-CaaX caused a four-fold increase in mitotic mBP processes (Figure 3O), which appeared to be short and relatively thin (Figure S3Q). Furthermore, analysis of the morphology of mitotic BPs (identified by PH3 IF) in fNcx upon IUE of PALMD-CaaX revealed a marked increase in the number of processes of mitotic mBPs and bRG (Figure 3P-S).

Taken together, these data show that PALMD-CaaX is sufficient to induce BP processes in both mNcx and fNcx. Importantly, only the PM-bound isoform of PALMD was able to induce such processes.

PALMD-CaaX promotes BP proliferation in mNcx and fNcx

In light of the above findings (see Figures 2 and 3), we examined BP proliferation upon PALMD-CaaX expression in mNcx. IF for PhVim and Ki67 of E15.5 mNcx (Figure S4A), revealed a specific increase in basal mitoses (PhVim+ cells, Figure 4A) and a marked increase in the proportion of cycling BPs (Ki67+ cells, Figure 4B) upon PALMD-CaaX IUE. These findings were further corroborated by analysis of cell cycle re-entry using a single EdU pulse at E14.5 followed by an IF analysis for Ki67 at E15.5, which revealed a doubling of BP cell cycle re-entry upon IUE of PALMD-CaaX (Figure 4C, D). These data indicated that IUE of PALMD-CaaX induces mouse BPs to undergo repeated cycles of cell divisions (likely symmetric proliferative ones), as opposed to their typical single, differentiative cell division (Haubensak et al., 2004; Miyata et al., 2004; Noctor et al., 2004).

We also examined BP proliferation in the fNcx and found an increase in the number of basal mitoses upon IUE of PALMD-CaaX, as revealed by both PhVim (Figure 4E, F) and PH3 IF (Figure S4B, C). This increase pertained also to bRG (Figure 4G), indicating that in fNcx, in contrast to mNcx, human PALMD-CaaX is able to promote the generation of bRG.

We then compared the effects on BP proliferation upon IUE of PALMD-CaaX, PALMD-KKVI and PALMD-Δ in the mNcx. Strikingly, only PALMD-CaaX was able to elicit a specific increase in basal mitoses (Figures 4H, I, S4D). Taken together, IUE of PALMD induced BP processes and

promoted BP proliferation in mNcx and fNcx, and both of these phenotypes were specific to the PM-bound PALMD-CaaX isoform.

Palmitoylation of PALMD-CaaX is required for the increase in BP processes and proliferation

We next investigated if these two PALMD-CaaX–elicited phenotypes reflected two independent actions of the PALMD protein, or one primary action which in turn led, as a consequence, to the second one. To this end we first analyzed the mNcx 16 h after IUE of PALMD-CaaX and found an increase in the number of BP processes (Figure 5A, C left), but did not see a significant effect on BP proliferation as revealed by IF for Ki67 (Figure 5A, D left). These data suggest that the PALMD-CaaX–induced increase in BP processes precedes the PALMD-CaaX–promoted increase in BP proliferation.

Paralemmins are known to attach to the PM via palmitoylation (Arstikaitis et al., 2008; Gauthier-Campbell et al., 2004). To block protein palmitoylation including that of PALMD-CaaX, we isolated mNcx hemispheres 16 h after IUE of PALMD-CaaX and incubated them for 24 h *ex vivo* in the presence or absence of the palmitoylation inhibitor 2-bromopalmitate (2BrPal) (Figure 5B and see Methods). In the absence of 2BrPal, the PALMD-CaaX–expressing hemispheres maintained the increase in mBP process number (Figure 5C middle), which was now followed by increased BP proliferation (Figure 5D middle). In contrast, upon 2BrPal treatment, not only was the increase in mBP process number reverted to control levels (Figure 5C right), but also no increase in BP proliferation occurred (Figure 5D right). These data provide further evidence that PALMD-CaaX palmitoylation, and hence its PM attachment, are essential for the PALMD-CaaX–induced increase in BP process number and proliferation. They are also consistent with the notion that the increase in BP proliferation is a consequence of the increase in BP process number.

We then investigated the general relevance of protein palmitoylation, including that of endogenous PALMD-CaaX, for BP process growth and proliferation in hNcx by *ex vivo* incubation with 2BrPal (Figure 5E and see Methods). Although 2BrPal treatment did not change the distribution of bRG morphotypes (Figure S5A), protein palmitoylation was found to be required to maintain the normal levels of mBP process number and of cycling BPs in hNcx tissue (Figure 5F, G).

PALMD ablation in hNcx reduces BP process number and proliferation

We asked if the endogenously expressed PALMD was required for the maintenance of the BP processes in hNcx. To this end, we employed the CRISPR/Cas9 technology and successfully disrupted the expression of the *PALMD* gene (hereafter referred to as PALMD KO) in 10-13–wpc hNcx tissue *ex vivo* (for details of the KO design, see Figure S5B, C, and Methods; for the efficiency and details of the *ex vivo* manipulation, see Figure S5D-H and Methods).

Analysis of the BP morphotypes in hNcx revealed that PALMD KO did not affect the proportion of mBP and bRG (Figure S5I), but clearly affected the proportions of distinct bRG morphotypes (Figure 5I). Specifically, we detected an increase in the proportion of bRG-b, at the expense of morphotypes with two and more processes. Furthermore, the number of mBP processes was reduced (Figure 5J), as was the number of radial processes of bRG (Figure 5K). The branching index of mBPs was not affected in a statistically significant manner (Figure S5J). Taken together, these data indicate that the depletion of the endogenous PALMD is sufficient to reduce the number of BP processes, in turn implying that PALMD is an essential factor for maintaining the normal level of such processes.

In light of this, we investigated the potential effect of PALMD KO on human BP proliferative capacity, by quantifying the proportion of progenitors (PCNA+ cells) among the Cas9+ abventricular cells (all Cas9+ cells without contact to the ventricle, see Figure 5H). PALMD KO resulted in a significant reduction of PCNA+ abventricular cells (Figure 5L). Hence, PALMD is also an essential factor for maintaining the normal level of cycling BPs.

Palm1, in contrast to PALMD-CaaX, is not essential for BP process number and proliferation

Our results on the lack of effect of a Palm1 KO on BP process number and proliferation in mNcx, described in detail in Figure S6A-D, indicate that the human PALMD-CaaX–induced BP process growth and proliferation are specific to this member of the paralemmin family.

PALMD is complexed with adducin 3

We next sought to obtain mechanistic insight into how PALMD-CaaX elicits the increase in BP process number. Immunoprecipitation (IP) of PALMD under stringent conditions from hNcx

tissue followed by mass spectrometry (MS) (Figure 6A, Table S2) revealed that PALMD specifically interacts with proteins that anchor the actin cytoskeleton to the PM, in particular adducins (Kiang and Leung, 2018). Among the adducins, only *Add3* (adducin-γ) shows an mRNA expression pattern in mNcx and hNcx that resembles that of *Palmd* mRNA (see Figure S6E for details, and compare to Figure S3A). Consistent with this, IF for Add3 showed prominent presence in fNcx, but not mNcx (Figure S6F, G). Complementing these observations, we found Add3 to be present in IP of Palmd from fNcx, but not from mNcx (Figure 6A, Table S2).

We sought to further corroborate the existence of a PALMD-ADD3 complex by performing IP of either PALMD or ADD3 under stringent conditions from hNcx tissue. Indeed, we detected PALMD upon ADD3 IP and ADD3 upon PALMD IP (Figures 6B, S6H). Collectively, our data indicate the existence of a Palmd-Add3 complex in hNcx and fNcx, but not mNcx. In light of the function of Add3 to anchor the actin cytoskeleton to the PM, this complex likely exerts a key role in the PALMD-CaaX–induced BP process growth.

We examined a potential role of ADD3 itself in BP process growth and proliferation, by performing a CRISPR/Cas9-mediated KO of *ADD3* in hNcx tissue (Figures 6C, S6I, J, see Methods for details). ADD3 KO resulted in an altered distribution of bRG morphotypes (Figure 6D) which was essentially similar to the one obtained after the PALMD KO in hNcx tissue (see Figure 5I). Furthermore, ADD3 KO resulted in reduction not only of the number of mBP processes (Figure 6E), but also in the level of cycling BPs (Figure 6F), again very similar to what we had observed upon PALMD KO in hNcx tissue. Taken together with our observation that membrane attachment of PALMD-CaaX is required for BP process growth (Figure 3M) and proliferation (Figure 4I), these data show that a PALMD-CaaX/ADD3 complex underlies these two phenotypes in hNcx.

PALMD-CaaX expression results in an increase in upper-layer (UL) neurons

We next explored putative effects of PALMD-CaaX on UL neurons, whose increase is considered a hallmark of the evolutionary expansion of Ncx (Molnar et al., 2006; Rakic, 2009; Sousa et al., 2017). We expressed PALMD-CaaX and GFP in mNcx at E13.5 and analyzed the CP at E18.5 by IF for a neuronal marker Satb2, present in UL neurons (Britanova et al., 2008;

Leone et al., 2015) (Figure 6G). The analysis showed an altered distribution of both GFP+ and Satb2+ GFP+ cells, with an increase in proportion of these cells in ULs (Figure 6H, I). Moreover, the proportion of GFP+ cells that were Satb2+ was also increased upon IUE of PALMD-CaaX (Figure 6J). In line with this, we detected an increase in thickness of the ULs of the CP (Figure 6K). Hence, human PALMD-CaaX is able to elicit a hallmark of the evolutionary expansion of the Ncx when expressed in mNcx.

PALMD-CaaX promotes BP proliferation via integrin signaling

We finally sought to obtain insight into the mechanism that underlies the PALMD-CaaX-promoted BP proliferation. BPs receive a variety of pro-proliferative signals from the extracellular environment via their processes, notably signals involving the extracellular matrix (ECM) (Fietz et al., 2012). ECM-promoted proliferation of both bRG (Fietz et al., 2010) and mBPs (Stenzel et al., 2014) has been shown to be mediated via integrin signaling.

We examined a potential role of integrin signaling in mediating PALMD-CaaX–promoted BP proliferation in mNcx, by focusing on integrin-β1 (Itgb1) (Loulier et al., 2009; Radakovits et al., 2009). We detected an increase in activated Itgb1 in the SVZ of mNcx upon IUE of PALMD-CaaX (Figure 7A, B).

Downstream pro-proliferative signaling upon integrin activation is known to involve PI3K-Akt and MEK-ERK pathways (Moreno-Layseca and Streuli, 2014). Analysis of IF for phospho-Akt and phospho-ERK (markers of active PI3K-Akt and MEK-ERK pathways, respectively) (Figures S7A, B, 7C) showed that IUE of PALMD-CaaX led to activation of both of these pathways in mouse BPs. These data demonstrate that activation of both integrins and the downstream signaling pathways in BPs is increased upon IUE of PALMD-CaaX in mNcx.

We performed an RNAi-mediated knock-down (KD) of Itgb1 in mNcx subjected to IUE of human PALMD-CaaX thereby reducing the level of activated Itgb1 in the SVZ to on average 37% of control (Figure S7C-E). IF analysis for PH3 and Ki67 revealed that this reduction resulted in a marked decrease in the abundance of basal mitoses and cycling BPs (Figure 7D-F). In fact, comparison with the effect of IUE of PALMD-CaaX on the levels of Ki67+ (Figure 4B) and PH3+ (Figure 4I) BPs revealed that the Itgb1 KD was sufficient to reduce the PALMD-CaaX–promoted

increase in BP proliferation back to the control levels. Hence, Itgb1 is required for the PALMD-CaaX–promoted increase in mouse BP proliferation.

To complement these data, we showed by EM that Itgb1 was actually localized to BP processes in both mNcx and hNcx (Figure 7H, I). We also demonstrated that ITGB1 in hNcx is required for progenitor proliferation (Figure S7F, G, see Methods for details).

Taken together, our data (Figures 3-6) suggested that the PALMD-CaaX-promoted increase in BP proliferation is the consequence of the PALMD-CaaX-induced increase in BP process growth. Accordingly, one would expect that the Itgb1 KD should not affect the PALMD-CaaX-induced increase in the number of BP processes. Indeed, tracking the morphology of the mBPs upon Itgb1 KD in mNcx revealed that this was the case (Figure 7G). This in turn is consistent with our concept that increasing BP process number underlies the observed increase in BP proliferative capacity.

DISCUSSION

Our study identifies a role of BP morphology that contributes in a major way to the differential proliferative capacity of BPs across mammals. Specifically, our data indicate that an increase in the number of BP processes leads to an increase in the proliferative capacity of BPs. In this regard, four aspects of our study deserve particular discussion: (i) the increase in the number of BP processes in the context of the evolutionary expansion of the Ncx; (ii) PALMD as an inducer of BP process growth, and its likely mechanism of action; (iii) the evidence that the BP morphology underlies BP proliferative capacity; and (iv) the requirement of Itgb1 for this increase in BP proliferative capacity.

BP process increase in the context of the evolutionary expansion of the Ncx

The evolutionary expansion of the Ncx is thought to be largely due to an increase in the proliferative capacity of BPs (Florio and Huttner, 2014; Lui et al., 2011). Here, we uncover that an increase in the number of BP processes constitutes a characteristic feature of this evolutionary expansion. First, we show that BPs contain more processes in hNcx than in fNcx and mNcx. Second, we show that both hNcx and fNcx exhibit a greater proportion of bRG morphotypes containing two or more processes compared to mNcx. Third, among these bRG morphotypes, the two morphotypes identified in the present study, bRG-(a)b_{bf}, appear to be especially increased in relative proportion in hNcx compared to fNcx. We therefore conclude that the greater the number of BP processes, the more expanded the Ncx. As an increase in UL neurons is a hallmark of Ncx expansion (Hutsler et al., 2005; Molnar et al., 2006), the increase in UL neurons observed upon IUE of PALMD-CaaX in mNcx is consistent with this conclusion. We are aware of the fact that in the phylogenetic tree, human is closer to mouse than ferret (Bininda-Emonds et al., 2007). Yet, we believe that the present comparison of BP morphology in these 3 species allows us to draw general conclusions about the role of increasing BP processes in Ncx evolution. In essence, we propose the concept, mechanistically discussed below, that increasing the number of BP processes can expose BPs to more pro-proliferative signals from their surrounding environment, ultimately leading to an increase in their proliferation.

PALMD as an inducer of BP process growth, and its likely mechanism of action

We identified the human morpho-regulatory protein PALMD, a member of the paralemmin family, as being necessary and sufficient to increase BP process number. In agreement with previous studies on other paralemmins (Arstikaitis et al., 2008; Kutzleb et al., 1998), several lines of evidence suggest that PALMD-CaaX induces BP process growth via modulation of the PM–actin cytoskeleton interaction.

First, IUE of only PALMD-CaaX isoform induced BP process growth *in vivo*, with the CaaX motif found to exert an essential role. This motif has previously been shown to mediate PM attachment via palmitoylation and prenylation (Gauthier-Campbell et al., 2004; Kutzleb et al., 1998), with the former modification shown to be involved in cell process formation, notably neurite outgrowth (Fukata and Fukata, 2010). In line with this, we show that upon specifically blocking palmitoylation, PALMD-CaaX loses the ability to induce new BP processes. Therefore, we propose a model in which the first step in the mechanism underlying the PALMD-induced BP process growth is the palmitoylation of PALMD-CaaX and its PM attachment (Figure 7J).

Second, a KO of PALMD in hNcx tissue reduced BP process number. Remarkably, this reduction was recapitulated upon KO of ADD3. Adducins are known to function in anchoring the actin cytoskeleton to the PM (Kiang and Leung, 2018). Hence, our findings strongly suggest that the observed increase in BP processes involves a PALMD-CaaX–modulated, adducin-mediated interaction of the actin cytoskeleton with the PM (Figure 7J).

Third, we note that the PALMD-CaaX–induced processes exhibited a high level of stability. This was evident when analyzing mBPs in mitosis. In contrast to normally rounded up mitotic mBPs, PALMD-CaaX–expressing mitotic mBPs maintained an increased number of processes. In light of previous findings with neurons (Gauthier-Campbell et al., 2004; Kutzleb et al., 1998), we therefore conclude that PALMD-CaaX expression not only results in an increase in mBP processes but also in their stabilization, the latter reflecting a robust interaction of the actin cytoskeleton with the PM (Figure 7J).

BP morphology underlies BP proliferative capacity

A key question regarding the interpretation of our data is whether the increase in BP proliferative capacity observed upon PALMD-CaaX expression is independent of the PALMD-

CaaX–induced increase in BP processes, or is the consequence of the latter. The following findings, when taken together, strongly suggest that the second scenario applies.

First, the PM attachment is required for both PALMD-mediated increase in BP process number and proliferation. This is evident from (i) our finding that only the PM-bound PALMD-CaaX, but not the cytosolic PALMD-KKVI can affect both BP features and (ii) that both phenotypes depend on PALMD palmitoylation. Furthermore, blocking palmitoylation in hNcx tissue reduced both the endogenous level of BP processes and that of cycling BPs, both of which reflected (at least in part) the presence of the endogenous human PALMD protein.

Second, the increase in BP process number preceded the increase in the level of cycling BPs upon IUE of PALMD-CaaX in mNcx.

Third, a KO of ADD3 in hNcx tissue reduced the level of cycling BPs, in a very similar manner as KO of PALMD. Adducins link the actin cytoskeleton to the PM and their involvement in cell proliferation is thought to occur indirectly via this cytoskeletal role (Kiang and Leung, 2018). Hence, the PALMD KO and the ADD3 KO phenotypes are most easily reconciled with one another by the concept that the reduction in BP process number constitute primary effects of both KOs, reflecting the lack of the normally occurring concerted action of PALMD and ADD3 at the PM (Figure 7J). The reductions in the level of cycling BPs upon PALMD KO and ADD3 KO would then reflect consequences of the reduction in BP process number.

How could the PALMD-CaaX–induced BP process growth lead to an increase in BP proliferative capacity? In addressing this question, it should be noted that increasing two distinct types of BP processes, the long basal processes of bRG and short processes of both bRG and mBPs, exert similar effects on promoting BP proliferation.

Long basal processes of bRG allows them to receive signals from the ECM components located at the basal lamina, which was shown to be important for proliferative capacity (Fietz et al., 2010). Hence, growing a second basal process, as is the case for the bRG-(a)b_{bf} morphotypes identified here, would allow each of the two daughters arising from the cell division of these

bRG to grow a basal process reaching the basal lamina, and is therefore likely to further promote the proliferative capacity of these BPs.

Short processes of mBPs and the apically directed process of bRG-ab and bRG-ab_{bf} enable these BPs to receive signals from the local environment. A previous study (Betizeau et al., 2013) has linked the presence of an apically directed process to the greater self-renewing potential of bRG-ab compared to bRG-b, in line with the notion that the local environment of BPs contains pro-proliferative signals. In agreement with this, our data demonstrate an increase in the number of short processes from mouse to human. The increase in the number of short processes of PALMD-CaaX–expressing mouse mBPs leads to an increase in the proliferative capacity of these cells, which provides further support for the notion that an increased ability to receive signals from the local SVZ environment can be conducive for BP proliferation. Of note, such local signals in the SVZ could, again, be provided by certain ECM components (Figure 7J), found to be enriched in hNcx BPs (Florio et al., 2015; Pollen et al., 2015).

Requirement of Itgb1 for the PALMD-CaaX-elicited increase in BP proliferative capacity

If the concept is true that increased BP process growth allows BPs to receive more pro-proliferative signals from their surrounding environment, notably involving ECM components, then one would expect that integrins, the major class of ECM receptors, are involved in the pro-proliferative signaling. Our data showing that Itgb1 is required for the BP proliferation increase observed upon PALMD-CaaX expression are in line with previous studies which found that integrin signaling promotes proliferation of cortical progenitors, notably of BPs (Fietz et al., 2010; Loulier et al., 2009; Stenzel et al., 2014). Importantly, reducing BP proliferative capacity by Itgb1 KD did not lead to a decrease in BP process number, which again is consistent with the notion that BP proliferation is downstream of BP morphology, and not *vice versa*.

There are several scenarios that can explain how the presence of actin in the proximity of the PM, may further Itgb1 activation (Figure 7J). First, integrins are known to be transported to cell protrusions such as filopodia by unconventional myosins, i.e. actin-based motors (Zhang et al., 2004). Consistent with this, we indeed detected Itgb1 on cell processes of SVZ cells. Second, recent models suggest that exertion of force by the actin cytoskeleton alone may

contribute to integrin activation (Li and Springer, 2017). Third, the major activators of integrins, talins, are also well-known actin-binding proteins (Klapholz and Brown, 2017). Thus, anchoring of the actin cytoskeleton to specific sites of the PM by the PALMD-CaaX–ADD3 interplay could facilitate the interaction of talin with Itgb1, which in turn would lead to its activation.

Activated integrins are in a high affinity state to bind their ECM ligands, which would trigger intracellular signaling downstream of integrins. The signaling upon PALMD-CaaX–promoted Itgb1 activation involved the PI3K-Akt and MEK-ERK pathways (Figure 7J), which are known to promote cell cycle progression (Moreno-Layseca and Streuli, 2014). In agreement with this, we show that human PALMD-CaaX is sufficient to promote cell cycle re-entry when expressed in mouse BPs. Interestingly, it has been shown that mutations of several molecules in the PI3K-Akt pathway are known to cause different neurodevelopmental disorders in human Ncx, including microcephaly (Hevner, 2015). It therefore appears worthwhile to explore whether genetic mutations of the components of the BP morpho-regulatory machinery studied here may underlie such disorders of so far unknown cause.

Acknowledgements:

We apologize to all researches whose work could not be cited due to space limitations. We are grateful to the Services and Facilities of the MPI-CBG for the outstanding support provided, notably J. Helppi and his team of the Biomedical Services, J. Peychl and his team of the Light Microscopy Facility, M. Sarov and his team of the Genome Editing Facility, I. Henry and his team of the Scientific Computing Facility (SCF), and the team of the Mass Spectrometry Facility. We thank H. Brandl from the SCF for help with statistics and gene expression analyses and M. Albert for critical reading of the manuscript. NK was supported by an EMBO long-term fellowship (ALTF 861-2013). WBH was supported by grants from the DFG (SFB 655, A2), the ERC (250197) and ERA-NET NEURON (MicroKin).

Author contributions:

Conceptualization, N.K.; Formal Analysis, N.K.; Investigation, N.K. in collaboration with C.G., B.S. (IP), M.W.B. (EM), A.S. (MS); Methodology, N.K., B.La. (help with ferret surgeries), H.K. (sharing technical knowledge on ferret IUE); M.F. (sharing technical knowledge on human *ex vivo* electroporation); Visualization, N.K.; Software, B.Lo.; Resources, K.R.L. (hNcx tissue), T.N. (plasmids), M.W.K. (Palm1 KO mice), P.W. (hNcx tissue); Writing - Original Draft, N.K., with input from C.G., B.S., K.R.L., T.N., B.La., B.Lo. and A.S.; Writing - Review & Editing, N.K. and W.B.H.; Supervision, W.B.H.; Project Administration and Funding Acquisition, W.B.H.

Declaration of interests:

The authors declare no competing interests.

References

Albrecht, I., Bieri, R., Leu, A., Granacher, P., Hagmann, J., Kilimann, M.W., and Christofori, G. (2013). Paralemmin-1 is expressed in lymphatic endothelial cells and modulates cell migration, cell maturation and tumor lymphangiogenesis. Angiogenesis *16*, 795-807.

Arstikaitis, P., Gauthier-Campbell, C., Carolina Gutierrez Herrera, R., Huang, K., Levinson, J.N., Murphy, T.H., Kilimann, M.W., Sala, C., Colicos, M.A., and El-Husseini, A. (2008). Paralemmin-1, a modulator of filopodia induction is required for spine maturation. Mol Biol Cell *19*, 2026-2038.

Betizeau, M., Cortay, V., Patti, D., Pfister, S., Gautier, E., Bellemin-Ménard, A., Afanassieff, M., Huissoud, C., Douglas, R.J., Kennedy, H.*, et al.* (2013). Precursor diversity and complexity of lineage relationships in the outer subventricular zone of the primate. Neuron *80*, 442-457.

Bininda-Emonds, O.R., Cardillo, M., Jones, K.E., MacPhee, R.D., Beck, R.M., Grenyer, R., Price, S.A., Vos, R.A., Gittleman, J.L., and Purvis, A. (2007). The delayed rise of present-day mammals. Nature *446*, 507-512.

Borrell, V., and Reillo, I. (2012). Emerging roles of neural stem cells in cerebral cortex development and evolution. Dev Neurobiol *72*, 955-971.

Britanova, O., de Juan Romero, C., Cheung, A., Kwan, K.Y., Schwark, M., Gyorgy, A., Vogel, T., Akopov, S., Mitkovski, M., Agoston, D.*, et al.* (2008). Satb2 is a postmitotic determinant for upper-layer neuron specification in the neocortex. Neuron *57*, 378-392.

Dehay, C., Kennedy, H., and Kosik, K.S. (2015). The outer subventricular zone and primate-specific cortical complexification. Neuron *85*, 683-694.

Fietz, S.A., Kelava, I., Vogt, J., Wilsch-Brauninger, M., Stenzel, D., Fish, J.L., Corbeil, D., Riehn, A., Distler, W., Nitsch, R.*, et al.* (2010). OSVZ progenitors of human and ferret neocortex are epithelial-like and expand by integrin signaling. Nat Neurosci *13*, 690-699.

Fietz, S.A., Lachmann, R., Brandl, H., Kircher, M., Samusik, N., Schroder, R., Lakshmanaperumal, N., Henry, I., Vogt, J., Riehn, A.*, et al.* (2012). Transcriptomes of germinal zones of human and mouse fetal neocortex suggest a role of extracellular matrix in progenitor self-renewal. Proc Natl Acad Sci U S A *109*, 11836-11841.

Florio, M., Albert, M., Taverna, E., Namba, T., Brandl, H., Lewitus, E., Haffner, C., Sykes, A., Wong, F.K., Peters, J.*, et al.* (2015). Human-specific gene ARHGAP11B promotes basal progenitor amplification and neocortex expansion. Science *347*, 1465-1470.

Florio, M., and Huttner, W.B. (2014). Neural progenitors, neurogenesis and the evolution of the neocortex. Development *141*, 2182-2194.

Fukata, Y., and Fukata, M. (2010). Protein palmitoylation in neuronal development and synaptic plasticity. Nat Rev Neurosci *11*, 161-175.

Gauthier-Campbell, C., Bredt, D.S., Murphy, T.H., and Ael-D., E.-H. (2004). Regulation of dendritic branching and filopodia formation in hippocampal neurons by specific acylated protein motifs. Mol Biol Cell *15*, 2205-2217.

Götz, M., and Huttner, W.B. (2005). The cell biology of neurogenesis. Nat Rev Mol Cell Biol *6*, 777-788.

Hansen, D.V., Lui, J.H., Parker, P.R., and Kriegstein, A.R. (2010). Neurogenic radial glia in the outer subventricular zone of human neocortex. Nature *464*, 554-561.

Haubensak, W., Attardo, A., Denk, W., and Huttner, W.B. (2004). Neurons arise in the basal neuroepithelium of the early mammalian telencephalon: a major site of neurogenesis. Proc Natl Acad Sci U S A *101*, 3196-3201.

Hevner, R.F. (2015). Brain overgrowth in disorders of RTK-PI3K-AKT signaling: a mosaic of malformations. Semin Perinatol *39*, 36-43.

Hu, B., Copeland, N.G., Gilbert, D.J., Jenkins, N.A., and Kilimann, M.W. (2001). The paralemmin protein family: identification of paralemmin-2, an isoform differentially spliced to AKAP2/AKAP-KL, and of palmdelphin, a more distant cytosolic relative. Biochem Biophys Res Commun *285*, 1369-1376.

Hutsler, J.J., Lee, D.G., and Porter, K.K. (2005). Comparative analysis of cortical layering and supragranular layer enlargement in rodent carnivore and primate species. Brain research *1052*, 71-81.

Jakovcevski, I., Filipovic, R., Mo, Z., Rakic, S., and Zecevic, N. (2009). Oligodendrocyte development and the onset of myelination in the human fetal brain. Front Neuroanat *3*, 5.

Kalebic, N., Taverna, E., Tavano, S., Wong, F.K., Suchold, D., Winkler, S., Huttner, W.B., and Sarov, M. (2016). CRISPR/Cas9-induced disruption of gene expression in mouse embryonic brain and single neural stem cells in vivo. EMBO reports *17*, 338-348.

Kawasaki, H., Iwai, L., and Tanno, K. (2012). Rapid and efficient genetic manipulation of gyrencephalic carnivores using in utero electroporation. Mol Brain *5*, 24.

Kiang, K.M., and Leung, G.K. (2018). A review on adducin from functional to pathological mechanisms: future direction in cancer. Biomed Res Int *2018*, 3465929.

Klapholz, B., and Brown, N.H. (2017). Talin - the master of integrin adhesions. J Cell Sci *130*, 2435-2446.

Kosodo, Y., Toida, K., Dubreuil, V., Alexandre, P., Schenk, J., Kiyokage, E., Attardo, A., Mora-Bermudez, F., Arii, T., Clarke, J.D.*, et al.* (2008). Cytokinesis of neuroepithelial cells can divide their basal process before anaphase. The EMBO journal *27*, 3151-3163.

Kutzleb, C., Sanders, G., Yamamoto, R., Wang, X., Lichte, B., Petrasch-Parwez, E., and Kilimann, M.W. (1998). Paralemmin, a prenyl-palmitoyl-anchored phosphoprotein abundant in neurons and implicated in plasma membrane dynamics and cell process formation. J Cell Biol *143*, 795-813.

Leone, D.P., Heavner, W.E., Ferenczi, E.A., Dobreva, G., Huguenard, J.R., Grosschedl, R., and McConnell, S.K. (2015). Satb2 Regulates the Differentiation of Both Callosal and Subcerebral Projection Neurons in the Developing Cerebral Cortex. Cereb Cortex *25*, 3406-3419.

Li, J., and Springer, T.A. (2017). Integrin extension enables ultrasensitive regulation by cytoskeletal force. Proc Natl Acad Sci U S A *114*, 4685-4690.

Loulier, K., Lathia, J.D., Marthiens, V., Relucio, J., Mughal, M.R., Tang, S.C., Coksaygan, T., Hall, P.E., Chigurupati, S., Patton, B.*, et al.* (2009). beta1 integrin maintains integrity of the embryonic neocortical stem cell niche. PLoS Biol *7*, e1000176.

Lui, J.H., Hansen, D.V., and Kriegstein, A.R. (2011). Development and evolution of the human neocortex. Cell *146*, 18-36.

Miyata, T., Kawaguchi, A., Saito, K., Kawano, M., Muto, T., and Ogawa, M. (2004). Asymmetric production of surface-dividing and non-surface-dividing cortical progenitor cells. Development *131*, 3133-3145.

Molnar, Z., Metin, C., Stoykova, A., Tarabykin, V., Price, D.J., Francis, F., Meyer, G., Dehay, C., and Kennedy, H. (2006). Comparative aspects of cerebral cortical development. Eur J Neurosci *23*, 921-934.

Moreno-Layseca, P., and Streuli, C.H. (2014). Signalling pathways linking integrins with cell cycle progression. Matrix Biol *34*, 144-153.

Namba, T., Kibe, Y., Funahashi, Y., Nakamuta, S., Takano, T., Ueno, T., Shimada, A., Kozawa, S., Okamoto, M., Shimoda, Y.*, et al.* (2014). Pioneering axons regulate neuronal polarization in the developing cerebral cortex. Neuron *81*, 814-829.

Noctor, S.C., Martinez-Cerdeno, V., Ivic, L., and Kriegstein, A.R. (2004). Cortical neurons arise in symmetric and asymmetric division zones and migrate through specific phases. Nature Neuroscience *7*, 136-144.

Pilz, G.A., Shitamukai, A., Reillo, I., Pacary, E., Schwausch, J., Stahl, R., Ninkovic, J., Snippert, H.J., Clevers, H., Godinho, L.*, et al.* (2013). Amplification of progenitors in the mammalian telencephalon includes a new radial glial cell type. Nat Commun *4*, 2125.

Pollen, A.A., Nowakowski, T.J., Chen, J., Retallack, H., Sandoval-Espinosa, C., Nicholas, C.R., Shuga, J., Liu, S.J., Oldham, M.C., Diaz, A.*, et al.* (2015). Molecular identity of human outer radial glia during cortical development. Cell *163*, 55-67.

Radakovits, R., Barros, C.S., Belvindrah, R., Patton, B., and Muller, U. (2009). Regulation of radial glial survival by signals from the meninges. J Neurosci *29*, 7694-7705.

Rakic, P. (1972). Mode of cell migration to the superficial layers of fetal monkey neocortex. J Comp Neurol *145*, 61-83.

Rakic, P. (2003). Developmental and evolutionary adaptations of cortical radial glia. Cereb Cortex *13*, 541-549.

Rakic, P. (2009). Evolution of the neocortex: a perspective from developmental biology. Nat Rev Neurosci *10*, 724-735.

Reillo, I., de Juan Romero, C., Cardenas, A., Clasca, F., Martinez-Martinez, M.A., and Borrell, V. (2017). A complex code of extrinsic influences on cortical progenitor cells of higher mammals. Cereb Cortex *27*, 4586-4606.

Reillo, I., de Juan Romero, C., Garcia-Cabezas, M.A., and Borrell, V. (2011). A role for intermediate radial glia in the tangential expansion of the mammalian cerebral cortex. Cereb Cortex *21*, 1674-1694.

Schenk, J., Wilsch-Brauninger, M., Calegari, F., and Huttner, W.B. (2009). Myosin II is required for interkinetic nuclear migration of neural progenitors. Proc Natl Acad Sci U S A *106*, 16487-16492.

Shitamukai, A., Konno, D., and Matsuzaki, F. (2011). Oblique radial glial divisions in the developing mouse neocortex induce self-renewing progenitors outside the germinal zone that resemble primate outer subventricular zone progenitors. The Journal of neuroscience : the official journal of the Society for Neuroscience *31*, 3683-3695.

Smart, I.H., Dehay, C., Giroud, P., Berland, M., and Kennedy, H. (2002). Unique morphological features of the proliferative zones and postmitotic compartments of the neural epithelium giving rise to striate and extrastriate cortex in the monkey. Cereb Cortex *12*, 37-53.

Sousa, A.M.M., Meyer, K.A., Santpere, G., Gulden, F.O., and Sestan, N. (2017). Evolution of the human nervous system function, structure, and development. Cell *170*, 226-247.

Stenzel, D., Wilsch-Brauninger, M., Wong, F.K., Heuer, H., and Huttner, W.B. (2014). Integrin alphavbeta3 and thyroid hormones promote expansion of progenitors in embryonic neocortex. Development *141*, 795-806.

Wang, X., Tsai, J.W., LaMonica, B., and Kriegstein, A.R. (2011). A new subtype of progenitor cell in the mouse embryonic neocortex. Nat Neurosci *14*, 555-561.

Wilsch-Bräuninger, M., Peters, J., Paridaen, J.T.M.L., and Huttner, W.B. (2012). Basolateral rather than apical primary cilia on neuroepithelial cells committed to delamination. Development *139*, 95-105.

Wong, F.K., Fei, J.F., Mora-Bermudez, F., Taverna, E., Haffner, C., Fu, J., Anastassiadis, K., Stewart, A.F., and Huttner, W.B. (2015). Sustained Pax6 expression generates primate-like basal radial glia in developing mouse neocortex. PLoS Biol *13*, e1002217.

Zhang, H., Berg, J.S., Li, Z., Wang, Y., Lang, P., Sousa, A.D., Bhaskar, A., Cheney, R.E., and Stromblad, S. (2004). Myosin-X provides a motor-based link between integrins and the cytoskeleton. Nat Cell Biol *6*, 523-531.

MAIN FIGURE TITLES AND LEGENDS

Figure 1. **Morphotypes of human proliferative BPs.**

(A) DAPI staining and IF for SOX2 and HOPX showing 6 morphotypes of human proliferative BPs (see schemes) in the OSVZ of 15-wpc hNcx (maximum intensity projection (MIP)). All images are oriented with the apical side facing down. Dashed lines, cell contours; arrows, basal processes; solid arrowheads, apical processes; open arrowheads, short processes of mBPs.

(B) Sparse DiI labeling of 12-wpc hNcx (MIP, stitched image (StI)). Box, bRG-ab$_{bf}$ shown at higher magnification in (B') at 3 different orientations as indicated.

(A, B) Scale bars, 10 µm (A, B'), 50 µm (B).

Seen also Figure S1 and Movies S1-S3.

Figure 2. **Quantitative analysis of BP morphotypes in mNcx, fNcx and hNcx.**

(A, B) DAPI staining and IF for GFP and PCNA of mNcx and fNcx upon IUE with mGFP as indicated. Arrowheads, examples of mGFP+ PCNA+ BPs.

(C) DAPI staining and IF for GFP and PCNA of hNcx tissue electroporated *ex vivo* with mGFP and soluble GFP as indicated. Box, bRG-b$_{bf}$ shown at higher magnification in (C') and (C''). (C'') MIP of 8 optical sections (left) and lower magnification MIPs of the same bRG-b$_{bf}$ along with the respective cell mask at 3 different orientations as indicated (right). Solid arrowheads, bRG-b$_{bf}$; arrows, basal processes, note that the shorter basal process terminates with a growth cone-like structure (double arrow); open arrowheads, short processes leaving the cell body.

(D-G) Quantitative analyses of BP morphotypes in E15.5 mNcx, E35 fNcx and 10-13–wpc hNcx, tracked by mGFP IF as described in (A-C).

(D) Distribution of bRG vs. mBP.

(E) Quantification of processes per single mBP.

(F) Distribution of the 5 bRG morphotypes, as shown schematically on the right.

(G) Quantification of radial processes per single bRG.

(A-C) Single optical sections (SOpS) (except for (C'')), StIs. Scale bars, 50 µm (A-C), 10 µm (C', C'' left), 30 µm (C'' three right panels).

(D-G) Mean of 8 (mouse D, E), 13 (mouse F, G), 4 (ferret) and 7 (human) experiments. Total number of cells scored: mouse 88 (D), 80 (E), 14 (F, G); ferret 88 (D), 43 (E), 45 (F, G); human 90 (D), 48 (E), 42 (F, G). Error bars, confidence interval (CI); ****, P <0.0001; ***, P <0.001; **,

P <0.01; *, P <0.05; n.s., not statistically significant; two-way ANOVA with Bonferroni post-hoc tests (D, F), Student's *t*-test (E, G).

See also Figure S2 and Movies S4,5.

Figure 3. PALMD-CaaX induces BP process growth in mNcx and fNcx.

(A) Sequential steps in the analysis of the transcriptome dataset of hNcx (Fietz et al., 2012), leading to the identification of *PALMD*.

(B) Human PALMD isoforms used for expression. Green and orange boxes, last protein-coding exons of *PALMD-CaaX* and of *PALMD*-KKVI, respectively. *PALMD-Δ,* truncated version lacking the last protein-coding exon.

(C) DAPI staining and IF for GFP and PALMD of EpH4 cells 2 days after transfection with GFP and control or different PALMD isoforms as indicated.

(D) Quantification of EpH4 cells that exhibit PM localization of PALMD, upon transfections as indicated.

(E) EM showing localization of Palmd in the cytoplasm of an SVZ cell body (upper left) and of a radial process in the VZ (lower left) of E14.5 mNcx, and on the PM of a process (upper right) and in the cytoplasm (lower right) of SVZ cells of 11-wpc hNcx. Arrows, Palmd in cytoplasm; arrowheads PALMD on PM.

(F-S) Analyses of mNcx (F-H, M-O) and fNcx (I-L, P-S) upon IUE with mGFP and control or PALMD isoforms as indicated. (G, H, J-M, O, R, S) Quantification of processes of BPs as tracked by mGFP IF.

(F) DAPI staining and IF for GFP and Ki67. Open arrowheads, cell processes.

(G, H) Quantification of processes per single mouse mBP (G) and of radial processes per single mouse bRG (H).

(I) IF for GFP and Pax6 of a ferret bRG-b_{bf} upon PALMD-CaaX IUE as indicated. Arrows, basal processes.

(J) Distribution of the 5 ferret bRG morphotypes, as shown schematically on the right.

(K, L) Quantification of processes per single ferret mBP (K) and of radial processes per single ferret bRG (L).

(M) Quantification of primary and all processes per single mouse mBP upon IUE with mGFP and control or different PALMD isoforms as indicated.

(N) DAPI staining and IF for GFP, Ki67 and PhVim. Arrowheads, cell processes.

(O) Quantification of primary and all processes per single mouse mitotic mBP.

(P, Q) Ferret mitotic mBP (P) and bRG (Q). DAPI staining and IF for GFP and PH3. Dashed lines, cell body. In (Q): Arrow, basal process; arrowhead, apical process.

(R, S) Quantification of primary and all processes per single ferret mitotic mBP (R) and of radial processes per single ferret mitotic bRG (S).

(C, E, F, I, N, P, Q) SOpS. Images are oriented with the apical side facing down (except C). Scale bars, 50 μm (C), 20 μm (F), 10 μm (I, N, P, Q), 100 nm (E). Cell shapes as tracked by mGFP IF are depicted along the IF images in (F, I, N, P, Q; note that cell shapes in (I, Q) are reduced in size relative to the IF images).

(D, G, H, J-M, O, R, S) Mean of 3 (M), 4 (D, J-L), 5 (R, S), 8 (G, H, O) experiments. Total number of cells scored: control 80 (G), 8 (H), 35 (J, L), 31 (K), 30 (M), 9 (O), 10 (R), 11 (S); PALMD-CaaX 89 (D), 79 (G), 8 (H), 41 (J, L), 34 (K), 35 (M), 17 (O), 8 (R), 13 (S); PALMD-KKVI 85 (D), 30 (M); PALMD-Δ 84 (D), 30 (M). Error bars, SD (D, R, S) or CI (G, H, J-M, O); ****, P <0.0001; ***, P <0.001; **, P <0.01; *, P <0.05; n.s., not statistically significant; one-way ANOVA with Bonferroni post-hoc test (D), two-way ANOVA with Bonferroni post-hoc test (J), Student's *t*-test (G, H, K-M, O, R, S).

See also Figure S3 and Table S1.

Figure 4. **PALMD-CaaX promotes BP proliferation in mNcx and fNcx.**

Analyses of mNcx (A-D, H, I) and fNcx (E-G) upon IUE with mGFP and control or PALMD isoforms as indicated.

(A) Quantification of mGFP+ PhVim+ mitoses.

(B) Percentage of mGFP+ cells in SVZ+IZ that are Ki67+.

(C, D) Following IUE, embryos were subjected to a single EdU pulse at E14.5, followed by DAPI staining and IF for GFP, Ki67 and EdU at E15.5. (C) Overviews of electroporated area.

(D) Percentage of EdU+ GFP+ cells in SVZ+IZ that are Ki67+.

(E) DAPI staining and IF for GFP and PhVim. Vertical arrows, apical mitoses; horizontal arrows, basal mitoses; arrowheads, bRG-ab.

(F) Quantification of mGFP+ PhVim+ mitoses.

(G) Percentage of mitotic BPs that are bRG.

(H) DAPI staining and IF for GFP and PH3.

(I) Quantification of basal mGFP+ PH3+ mitoses.

(C, E, H) SOpS, StIs. Scale bars, 50 µm (C), 20 µm (E, H).

(A, B, D, F, G, I) Mean of 5 (A, D, F, G), 3 (B), 8 (I, control and PALMD-CaaX), 4 (I, PALMD-KKVI and PALMD-Δ) experiments. Error bars, SD; **, P <0.01; *, P <0.05; n.s., not statistically significant; Mann-Whitney *U*-test.

See also Figure S4.

Figure 5. **PALMD and its palmitoylation are required for the BP process growth and proliferation.**

(A-D) Analyses of mNcx hemispheres 16 h after IUE with mGFP and control or PALMD-CaaX as indicated, either directly (A, C left, D left) or after incubation *ex vivo* for 24 h in the absence (DMSO; B left, C middle, D middle) or presence (2BrPal; B right, C right, D right) of 2BrPal.

(A, B) DAPI staining and IF for GFP and Ki67. Arrows, cell processes; dashed lines, cell body. (A) boxes, area shown at higher magnification on the right.

(C) Quantification of processes per single mBP.

(D) Percentage of mGFP+ cells in SVZ+IZ that are Ki67+.

(E-G) hNcx tissue was electroporated *ex vivo* with mGFP and soluble GFP, kept in culture and incubated in the absence (DMSO) or presence of 2BrPal as indicated in (E).

(E) DAPI staining and IF for GFP and PCNA of a bRG (top) and mBP (bottom). Arrowheads, cell bodies; arrows, cell processes.

(F) Quantification of processes per single mBP.

(G) Abventricular GFP+ cells that are PCNA+, expressed as percentage of control.

(H-L) hNcx tissue was electroporated *ex vivo* with mGFP and soluble GFP together with plasmids encoding *Cas9_T2A_RFP* and gRNA targeting either *LacZ* (Control) or *PALMD* (PALMD KO), as indicated.

(H) DAPI staining and IF for GFP, RFP (reflecting Cas9) and PCNA. Boxes (30 x 30 µm), areas shown at higher magnification on the right.

(I) Distribution of the 5 bRG morphotypes, as shown schematically on the right.

(J, K) Quantification of processes per single mBP (J) and of radial processes per single bRG (K).

(L) Abventricular Cas9+ cells that are PCNA+, expressed as percentage of Control.

(A, B, E, H) SOpS (A, B), MIPs (E, H), StIs (A, B, H). Scale bars, 50 µm (H), 30 µm (A), 20 µm (B), 10 µm (E).

(C, D, F, G, I-L) Mean of 6 (I-K), 4 (L) or 3 (C, D, F, G) experiments. Total number of cells scored: control 15 (C-16h, C-DMSO), 19 (C-2BrPal), 31 (I), 35 (J), 31 (K); PALMD-CaaX 15 (C-16h), 16 (C-2-BrPal), 26 (C-DMSO); PALMD KO 28 (I), 31 (J), 28 (K); DMSO in (F) 25; 2BrPal in (F) 18. Error bars, CI (C, F, I-K) or SD (D, G, L); ***, P <0.001; **, P <0.01; *, P <0.05; n.s., not statistically significant; Student's *t*-test (C, F, G, J, K), Mann-Whitney *U*-test (D, L), two-way ANOVA with Bonferroni post-hoc tests (I).

See also Figure S5.

Figure 6. **ADD3 is required for BP process growth and proliferation, and effects of PALMD-CaaX IUE on UL neurons.**

(A) List of top 10 PALMD interactors in IP from 12-13–wpc hNcx (triplicate analyses). Proteins are listed in descending order by their average number of unique peptides recovered. Green, adducins; blue, PALMD.

(B) Immunoblots, using anti-PALMD (left) and anti-ADD3 (right) antibodies, of IPs from hNcx using control, anti-PALMD or anti-ADD3 antibodies. Arrowheads, PALMD (left), ADD3 (right).

(C-F) hNcx tissue was electroporated *ex vivo* with mGFP together with plasmids encoding *Cas9_T2A_GFP* and gRNA targeting either *LacZ* (Control) or *ADD3* (ADD3 KO), as indicated.

(C) DAPI staining and IF for GFP, Ki67 and ADD3. Dashed lines, cell outline; arrowheads, presence of ADD3 along the PM of two non-electroporated progenitors in the ADD3 KO (right).

(D) Distribution of the 5 bRG morphotypes, as shown schematically on the right.

(E) Quantification of processes per single mBP.

(F) Abventricular GFP+ (reflecting Cas9+) cells that are Ki67+, expressed as percentage of control.

(G-K) Analyses of mNcx upon IUE with GFP and control or PALMD-CaaX as indicated.

(G) DAPI staining and IF for GFP and Satb2.

(H, I) Distribution of GFP+ cells (H) and Satb2+ GFP+ cells (I) across the CP layers.

(J) Percentage of GFP+ cells in the CP that are Satb2+.

(K) Thickness of CP layers V+VI and II+III+IV.

(C, G) SOpS, StIs. Scale bars, 30 μm (G), 20 μm (C).

(D-F, H-K) Mean of 5 (H-K) or 3 (D-F) experiments. Total number of cells scored: control 51 (D), 39 (E); ADD3 KO 55 (D), 35 (E). Error bars, CI (D, E) or SD (F, H-K); **, P <0.01; *, P <0.05; n.s.,

not statistically significant; two-way ANOVA with Bonferroni post-hoc tests (D, H, I), Student's *t*-test (E, F, J, K).

See also Figure S6 and Table S2.

Figure 7. The PALMD-CaaX–promoted increase in BP proliferation requires Itgb1.

(A-C) Analyses of mNcx upon IUE with mGFP and control or PALMD-CaaX as indicated.

(A) DAPI staining and IF for GFP and activated (act) Itb1. Boxes (30 x 30 µm), area shown at higher magnification in (A').

(B, C) Quantification of act Itgb1 (B), phospho-ERK (pERK, C) and phospho-Akt (pAk, C) immunoreactivity, determined as described in Methods.

(D-G) Analyses of mNcx upon IUE with mGFP and PALMD-CaaX together with a plasmid encoding either scrambled shRNA (Control) or shRNA targeting *Itgb1* as indicated.

(D) DAPI staining and IF for GFP, Ki67 and PH3. Arrowheads, GFP+ basal mitoses.

(E) Quantification of basal mGFP+ PH3+ mitoses.

(F) Percentage of mGFP+ cells in SVZ+IZ that are Ki67+.

(G) Quantification of processes per single mBP.

(H, I) EM showing localization of Itgb1 (arrowheads) on the PM of processes of SVZ cells in mNcx (H) and hNcx (I). All images are oriented with the apical side facing left.

(J) Model of PALMD-CaaX–mediated BP process growth and BP proliferation.

(A, D, H, I) SOpS. StIs (A, D). Scale bars, 50 µm (A, D), 100 nm (H, I).

(B, C, E-G) Mean of 3 (G), 4 (C, E, F), 7 (B) experiments. Total number of mBPs scored in (G): 30 per condition. Error bars, SD (B, C, E, F) or CI (G); *, P <0.05; n.s., not statistically significant; Mann-Whitney *U*-test (B, C, E, F), Student's *t*-test (G).

See also Figure S7.

STAR METHODS

CONTACT FOR REAGENT AND RESOURCE SHARING

Further information and requests for resources and reagents should be directed to and will be fulfilled by the Lead Contact, Wieland B. Huttner (huttner@mpi-cbg.de).

EXPERIMENTAL MODEL AND SUBJECT DETAILS

Experimental animals

All experimental procedures were conducted in agreement with the German Animal Welfare Legislation after approval by the Landesdirektion Sachsen (licences: mouse TVV 5/2015, ferret TVV2/2015). Animals used for this study were kept in standardized hygienic conditions at the Biomedical Services Facility (BMS) of the MPI-CBG with free access to food and water. Animals were kept with the following light cycle (light/dark): 12 h / 12 h (mice) and 16 h / 8 h (ferrets). All experiments were performed in the dorsolateral telencephalon of mouse and ferret embryos, at a medial position along the rostro-caudal axis. The developmental time points of experimental procedures (E13.5 for mouse and E33 for ferret) correspond to a mid-neurogenesis stage, when the production of UL neurons starts. The sex of embryos was not determined, as this is not likely to be of relevance for the results obtained in the present study.

Mice

Embryonic day E0.5 was set at noon of the day of vaginal plug identification. Mouse lines used were C57BL/6JOlaHsd and Palm1 KO line (Albrecht et al., 2013). C57BL/6JOlaHsd line was bred at the BMS of the MPI-CBG and the Palm1 KO line was bred at Max Planck Institute for Experimental Medicine and transported to MPI-CBG during the first week of pregnancy.

Ferrets

Timed-pregnant ferrets (*Mustela putorius furo*) were obtained from Marshall BioResources (NY, USA) or Euroferret (Copenhagen, Denmark) and housed at the BMS of MPI-CBG. Observed mating date was set to E0.

Human tissue

Fetal human brain tissue was obtained from two sources. First, from the Klinik und Poliklinik für Frauenheilkunde und Geburtshilfe, Universitätsklinikum Carl Gustav Carus of the Technische Universität Dresden, following elective pregnancy termination and informed written maternal consents, and with approval of the local University Hospital Ethical Review Committees. The age of fetuses ranged from 10-wpc to 12-wpc as assessed by ultrasound measurements of crown-rump length and other standard criteria of developmental stage determination. The second source was the Human Development Biology Resource (HDBR), with the fetal human material being provided by the Joint MRC/Wellcome Trust (MR/R006237/1) Human Developmental Biology Resource (www.hdbr.org). The HDBR provided tissue from fetuses aged 11-13–wpc. These developmental time points correspond to a mid-neurogenesis stage, when the production of UL neurons starts. Due to protection of data privacy, neither gender identity nor sex of the human fetuses from which Ncx tissue was obtained can be reported. Neither gender identity nor sex of the human fetuses is likely to be of relevance for the results obtained in the present study. The fetal hNcx tissue used in this study had not been subjected to any additional procedures. No health disorders were reported for any of the fetal hNcx tissue samples used in this study.

Fetal human brain tissue was dissected in PBS and used immediately for further manipulation or fixation when obtained from Dresden. When obtained from HDBR, tissue was dissected and shipped in Hibernate E media (Gibco A1247601). Upon arrival, the tissue was cultured in slice culture medium (SCM, see the following section) for 24 h prior to any further manipulation.

METHOD DETAILS

Plasmids

Human PALMD-CaaX– and PALMD-KKVI–encoding DNAs were amplified by PCR from a 12-wpc human brain cDNA library. The common forward primer, Palmd_SpHI_Fw, had an SpHI restriction site included upstream of the Kozak sequence. Both reverse primers (CAAX_BsrGI_Rev and KKVI_BsrGI_Rev) had a BsrGI restriction site included downstream of the stop codon. Subsequently, both PALMD isoforms were cloned into the pCAG vector using SpHI and BsrGI restriction enzymes. pCAG itself was generated from pCAG-GFP (a kind donation by Elly Tanaka and Stefania Tavano). PALMD-Δ was generated by site-directed

mutagenesis of the pCAG-PALMD-KKVI plasmid using the primers described in the Key Resources Table. The mutagenesis was performed using the QuikChange Lightning Site-Directed Mutagenesis kit following the manufacturer's instructions. The membrane GFP (mGFP) encoding plasmid used was pCAG-Lyn-GFP and was modified from the previously published pTα1-Lyn-GFP (Namba et al., 2014). Knock-down of Itgb1 in mNcx was performed using the pSuper RNAi system. The control vector, pSuper-Scrambled shRNA (kind gift by K. Kaibuchi), was modified to generate the pSuper-itgb1 shRNA vector with the AAGGGCCAACTTGTGAGACAT target sequence. Other commercial vectors used are listed in the Key Resources Table.

All DNA was purified using the QIAquick PCR Purification Kit (QIAGEN), eluted in 5 µl of distilled water and used to transform competent bacteria. All DNA plasmids were extracted and purified using the EndoFree Plasmid Maxi kit (QIAGEN) following the manufacturer's instructions.

CRISPR/Cas9 strategy and *in vitro* testing

CRISPR/Cas9 approach used for obtaining PALMD and ADD3 KOs *ex vivo* in hNcx was similar to the approach established previously in the mNcx in vivo (Kalebic et al., 2016). For controls, a previously published gRNA targeting LacZ was used (Kalebic et al., 2016). For disruption of *PALMD*, the genomic sequence of human *PALMD* was analyzed for CRISPR/Cas9 target sites by Geneious 11 software (Biomatters), and 7 gRNAs (cr1–cr7, Figure S5B, C) were selected. Cr1–cr4 had a forward orientation (identical in sequence to the DNA sense strand and not complementary to the mRNA sequence), and cr5–cr7 had a reverse orientation. gRNAs were produced by *in vitro* transcription from a PCR product as previously described (Kalebic et al., 2016). Recombinant Cas9 protein (ToolGen) from *Streptococcus pyogenes* was used.

Individual gRNAs were first tested *in vitro* using recombinant Cas9 protein and the PCR products of the *Palmd* locus. Three different PCR templates were made (Figure S5). PCR1 was used as the template for cr1, which guides cutting in intron 1, PCR2 was used for cr2 (cutting in exon 4) and PCR3 was used for the remaining gRNAs, all of which guide cutting in exon 7. Cutting by Cas9 of the target sequence *in vitro* was performed as previously described (Kalebic et al., 2016). Briefly, an *in vitro* reaction contained 12 ng/µl of the PCR product, 50 ng/µl of

recombinant Cas9 protein, and 35 ng/µl of the indicated *in vitro* transcribed gRNAs, in a total volume of 10 µl. Reactions were carried out at 37°C for 1 h. Samples were then treated with 4 µg of RNAse (Qiagen) for 15 min at 37°C, followed by addition of 2.5 µg of proteinase K (Merck) and further incubation for 10 min at 55°C. After 5 min at room temperature, samples received 1 µl of STOP solution (30% glycerol, 1.2% SDS, 250 mM EDTA pH 8.0; ToolGen) and were incubated for a further 15 min at 37°C, followed by analysis on a 1% agarose gel.

Based on the results of the *in vitro* testing, three gRNAs were selected for the *ex vivo* experiments. Cr1 was selected because it was able to guide Cas9-mediated cutting of the template and it was located most 5' within the *Palmd* gene; such a location has been shown to increase the probability of obtaining disruption of gene expression (Kalebic et al., 2016). Cr2 and cr3 were selected since they had the greatest efficiency of guiding the cutting of the PCR product, as revealed by the *in vitro* reaction (Figure S5C).

The three selected gRNAs were obtained from DNA 2.0, cloned into pD1321-AP plasmids under the control of the human U6 promoter. The same plasmid contained the *Cas9* gene under the CAG promoter, followed by sequences encoding the proteolytic self-cleaving 2A peptide from *Thosea asigna* virus (T2A) and Paprika RFP, which was used as an indicator of Cas9 expression. *Cas9* was flanked with two nuclear localization signals (5' and 3', (Kalebic et al., 2016)).

For the ADD3 KO, plasmids encoding three different gRNAs were obtained from Santa Cruz (adducin γ CRISPR/Cas9 KO plasmid (h); sc-417366). The plasmid design was similar to the one used for the PALMD KO. Briefly, gRNAs were under the control of the human U6 promoter and Cas9 under the CBh promoter. Cas9 was followed by T2A peptide and GFP.

***In vivo* experiments in mouse**

IUEs were performed as previously described (Kalebic et al., 2016). Briefly, pregnant mice with E13.5 embryos were anesthetized with isofluorane, first in a narcosis box (with 4% isoflurane) and then transferred to the operation platform, with their nose being connected to 2.5% isoflurane. Subsequently the animals were injected subcutaneously with the analgesic (0.1ml, Metamizol, 200mg/kg). The peritoneal cavity was then surgically opened and the uterus

exposed. Embryos were then injected intraventricularly with a solution containing 0.1% Fast Green (Sigma) in sterile PBS, 2 μg/μl of one of the CAG plasmids (empty vector, PALMD-CaaX, PALMD-KKVI, PALMD-Δ) and 1 μg/μl of the mGFP vector. All electroporations were performed with six 50-msec pulses of 28-33 V at 1 sec intervals. After surgery mice received Metamizol for two days via drinking water (1.33 mg/ml). Mice were sacrificed by cervical dislocation and embryos were harvested 16 h or 48 h post-electroporation, and the embryonic brains were dissected and PFA-fixed (see below) for the IF analyses or transferred into HERO culture (see below).

For the cell cycle re-entry experiments, a single pulse of EdU was injected at E14.5, i.e. 24 h after the IUE, and the animals were sacrificed 24 h later, as previously described (Wong et al., 2015). The cell cycle re-entry analysis was performed by quantifying the proportion of Ki67+ EdU+ GFP+ cells out of all EdU+ GFP+ cells. Considering that (i) EdU was likely incorporated only during the first 5 h after injection and (ii) the length of the S + G2 + M phase is less than 11 h at E14 (Wong et al., 2015), this type of analysis was suitable for determining whether the resulting daughter cells were still cycling or not.

***In vivo* experiments in ferret**

IUE of ferrets was performed as originally established by Hiroshi Kawasaki with the modifications described below (Kawasaki et al., 2012). Pregnant ferrets (with embryos at E33) were kept fasted for at least 3 h before the surgery and placed in the narcosis box with 4% isoflurane. Subsequently they were positioned on the operation table and attached to the narcosis mask with 3% isoflurane and injected subcutaneously with analgesic (0.1 ml Metamizol, 50 mg/kg), antibiotic (0.13 ml Synulox, 20 mg/kg or 0.1 ml amoxicillin, 10 mg/kg) and glucose (10 ml 5% glucose solution). The ferret bellies were then shaved, sterilized with iodide and surgically opened. The uterus was exposed and embryos were then injected intraventricularly with a solution containing 0.1% Fast Green (Sigma) in sterile PBS, 2.5 μg/μl of one of the CAG plasmids (empty vector, *PALMD-CaaX*) and 1.25 μg/μl of the mGFP vector. Electroporations were performed with six 50-msec pulses of 100 V at 1 sec intervals. Subsequently, the uterus was placed back in the peritoneal cavity, the muscle layer with the peritoneum was sutured using a 4-0 suture, after which the skin was sutured intracutaneously using 4-0 suture. Animals were carefully monitored until they woke up and then underwent

postoperative care for the following 3 days (2 x daily 10 mg/kg amoxicillin, 3 x daily 25 mg/kg Metamizol).

Two days after electroporation embryos were harvested. This occurred either after sacrificing the mother or by performing a second surgery. When the pregnant ferrets were sacrificed the protocol was as follows: 4 mg/kg Xylazin + 40 mg/kg Ketamin (0.2 ml Xylazin and 0.4 ml Ketamin) subcutaneously. After the embryos were removed, the ferrets were euthanized by an intracardial injection of 0.3 ml/animal T61.

When the pregnant ferrets were not sacrificed, they underwent another surgery that followed the same pre-operative care, anesthesia and analgesia as the first surgery. The sutures from the first operation were removed and the uterus exposed, after which the embryos were removed by a caesarian section. Subsequently a complete hysterectomy was performed, after which the muscle layer with peritoneum and skin were sutured and the animal underwent the same post-operative care as after the first surgery. Animals were kept at the BMS of the MPI-CBG for at least two weeks after the second surgery after which they were donated for adoption. Embryonic brains were dissected and PFA-fixed for the IF analyses.

***Ex vivo* experiments on hNcx**

Culture of hNcx tissue was done in slice culture medium (SCM): 84 ml of Neurobasal medium (Gibco, 21103049) supplemented with 10 ml of KnockOut Serum Replacement (Gibco, 10828028), 1 ml glutamine (2 mM), 1 ml Penstrep (100x), 1 ml N-2 (100x) (Gibco, 17502048), 2 ml B-27 (50x) (Gibco, 17504044) and 1 ml of 1 M HEPES-NaOH, pH 7.2, to yield a final volume of 100 ml.

For *ex vivo* electroporation, the hNcx tissue was placed in an electroporation chamber filled with sterile PBS. Tissue was positioned parallel to the electrodes so that the apical surface was facing the negative and the basal surface the positive electrode. The solution containing 0.1% Fast Green (Sigma) in sterile PBS along with the plasmids was administered adjacent to the apical surface of the tissue. Considering that the electroporated areas were difficult to identity when using only the plasmid encoding mGFP, we always administered a combination of plasmids encoding mGFP and soluble GFP to facilitate visualization. When only the two GFP

plasmids were used, 2 µg/µl of each plasmid was used. For the CRISPR/Cas9–mediated disruption of *PALMD*, 1 µg/µl of mGFP plasmid, 1 µg/µl of soluble GFP plasmid and 3 µg/µl of plasmids encoding Cas9 and gRNAs were used (control 3 µg/µl of gLacZ plasmid; PALMD KO 1 µg/µl of each of the three gPalmd plasmids). Electroporations were performed with ten 50-msec pulses of 36 V at 1 sec intervals. Subsequently, the tissue was washed in PBS, placed into a rotating flask with 1.5 ml SCM, and incubated at 37°C for 3-4 days in a humidified atmosphere of 40% O_2 / 5% CO_2 / 55% N_2, before being fixed.

For the 2-bromopalmitate (2BrPal) treatment, 2BrPal (Sigma, 238422) was dissolved in DMSO and a 100 mM stock solution was stored at –20°C. hNcx tissue was electroporated with (m)GFP-encoding plasmid(s) and kept in culture for one day, after which it was treated for 2 h at 37°C with 100 µM final concentration of 2BrPal in SCM or 0.1% DMSO as control. Subsequently, the tissue was transferred to a new flask with DMSO-free SCM and incubated for an additional 2 days at 37°C, before being fixed.

For ITGB1-blocking antibody treatment, P5D2 blocking antibody was used (Loulier et al., 2009). hNcx tissue was kept in culture for one day, after which it was incubated with the P5D2 antibody diluted 1:100 for 24 h in SCM at 37°C, before being fixed.

***Ex vivo* experiments on mouse hemispheres**

Mouse embryonic brains were electroporated at E13.5 and isolated 16 h later. Meninges were surgically removed and electroporated hemispheres were placed in the hemisphere rotation (HERO) culture. The HERO culture conditions were as previously described (Schenk et al., 2009). Upon dissection, hemispheres were placed in rotating flasks with 1.5 ml mouse SCM (mSCM), which had the identical composition as SCM described above except that 10 ml of the KnockOut Serum Replacement were replaced by the same amount of rat serum. Hemispheres were kept in mSCM for 2 h at 37°C to recover. Subsequently, the hemispheres were treated for 24 h at 37°C either with 20 µM final concentration of 2BrPal in SCM or with DMSO as control, before being fixed.

Transfection of cells in culture

To examine the subcellular localization of PALMD proteins we used EpH4-Ev, a mouse epithelial cell line that does not express detectable levels of Palmd protein. EpH4-Ev cells were seeded into 12-well plates at a density of 200,000 cells / well and transfected using Lipofectamine 2000 following the manufacturer's instructions. Cells in each well were transfected with 1 µg mGFP plasmid along with 4 µg of one of the pCAG plasmids (PALMD-Caax, PALMD-KKVI, PALMD-Δ, or empty vector). One day after transfection, cells were re-plated on coverslips into 12-well plates (100,000 cells / well) and processed for analysis 1 day later.

DiI labeling

DiI labeling of the hNcx tissue (12-wpc) was performed as previously described (Florio et al., 2015). Brielfy, a DiI working solution was prepared as previously described (Florio et al., 2015) and applied on the basal surface of the hNcx tissue by means of mouth-controlled pipette-tip. The dye was applied sparsely to facilitate the visualization of individual cells. After a single passage of DiI application, the tissue was washed 3 times with PBS and incubated in SCM (see above) for 4 h at 37°C. Subsequently, the tissue was PFA-fixed for 24 h at 4°C. After fixation the tissue was sectioned on a vibratome and 100-µm thick sections were stained with DAPI and mounted on microscopy slides with Mowiol.

Sectioning

Briefly, the tissue was fixed in 4% paraformaldehyde in 120 mM phosphate buffer pH 7.4 (referred to as PFA fixative) for 24 h (mNcx and hNcx tissue) or 48 h (fNcx) at 4°C. Subsequently, fixed tissue was sectioned on either a cryostat or vibratome. Cryosections were 20-50 µm thick and were mainly used for quantifications of nuclear markers. For cell tracking experiments, thick vibratome sections were used. Thickness of sections was as follows: 100-µm thick sections, all DiI experiments (Figure 1B, S1D-G), IF for Hopx/Sox2 in mNcx (Figure 2SH-J), all the experiments *ex vivo* with 2BrPal treatment (Figure 5A-G); 70-100–µm thick sections, all the mGFP tracking experiments in fNcx and hNcx and most of the experiments in E15.5 mNcx (Figure 2, S2A-F, O-P, Figure 5H-L, Figure 6C-E, Figure S6A-C, Figure S7D-G, most of experiments in Figure 3), all the HOPX/SOX2, IFs for HOPX/ANLN and BLBP/SOX2 in hNcx (Figure 1A, S1A-C, H-H", S2G), IF for PhVim in mNcx (Figure S2K-N); 50-µm thick sections, few mGFP tracking experiments in E15.5 mNcx (in Figure 3), IF for OLIG2 in hNcx (Figure 1I-N).

Immunofluorescence (IF)

IF was performed as previously described (Florio et al., 2015; Kalebic et al., 2016). When necessary, an antigen retrieval was performed (1 h incubation with 10 mM citrate buffer pH 6.0 at 70°C in a water bath or oven for mouse and ferret; 30 min with the same buffer for human tissue), followed by 3 washings with PBS, permeabilization for 30 min in 0.3% Triton X-100 at room temperature, quenching for 30 min in 0.1 M glycine in PBS at room temperature and blocking for 30 min in blocking solution (0.2% gelatin, 300 mM NaCl, 0.3% Triton X-100 in PBS). Primary antibodies were incubated in blocking buffer for 12 h – 3 days, at 4°C, depending on the antibody used. Subsequently the sections were washed 3 times in blocking solution, incubated with secondary antibodies (1:500 to 1:1000) and DAPI (Sigma) in blocking solution for 1-2 h at room temperature, and washed again 3 times in blocking solution before being mounted on microscopy slides with Mowiol.

EpH4 cells in culture were washed twice with PBS and fixed in the same fixative as the tissue for 5 min at room temperature. Afterwards IF was performed as described above for tissue.

Primary antibodies used for IF were all diluted 1:200 except for the following antibodies: anti-GFP and rabbit anti-RFP (1:1000), anti-pan-cadherin and rat anti-RFP (1:500), anti-PH3 (1:300), anti-Palmd (1:50). The PALMD antibody used was raised against amino acids 40-69 of human PALMD. This sequence is identical for PALMD-CaaX and PALMD-KKVI and therefore this antibody cannot be used to distinguish the two isoforms. The ADD3 antibody used was raised against amino acids 571-630 of human ADD3. Of these 60 amino acids, 55 are conserved in ferret and 47 in mouse ADD3.

Image acquisition

Most of the fluorescent images were acquired using a Zeiss LSM 880 upright single photon point scanning confocal system, and only few images were acquired using a Zeiss LSM 510 Duoscan laser-scanning confocal microscope. Images were taken as either 1-µm optical sections with a 40x objective or 2-µm optical sections with a 20x objective. When the images were taken as tile scans, the stitching of the tiles was performed using the ZEN software and the images are referred to in the figure legends as "stitched images" (StIs). The images are

presented either as single optical sections (referred to in the figure legends as "SOpS") or as maximum intensity projections (referred to in the figure legends as "MIPs"). The images were analyzed with ImageJ and processed with either ImageJ or Imaris 8 (BitPlane). The orthogonal projections and movies with the 3D visualization of cells were made using Imaris 8.

Electron microscopy

Electron microscopy was performed as described previously (Wilsch-Bräuninger et al., 2012), with the addition of antigen retrieval (for Palmd EM only, 30-min incubation with 10 mM citrate buffer pH 6.0 at 95°C in an incubator) prior to blocking. The primary antibodies against Palmd and Itgb1 (P5D2) were used at a 1:5-1:10 dilution and the signal was detected either by Protein A conjugated to 10 nm gold particles at a 1:50 dilution (for Palmd), or by a secondary antibody against mouse IgG conjugated to 10 nm gold particles at a 1:30 dilution (for Itgb1).

Immunoprecipitation and immunoblotting

For co-immunoprecipitation, all steps were performed at 4°C unless indicated otherwise. Affi-Prep® Protein A Resin beads (Bio-Rad, 1560006) were washed 3 times with 1 ml PBST (PBS, 0.04% Triton X-100) and incubated in 1ml PBST with 50 µg per 50 µl settled beads of either α-PALMD antibody (Abcam, ab129388) or α-ADD3 antibody (Santa Cruz, sc-74474) for 1 h at room temperature. Antibody-bound beads were then washed 3 times with PBST and lysis buffer (50 mM Tris-HCl pH 8.0, 150 mM NaCl, 1 mM EDTA, 0.1% SDS, 1% NP-40, Merck cOmplete™ Protease Inhibitor Cocktail) and stored on ice until use. Control beads were prepared in the same way using rabbit serum IgG fraction (Sigma-Aldrich, I5006). Embryonic/fetal brain tissue (E15.5 mouse, E37 ferret, 12-13–wpc human) was homogenized in 5 ml of lysis buffer on ice using a glass homogenizer (final protein concentration in the lysates: mouse 5 mg/ml, ferret 4 mg/ml, human 1-5 mg/ml). The lysates were centrifuged for 40 min, 10,000 g at 4°C, and 2 ml of supernatant per 50 µl of settled beads was added to experimental (α-PALMD or α-ADD3 bound) and control beads. In any given experiment, the same amount of protein was added to the three types of beads. Supernatants were incubated with the beads for 2 h in a cold room under rotation, which were then washed 3 times with lysis buffer. Bound proteins were eluted with sample buffer (ThermoFisher Scientific NuPAGE™ LDS Sample buffer, NP0007; 50 mM DTT), and samples were run on SDS-PAGE (ThermoFisher Scientific NuPAGE™ 4-12% Bis-Tris Protein Gel 1.0 mm, 10-well NP0321;

NuPAGE™ MES SDS Running Buffer NP0002). Gels were then processed for immunoblotting or MS.

For immunoblot analysis, gels were transferred for 2 h at 30 V in 10% methanol NuPAGE™ Transfer Buffer (ThermoFisher Scientific, NP0006). Membranes (Merck Immobilon®-P PVDF Membrane, IPVH00010) were blocked with 5% skim milk in PBST and incubated overnight with primary antibody (α-PALMD 1:1000 or α-ADD3 1:1000). Membranes were washed three times with PBST, incubated with secondary antibody (Peroxidase IgG Fraction Monoclonal Mouse Anti-Rabbit IgG, Light Chain Specific or Peroxidase AffiniPure Donkey Anti-Mouse IgG (H+L) 1:10,000; Jackson ImmunoResearch) for 1 h at room temperature, washed three times with PBST and developed for 5 min with SuperSignal™ West Dura Extended Duration Substrate (ThermoFisher Scientific, 34075). Times of exposure to X-ray film were varied for best visibility. Images were acquired using transmitted light.

Mass spectrometry (MS)

For MS, gels were incubated in Coomassie staining solution (50% methanol, 10% acetic acid, 0.2% CBB R-250) for 30 min at room temperature followed by washing in de-staining solution (50% methanol, 2% acetic acid). Gels were then transferred to water and subjected to GeLC MSMS analysis.

Coomassie-stained gel lanes were cut into 10 pieces per lane, each of which was then processed individually. Each gel piece was cut into 1x1 mm cubes, incubated with 10 mM DTT and 55 mM iodacetamide in 10 mM ammonium bicarbonate, and dehydrated with acetonitrile. The gel pieces were then rehydrated in 10 mM ammonium bicarbonate containing 10% acetonitrile and 12 ng/µl trypsin (modified, sequencing grade, Promega, Mannheim) and subjected to overnight *in-gel* digestion at 37°C. The resulting peptide mixtures were extracted twice with exchange of 5% formic acid and 100% acetonitrile, the extracts pooled together and dried down. The dry residue containing the peptides was dissolved in 20 µl of 5% formic acid, and 5 µl were taken for LCMSMS analysis. This analysis was performed on a nano-UPLC Ultimate 3000 interfaced on-line to a Velos LTQ Orbitrap hybrid mass spectrometer (both Thermo Fischer Scientific, Bremen). The UPLC system was equipped with Acclam PepMap^{tm} 100 75 µm x 2 cm trapping column and 75 µm x 50 cm separating column

packed with 3 µm diameter C18 particles (Thermo Fischer Scientific, Bremen), which was heated to 50°C. Peptides recovered from each gel piece were separated using a 180 min linear gradient 0 to 35 % of solvent B (0.1% formic acid in acetonitrile) in solvent A (0.1% formic acid in water) followed by step increase to 100% solvent B for 15 minutes. Velos instrument was operating in CID mode where 1 MS scan (R=60000) was followed by MSMS acquired on top 20 most abundant ions. Normalized collision energy was set on 35 and dynamic exclusion time on 25 s. The lock-mass function was set to recalibrate MS1 scans using the background ion $(Si(CH_3)_2O)6$ at m/z 445.12. Spectra acquired for pieces from the same gel lane were converted into .mgf format, merged into a single file and searched against human, mouse or ferret sequences in the UniProt database (January 2018) using MASCOT software (version 2.2.04, Matrix Sciences Ltd, London, UK). Mass tolerance was set on 5 ppm and 0.5 Da for precursor and fragment ions respectively; enzyme specificity – trypsin; number of miscleavages was set on two; variable modification – cysteine carbamidomethyl and propionamide, methionine oxidation, protein N-terminal acetyl. The results of the database searches were evaluated by Scaffold software v.4.7.5 (Proteome Software, Portland). Protein hits were accepted if matched with one peptide under 90% and 95% probability thresholds for peptides and proteins, respectively. Proteins and spectra False Discovery Rates (FDR, function of the Scaffold software) were calculated below 1%.

Human PALMD immunoprecipitation and subsequent MS analysis were performed in triplicates. Of the 603 proteins identified in total by MS in the sum of the three PALMD and the three control immunoprecipitates, 21 were found exclusively in all three PALMD immunoprecipitates but not in any of the control immunoprecipitates. This list of 21 interactors also contained the bait, PALMD itself. Among the top five interactors on this list (Table S2), three belonged to the adducin family of proteins (ADD1, ADD2, ADD3). For this reason, we examined the mRNA expression levels of the three members of the adducin family in the previously published transcriptome datasets (Fietz et al., 2012; Florio et al., 2015) and, based on the similarity of the *ADD3* mRNA expression pattern (Figure S6D) with that of *PALMD* (Figure S3A), identified *ADD3* as the top candidate to be a PALMD interactor. Immunoprecipitation of ferret and mouse Palmd followed by MS analysis was performed in the same way, but only once each. ADD3 was found in the ferret, but not the mouse, Palmd immunoprecipitate (Table S2).

QUANTIFICATION AND STATISTICAL ANALYSIS

Tracking cell outlines

To analyze the morphology of BPs in a quantitative manner, we developed a semi-manual workflow named Progenitors Process Analysis (PPA) software. Images used for this workflow were acquired on a confocal microscope with a 40x objective as ≈50-100–µm thick stacks of 1-µm thick optical sections. Individual cells were first annotated manually with Fiji plugin trakEM2 and exported as 2D masks for further analysis. Each cell was processed to create a mask of the cell body and a skeleton of the processes. The cell body mask was then combined with the processes skeleton, constituting a simplified representation of the cell that could be used for the analysis of its morphology. If necessary the cell body mask could be corrected manually during the process. In this representation, each process is a branching tree. It is in contact with the cell body at a single position, may or may not divide into multiple branches defining one or more extremities. For each BP the number of processes, the total number of process extremities, the branching index (ratio of all process extremities to the primary processes count) and the cell body (soma) radius were measured. Additionally, a Sholl analysis was performed, which consisted of counting the number of branches intersecting circles of either 2r, 3r or 4r, with r being the radius of the cell body and the circle center being in the middle of the cell body. For each process, we also measured its length and tortuosity. Finally, for each analyzed cell, an image allowing the visual inspection of the cell body and the detected processes was generated. This entire workflow was implemented as a script for the freely available Fiji software. The script was tested with the Fiji version: (Fiji is just ImageJ) ImageJ 2.0.0-rc-61/1.51n. The source code of the script and its helper library are available on an online repository (git platform of MPI-CBG, https://git.mpi-cbg.de/bioimage-informatics/Progenitors_Processes_Analysis). Additional details on the installation, usage and implementation of the workflow can be found on that repository.

Tracking of DiI-labeled bRG basal processes (Figure S1F) was performed starting from the basal side and stopping at the cell body in the SVZ. The tracked processes were analyzed with respect to whether they contained a splitting site or not. Splitting sites in the basal-most 50 µm were excluded as those likely accounted for basal end-foot branching and not radial

process bifurcation. As DiI was applied on the basal surface, only bRG-b, bRG-ab and the morphotypes identified here (bRG-b_{bf} and bRG-ab_{bf}) could be traced.

Identification of *PALMD*

To identify genes that potentially regulate BP morphology in hNcx, we used a published transcriptome dataset of mouse and human Ncx zones (GSE38805) (Fietz et al., 2012). As summarized in Figure 3A, of the 13.719 genes that were found to be expressed in fetal human OSVZ and ISVZ (FPKM >1), we focused our analysis on those genes that exhibited an at least 2-fold higher level of expression in the OSVZ and ISVZ compared to the VZ and CP, which yielded 250 genes. Among these 250 genes, we focused our attention on those genes that exhibited and at least 10-fold increase in FPKM value from the VZ to the OSVZ and from the VZ to the ISVZ, which yielded 25 genes (Table S1). Of these 25 genes, 7 were potentially related to cell morphology by GO term analysis (Table S1). The top candidate among these 7 potential morpho-regulatory genes that exhibited the highest fold change between VZ and OSVZ/ISVZ (of all 25 genes) was *PALMD* (96-fold increase between VZ and OSVZ and 56-fold increase between VZ and ISVZ). In the transcriptome of mNcx (Fietz et al., 2012), *Palmd* was also found to be enriched in the SVZ compared to VZ and CP, but the fold increase between VZ and SVZ was only 2. This suggested that (i) *Palmd* could potentially be a general regulator of BP morphology across different mammalian species, and (ii) that *Palmd* exhibits evolutionary different expression levels, which was in line with our findings on the evolutionary increase in the number of BP processes and BP morphotypes. For the above-mentioned reasons, we selected *PALMD* as our candidate to manipulate BP morphology.

The data of gene expression in various neocortical cell types isolated from mNcx and hNcx are from the previously published datasets of mouse and human Ncx cells (GSE65000) (Florio et al., 2015). To determine the expression levels of individual *PALMD* isoforms, the Kallisto probabilistic algorithm was used. The age of the fetuses used for the transcriptome study of the hNcx ranged from 13-wpc to 16-wpc (Fietz et al., 2012) and from 12-wpc to 13-wpc (Florio et al., 2015). All these fetal stages are comparable to the stages we used for our various analyses in hNcx (11-wpc to 16-wpc).

Cell counting

All cell counts were performed in standardized microscopic fields using Fiji, processed using Excel (Microsoft), and results were plotted using Prism (GraphPad Software). For each condition, data (typically at least 3 microscopic fields) from one experiment (see definition below) were pooled, and the mean of the indicated number of experiments was calculated. Whenever possible the quantifications were done blindly. To identify BPs we uniformly used the marker shown in the panel(s) preceding the respective quantification of morphology, or markers indicated along with the quantification of morphology. For mGFP-electroporated BPs, PCNA (Figure 2D-G; Figure S2E; Figure 3K; Figure S3O, Figure 5F, I-K; Figure S5A; Figure S5I, J) or Ki67 (Figure 3G, H; Figure S3I-L; Figure 5C; Figure 6D, E; Figure S6B; Figure 7G) were used as markers. For non-electroporated BPs, Hopx+Sox2 were used as markers (Figure S1H, L, M; Figure S2G, J). For the mGFP-electroporated bRG analyzed in Figure 3L and Figure S3P, in addition to PCNA+ cells with radial morphology, Pax6 was used as marker. For mitotic BPs, PH3 (Figure 3R, S) and PhVim (Figure S2M, N, Figure 3O) were used as markers. DAPI staining was used to delineate the border between layer III and layer IV and the border between layer IV and layer V in the mouse E18.5 CP (Figure 6G-K).

Quantification of IF intensity

All quantifications of IF intensity were done blindly. The quantifications of the IF intensity upon PALMD and ADD3 KOs were done focusing only on those RFP+ (for PALMD KO) or GFP+ (for ADD3 KO) cells that were not in direct contact with other RFP+/GFP+ cells. The cell perimeter was outlined using the RFP/GFP channel, as this channel reflected the expression of a protein which contained no specific localization signal and which marked the entire cell body along with the clearly identifiable processes. Subsequently, by using the DAPI channel, a confirmation that the outlined area contained only a single nucleus was obtained. After switching to the PALMD/ADD3 channel, a measurement of the IF intensity within the outlined area was performed. Measuring of the PALMD/ADD3 IF intensity was performed only for those outlined areas that met the above-mentioned criteria (no overlap with other cells, presence of a single nucleus). Upon subtraction of the background signal, the average IF intensity level of the control conditions was set to 100%, and all the IF intensity levels of the KO conditions were expressed relative to this.

The quantifications of the Itgb1, active Itgb1, pERK and pAkt IF intensities upon PALMD-CaaX expression and the quantification of Itgb1 IF intensity upon combined PALMD-CaaX expression and Itgb1 KD were done as follows. Inspecting the GFP channel, which reflected the location of the electroporated area, a 50 µm x 50 µm region of interest (ROI) was selected in the SVZ. Subsequently, by using the DAPI channel, a confirmation that the selected ROI was located in the SVZ was obtained. Switching to the Itgb1/pERK/pAkt channel, the level of IF intensity was measured within the ROI. A total of 3-5 different ROIs in the electroporated area were selected for each section, and the mean was calculated. Subsequently, 1-2 ROIs of the same dimensions were selected in the SVZ outside the electroporated area of the same histological section. In case of small-area electroporations, this was done by selecting ROIs in the same hemisphere. In case of large electroporations that were spanning the majority of the hemisphere, an equivalent position was selected in the contralateral hemisphere. The level of IF intensity of the electroporated SVZ was expressed relative to the level of this intensity from the non-electroporated area of the same histological section.

Statistical analyses

Sample sizes are reported in each figure legend, where the term "one experiment" refers to one embryo coming from an independent litter for analysis of mNcx and fNcx and to one individual hNcx tissue sample for analysis of hNcx. All IUE experiments were performed in as many litters as indicated in each figure legend with the term "experiment". From each litter a single control and experimental (usually PALMD-CaaX expression) embryo were used for further analysis. No litters and hNcx tissue samples were excluded from the statistical analysis.

All statistics analyses were conducted using Prism (GraphPad Software). We used parametric statistics for normally distributed data (determined by Shapiro-Wilk or D'Agostino-Pearson omnibus normality tests with alpha level of 0.05) and non-parametric tests otherwise. Tests used were two-way ANOVA with Bonferroni post-hoc test, one-way ANOVA with Dunnett's multiple comparisons test, Student's *t*-test and Mann-Whitney *U*-test. For each quantification, the statistical test and P value are indicated in the figure legend. For the main figures, when the comparisons between different categories were made, P values of the post-hoc test are indicated as follows: Figure 2F, bRG-b (mouse vs. ferret, P =0.0009; mouse vs. human, P <0.0001; ferret vs. human, P =0.0281); Figure 2F, bRG morphotypes with two or more

processes (bRG-ab+bRG-(a)b_{bf}) vs. bRG with a single process (bRG-b+bRG-a) (human vs. mouse, P<0.0001; ferret vs. mouse, P=0.0078); Figure 3J, bRG-b (control vs. PALMD-CaaX P=0.039); Figure 5I, bRG-b (control vs. PALMD KO, P=0.0016); Figure 6D, bRG-b (control vs. ADD3 KO, P=0.0041); Figure 6H, layers II+III (control vs. PALMD-CaaX, P=0.0101); Figure 6H, layers V+VI (control vs. PALMD-CaaX, P=0.0017); Figure 6I, layers V+VI (control vs. PALMD-CaaX, P=0.0068). For the supplemental figures the P values of the post-hoc test are given in the respective figure legends.

Supplemental movie S1 Related to Figure 1. 3D representation of a bRG-ab$_{bf}$ in hNcx revealed by DiI.

Supplemental movie S2 Related to Figures 1 and S1. 3D representation of a bRG-ab and bRG-b in hNcx revealed by DiI.

Supplemental movie S3 Related to Figures 1 and S1. 3D representation of a bRG-b$_{bf}$ in hNcx revealed by DiI.

Supplemental movie S4 Related to Figure 2. 3D representation of a bRG-b$_{bf}$ in hNcx revealed by mGFP fluorescence, with its cell mask indicated subsequently.

KEY RESOURCES TABLE

REAGENT or RESOURCE	SOURCE	IDENTIFIER
Antibodies		
Goat anti-Sox2	R+D Systems	AF2018, RRID:AB_355110
Mouse anti-Hopx	Santa Cruz Biotech	Sc-398703, RRID:AB_2687966
Rabbit anti-Hopx (FL-73)	Santa Cruz Biotech	Sc-30216, RRID:AB_2120833
Rabbit anti-Blbp	LifeSpanBioScience	LS-C30565, RRID:AB_2100467
Chicken anti-GFP	Abcam	ab13970, RRID:AB_300798
Rat anti-RFP	ChromoTek	Cat#5F8
Rabbit anti-RFP	Rockland antibodies	600-401-379, RRID:AB_2209751
Goat anti-Anillin	Abcam	ab5910, RRID:AB_2058292
Rabbit anti-Olig2	Millipore	ab9610, RRID:AB_570666
Goat anti-GFP	MPI-CBG	N.A.
Rabbit anti-Ki67	Abcam	ab15580, RRID:AB_443209
Rabbit anti-Pax6	Covance	PRB-278P, RRID:AB_291612
Mouse anti-PCNA	Millipore	CBL407, RRID:AB_93501
Rabbit anti-Palmd	Abcam	ab129388, RRID:AB_11145499
Mouse anti-PanCDH, clone CH-19	Sigma	C 1821, RRID:AB_476826
Mouse anti-PhVim	Abcam	ab22651, RRID:AB_447222
Rat anti-PH3	Abcam	ab10543, RRID:AB_2295065
Mouse anti-ADD3	Santa Cruz	sc74474, RRID:AB_1118719
Mouse anti-Satb2	Abcam	ab51502, RRID:AB_882455
Rat anti-CD29 β1 integrin (active), clone 9EG7	BD Pharmigen	550531, RRID:AB_393729
Mouse anti-β1 integrin (blocking antibody), P5D2	Abcam	ab24693, RRID:AB_448230
Phospho-p44/42 MAPK (Erk1/2) (Tyr 202/Tyr204)	Cell Signaling	Cat# 9106, RRID:AB_331768
Mouse anti-AKT pS473	Rockland antibodies	200-301-268S, RRID:AB_2224884
Goat anti-Chicken Alexa Fluor 488	ThermoFisher Scientific	A11039, RRID:AB_142924
Donkey anti-Goat Alexa Fluor 488	ThermoFisher Scientific	A11055, RRID:AB_2534102
Donkey anti-Goat Alexa Fluor 555	ThermoFisher Scientific	A21432, RRID:AB_2535853
Donkey anti-Goat Alexa Fluor 647	ThermoFisher Scientific	A21447, RRID:AB_141844
Donkey anti-Rabbit Alexa Fluor 488	ThermoFisher Scientific	A21206, RRID:AB_141708
Donkey anti-Rabbit Alexa Fluor 555	ThermoFisher Scientific	A31572, RRID:AB_162543

Donkey anti-Mouse Alexa Fluor 555	ThermoFisher Scientific	A31570, RRID:AB_2536180
Donkey anti-Mouse Alexa Fluor 647	ThermoFisher Scientific	A31571, RRID:AB_162542
Goat anti-Rabbit Cy2	Jackson Immuno research	# 111-225-144, RRID:AB_2338021
Goat anti-Mouse Cy3	Jackson Immuno research	#115-165-166, RRID:AB_2338692
Goat anti-Mouse Cy5	Jackson Immuno research	#115-175-166, RRID:AB_2338714
Goat anti-Rat Alexa Fluor 647	ThermoFisher Scientific	A21247, RRID:AB_141778
Mouse anti-rabbit light chain specific IgG HRP	Jackson Immuno research	211-032-171, RRID:AB_2339149
Donkey anti-mouse IgG (H+L) HRP	Jackson Immuno research	715-035-151, RRID:AB_2340771
Rabbit serum IgG fraction	Sigma Aldrich	I5006, RRID:AB_1163659
Protein A-10 nm Gold	UMC Utrecht	N.A.
Goat anti-Mouse IgG 10 nm Gold	BBI solutions	Cat# EM.GMHL10
Bacterial and Virus Strains		
XL-10 Gold Ultracompetent cells E.Coli	Agilent Technologies	#200315
Biological Samples		
10-12–wpc human brain tissue	Uniklinikum Dresden	N.A.
10-13–wpc human brain tissue	HDBR	N.A.
15- and 16-wpc fixed human brain tissue	HDBR	N.A.
Chemicals, Peptides, and Recombinant Proteins		
Cas9 WT protein, injection ready, lyophilized	ToolGen	Cat# TGEN_CP1
Critical Commercial Assays		
Maxi prep kit	Qiagen	Cat#12362
QuikChange Lightning Site-Directed Mutagenesis kit	Agilent Technologies	Cat#210518
Lipofectamine 2000 Reagent	Invitrogen	Cat#11668-019
Adducin γ CRISPR/Cas9 KO plasmid (h)	Santa Cruz	sc-417366
Experimental Models: Cell Lines		
Mouse: Eph4-Ev cells	ATCC	Cat# ATCC® CRL-3063TM
Experimental Models: Organisms/Strains		
Mouse: C57BL/6JOlaHsd	MPI-CBG	N.A.
Mouse: Palm1 KO	(Albrecht et al., 2013)	N.A.
Ferret *Mustela putorius furo*	Marshall Bioresources	N.A.
Ferret *Mustela putorius furo*	Euroferret	N.A.
Oligonucleotides		
Palmd cloning primers, see Table S3	This paper	N.A.
Palmd mutagenesis primers, see Table S3	This paper	N.A.
LacZ gRNA: TGCGAATACGCCCACGCGAT	(Kalebic et al., 2016)	N.A.
Palmd gRNAs, see Table S3	This paper	N.A.
CRISPR test Primers, see Table S3	This paper	N.A.
Recombinant DNA		
pCAG	This paper	N.A.
pCAG-Palmd-Caax	This paper	N.A.
pCAG-Palmd-KKVI	This paper	N.A.
pCAG-Palmd-Delta	This paper	N.A.
pCAG-GFP	(Fei et al., 2014)	N.A.

pCAGGS-Lyn GFP (mGFP)	Mod.from (Namba et al., 2014)	N.A.
pCas9-LacZ	DNA2.0	pD1321-AP:211150
pCas9-gPalmd_cr1	DNA2.0	N.A.
pCas9-gPalmd_cr2	DNA2.0	N.A.
pCas9-gPalmd_cr3	DNA2.0	N.A.
pSuper-Scrambled shRNA	(Namba et al., 2014)	N.A.
pSuper-ITGB1 shRNA	This paper	N.A.
Software and Algorithms		
Fiji/ImageJ	Fiji/Imagej	https://imagej.nih.gov/ij/
Imaris 8	BitPlane	N.A.
Prism	GraphPad software	N.A.
ZEN	Carl Zeiss	N.A.
TrakEM2 0.9a	Imagej	N.A.
Geneious 11.0	Biomatters Ltd	N.A.
Process tracker	This paper	N.A.

Figure 1

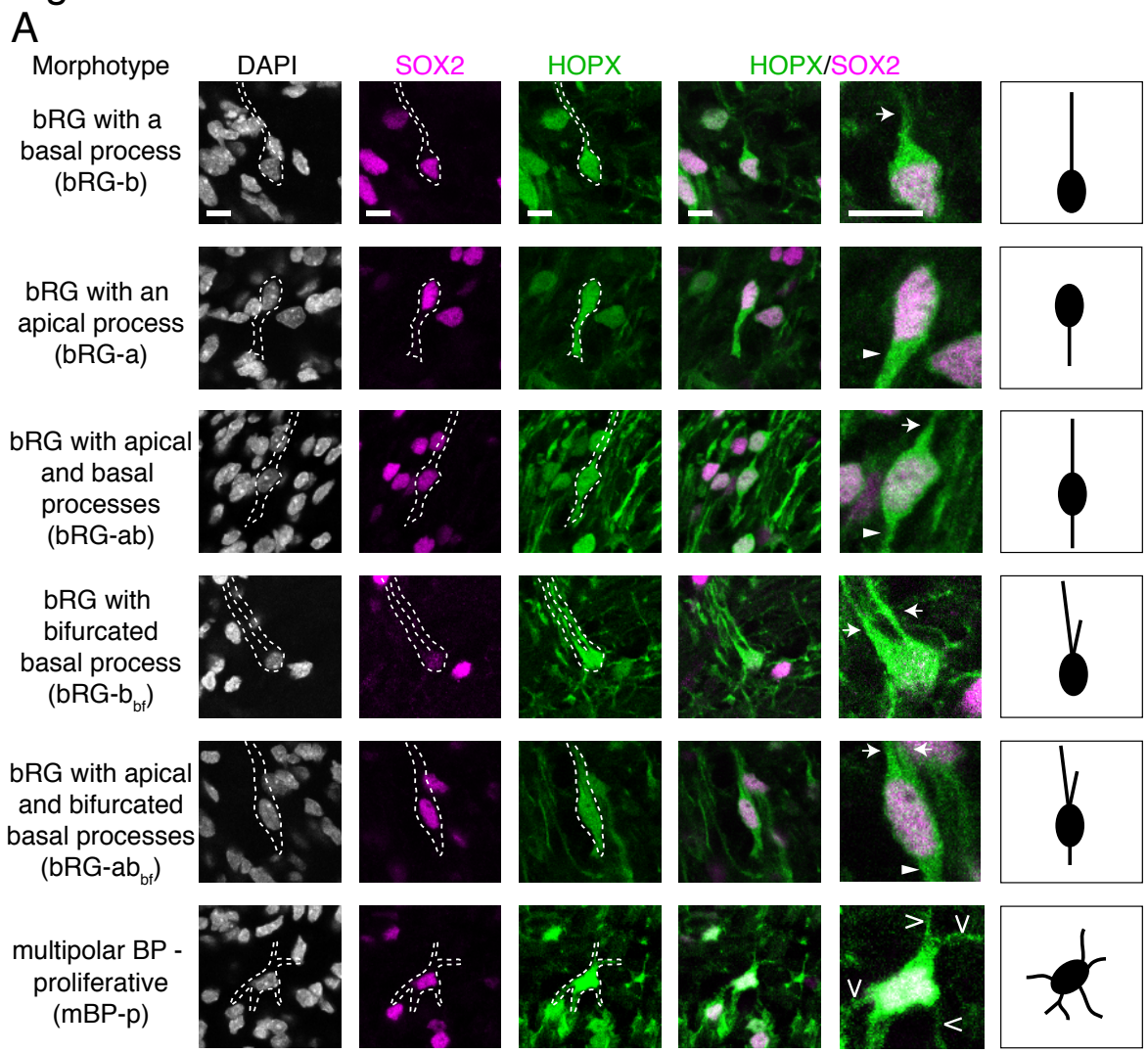
A
Morphotype
DAPI
SOX2
HOPX
HOPX/SOX2
bRG with a basal process (bRG-b)
bRG with an apical process (bRG-a)
bRG with apical and basal processes (bRG-ab)
bRG with bifurcated basal process (bRG-b$_{bf}$)
bRG with apical and bifurcated basal processes (bRG-ab$_{bf}$)
multipolar BP - proliferative (mBP-p)

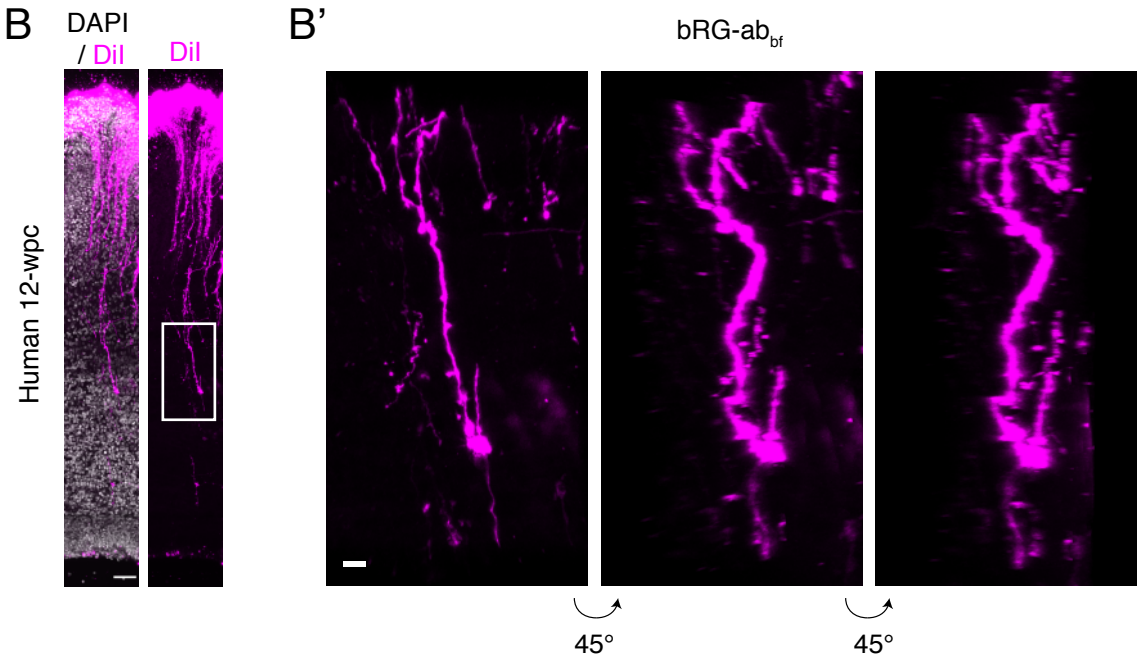
B
DAPI / DiI
DiI
Human 12-wpc
B'
bRG-ab$_{bf}$
45°
45°

Figure 2

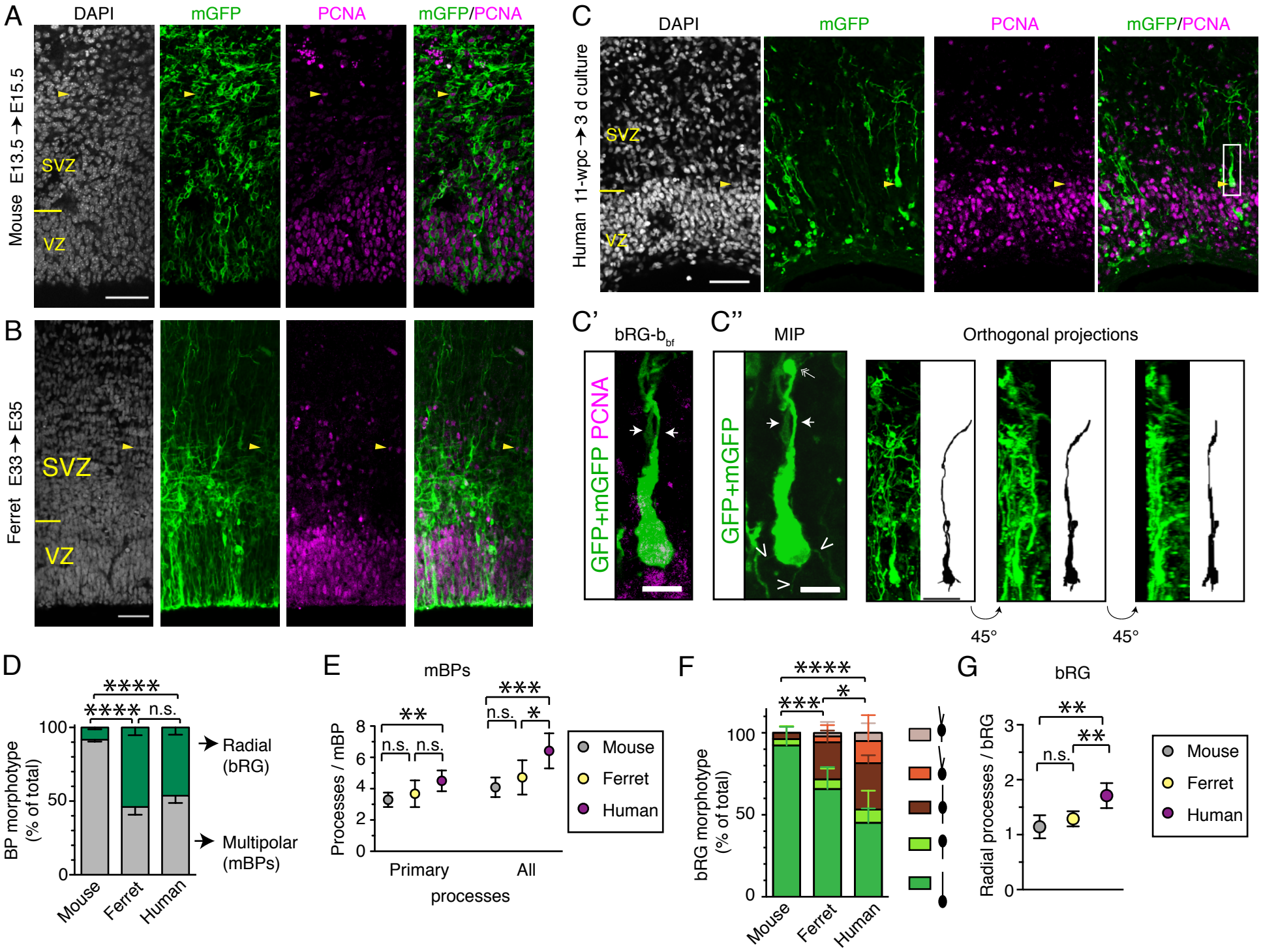
A
DAPI
mGFP
PCNA
mGFP/PCNA
Mouse E13.5 → E15.5
SVZ
VZ
B
Ferret E33 → E35
SVZ
VZ
C
DAPI
mGFP
PCNA
mGFP/PCNA
Human 11-wpc → 3 d culture
SVZ
VZ
C'
bRG-b_bf
GFP+mGFP PCNA
C''
MIP
GFP+mGFP
Orthogonal projections
45°
45°
D
BP morphotype (% of total)
100
50
0
****
****
n.s.
Radial (bRG)
Multipolar (mBPs)
Mouse
Ferret
Human
E
mBPs
Processes / mBP
8
6
4
2
0
**
n.s.
n.s.
***
n.s.
*
Primary
All
processes
Mouse
Ferret
Human
F
bRG morphotype (% of total)
100
50
0
****
***
*
Mouse
Ferret
Human
G
bRG
Radial processes / bRG
3
2
1
0
**
n.s.
**
Mouse
Ferret
Human

Figure 3

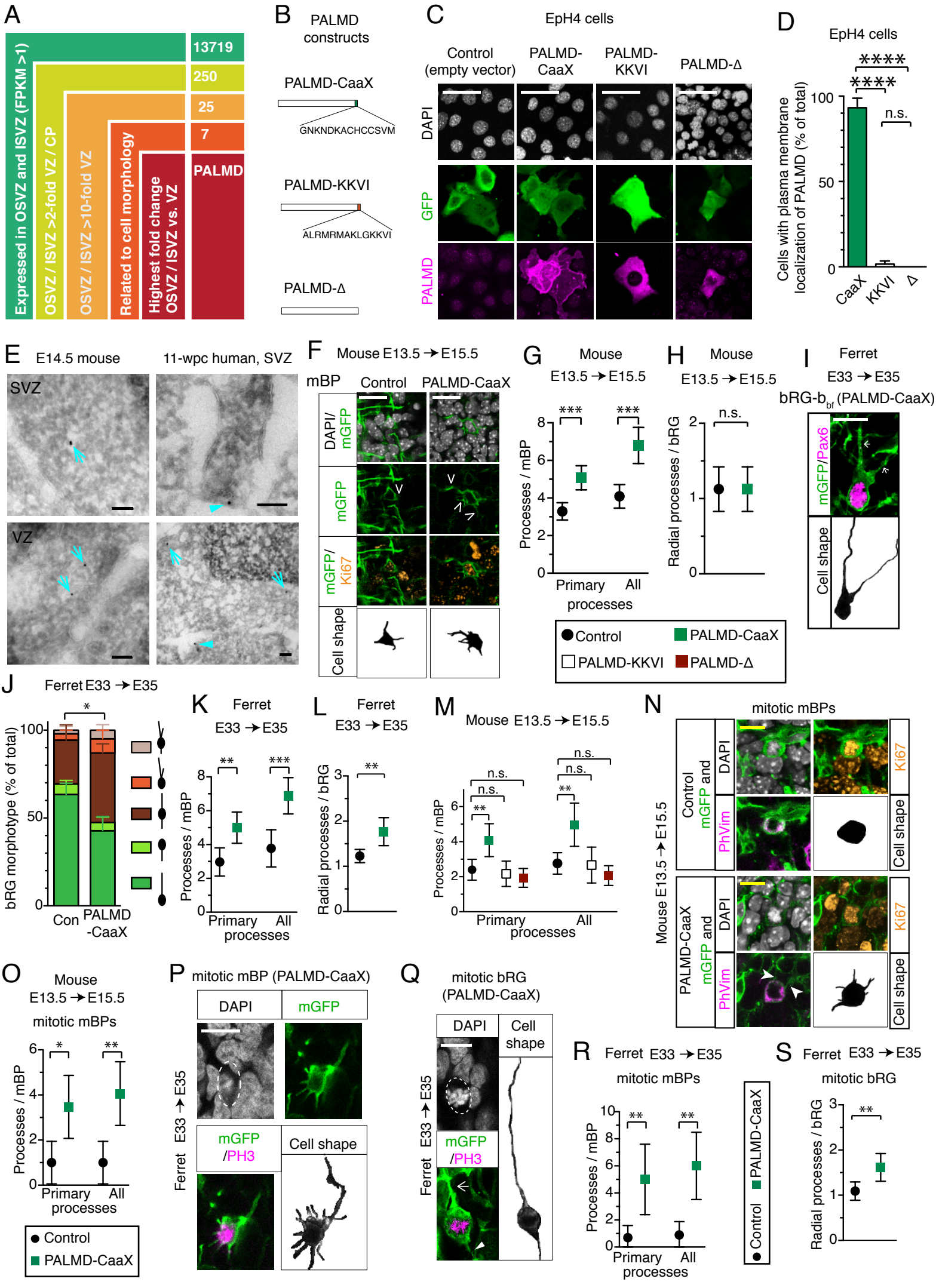
A
Expressed in OSVZ and ISVZ (FPKM >1)
OSVZ / ISVZ >2-fold VZ / CP
OSVZ / ISVZ >10-fold VZ
Related to cell morphology
Highest fold change OSVZ / ISVZ vs. VZ
13719
250
25
7
PALMD
B
PALMD constructs
PALMD-CaaX
GNKNDKACHCCSVM
PALMD-KKVI
ALRMRMAKLGKKVI
PALMD-Δ
C
EpH4 cells
Control (empty vector)
PALMD-CaaX
PALMD-KKVI
PALMD-Δ
DAPI
GFP
PALMD
D
EpH4 cells
Cells with plasma membrane localization of PALMD (% of total)
****
****
n.s.
CaaX
KKVI
Δ
E
E14.5 mouse
11-wpc human, SVZ
SVZ
VZ
F
Mouse E13.5 → E15.5
mBP
Control
PALMD-CaaX
DAPI/ mGFP
mGFP
mGFP/ Ki67
Cell shape
G
Mouse E13.5 → E15.5
Processes / mBP
***
***
Primary processes
All processes
H
Mouse E13.5 → E15.5
Radial processes / bRG
n.s.
Control
PALMD-CaaX
PALMD-KKVI
PALMD-Δ
I
Ferret E33 → E35
bRG-b_bf (PALMD-CaaX)
mGFP/Pax6
Cell shape
J
Ferret E33 → E35
bRG morphotype (% of total)
Con
PALMD -CaaX
K
Ferret E33 → E35
Processes / mBP
Primary processes
All processes
L
Ferret E33 → E35
Radial processes / bRG
M
Mouse E13.5 → E15.5
Processes / mBP
Primary processes
All processes
N
mitotic mBPs
Mouse E13.5 → E15.5
Control mGFP and
PALMD-CaaX mGFP and
DAPI
PhVim
Ki67
Cell shape
O
Mouse E13.5 → E15.5
mitotic mBPs
Processes / mBP
Primary processes
All processes
Control
PALMD-CaaX
P
mitotic mBP (PALMD-CaaX)
Ferret E33 → E35
DAPI
mGFP
mGFP /PH3
Cell shape
Q
mitotic bRG (PALMD-CaaX)
Ferret E33 → E35
DAPI
Cell shape
mGFP /PH3
R
Ferret E33 → E35
mitotic mBPs
Processes / mBP
Primary processes
All processes
Control
PALMD-CaaX
S
Ferret E33 → E35
mitotic bRG
Radial processes / bRG

Figure 4

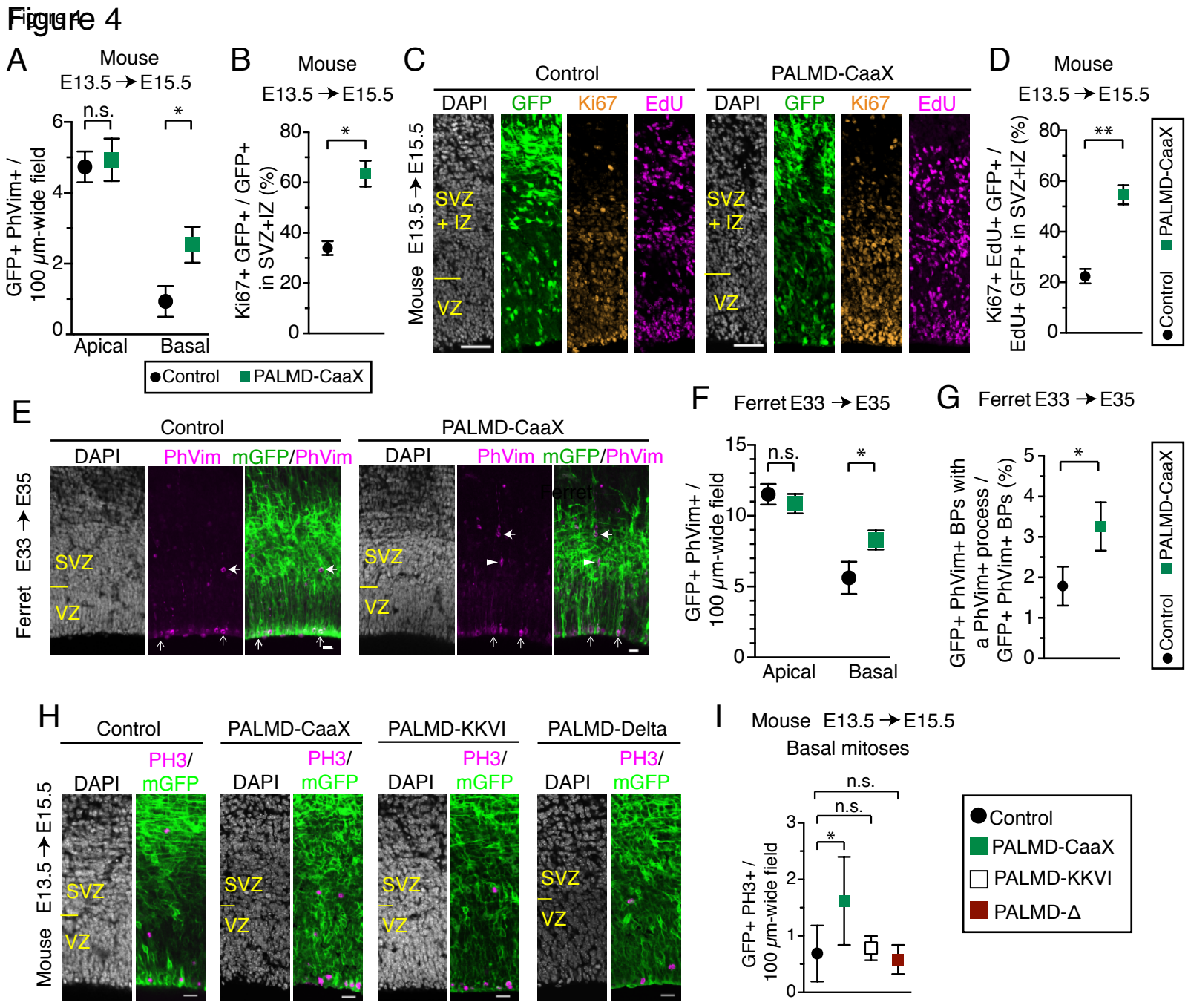
A
Mouse
E13.5 → E15.5
n.s.
*
GFP+ PhVim+ / 100 μm-wide field
Apical
Basal
Control
PALMD-CaaX
B
Mouse
E13.5 → E15.5
*
Ki67+ GFP+ / GFP+ in SVZ+IZ (%)
C
Control
PALMD-CaaX
DAPI
GFP
Ki67
EdU
Mouse E13.5 → E15.5
SVZ + IZ
VZ
D
Mouse
E13.5 → E15.5
**
Ki67+ EdU+ GFP+ / EdU+ GFP+ in SVZ+IZ (%)
Control
PALMD-CaaX
E
Control
PALMD-CaaX
DAPI
PhVim
mGFP/PhVim
Ferret E33 → E35
SVZ
VZ
Ferret
F
Ferret E33 → E35
n.s.
*
GFP+ PhVim+ / 100 μm-wide field
Apical
Basal
G
Ferret E33 → E35
*
GFP+ PhVim+ BPs with a PhVim+ process / GFP+ PhVim+ BPs (%)
Control
PALMD-CaaX
H
Control
PALMD-CaaX
PALMD-KKVI
PALMD-Delta
DAPI
PH3/ mGFP
Mouse E13.5 → E15.5
SVZ
VZ
I
Mouse E13.5 → E15.5
Basal mitoses
n.s.
n.s.
*
GFP+ PH3+ / 100 μm-wide field
Control
PALMD-CaaX
PALMD-KKVI
PALMD-Δ

Figure 5

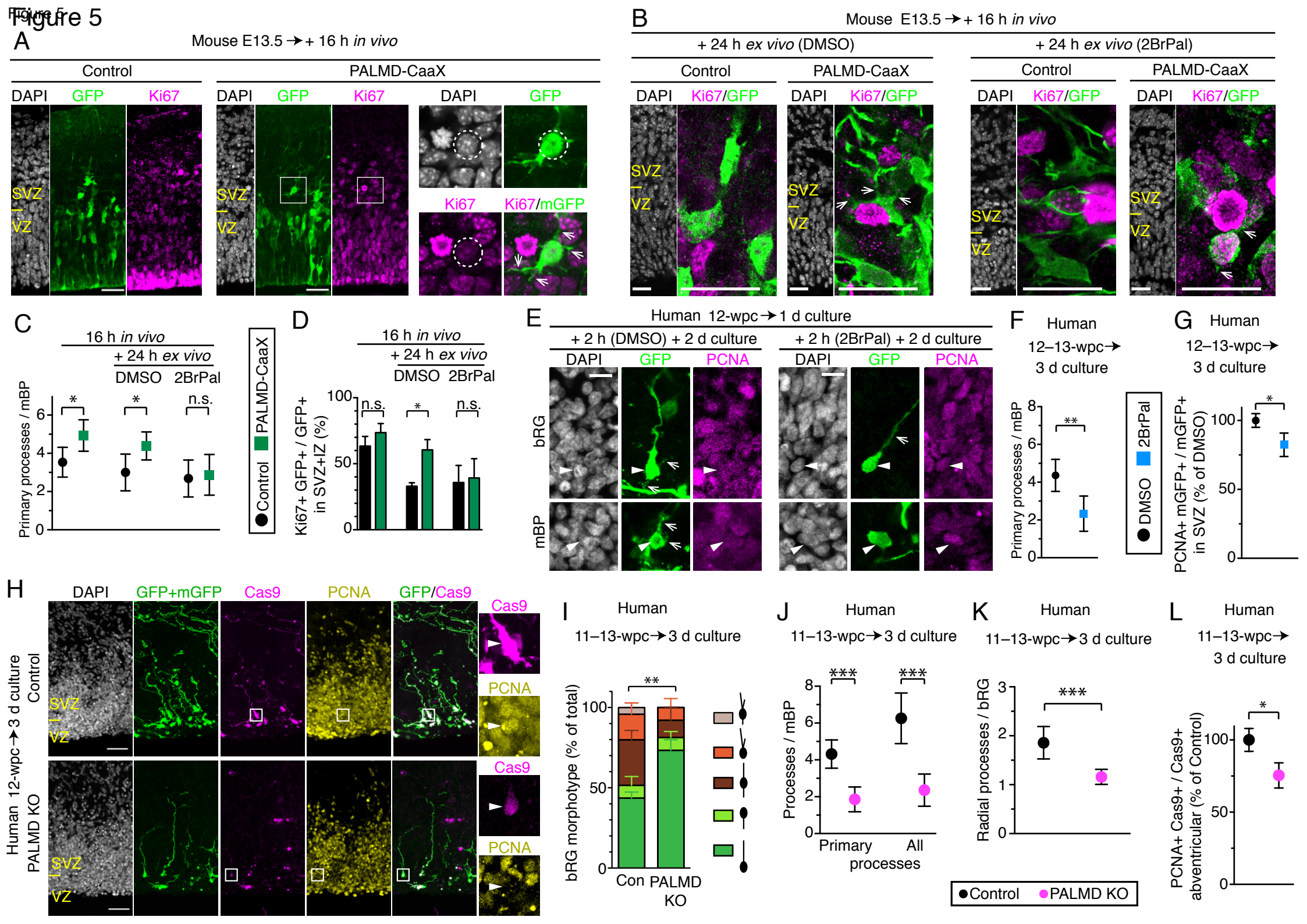
A
Mouse E13.5 → + 16 h in vivo
Control
PALMD-CaaX
DAPI
GFP
Ki67
SVZ
VZ
Ki67/mGFP
B
Mouse E13.5 → + 16 h in vivo
+ 24 h ex vivo (DMSO)
+ 24 h ex vivo (2BrPal)
Ki67/GFP
C
16 h in vivo
+ 24 h ex vivo
DMSO
2BrPal
Primary processes / mBP
n.s.
Control
PALMD-CaaX
D
Ki67+ GFP+ / GFP+ in SVZ+IZ (%)
E
Human 12-wpc → 1 d culture
+ 2 h (DMSO) + 2 d culture
+ 2 h (2BrPal) + 2 d culture
PCNA
bRG
mBP
F
Human
12–13-wpc →
3 d culture
DMSO
2BrPal
G
PCNA+ mGFP+ / mGFP+ in SVZ (% of DMSO)
H
GFP+mGFP
Cas9
GFP/Cas9
Human 12-wpc → 3 d culture
Control
PALMD KO
I
Human
11–13-wpc → 3 d culture
bRG morphotype (% of total)
Con
PALMD KO
J
Processes / mBP
Primary processes
All processes
K
Radial processes / bRG
Control
PALMD KO
L
PCNA+ Cas9+ / Cas9+ abventricular (% of Control)

Figure 6

A

List of top 10 PALMD interactors (PALMD IP from hNcx)			
	Protein (gene name)	Present in Palmd IP	
		from fNcx	from mNcx
1.	*ADD1*	yes	yes
2.	*ADD2*	yes	yes
3.	*KIF4A*	no	no
4.	*FLII*	yes	no
5.	***ADD3***	**yes**	**no**
6.	*LRRFIP1*	no	no
7.	*CLTC*	yes	no
8.	*PALMD*	yes	yes
9.	*MAP2*	no	no
10.	*MGEA5*	no	no

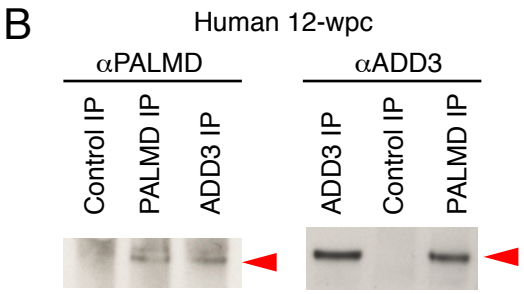

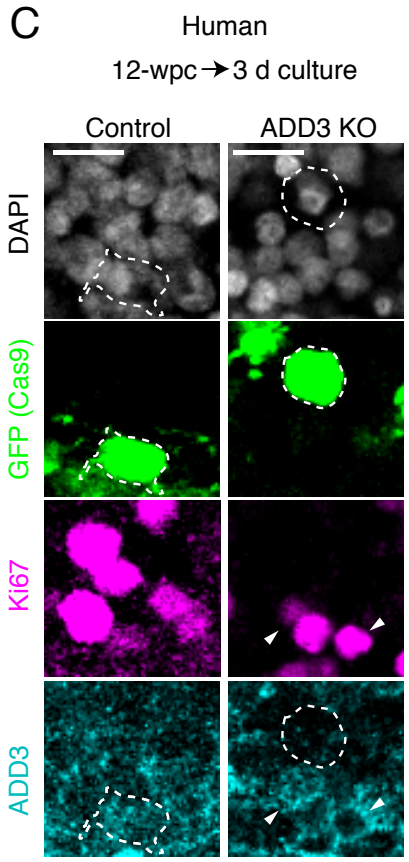

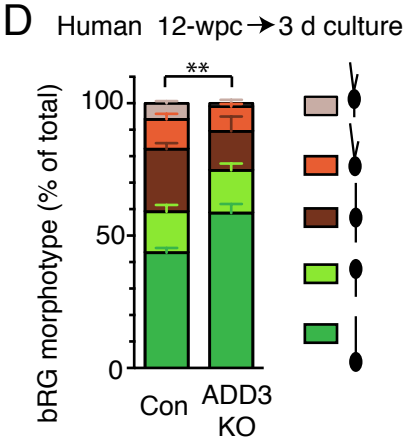

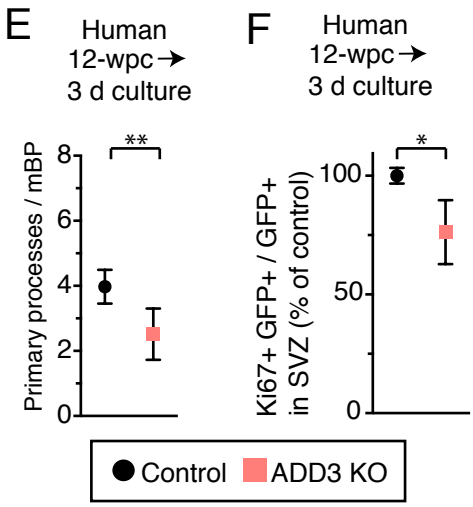

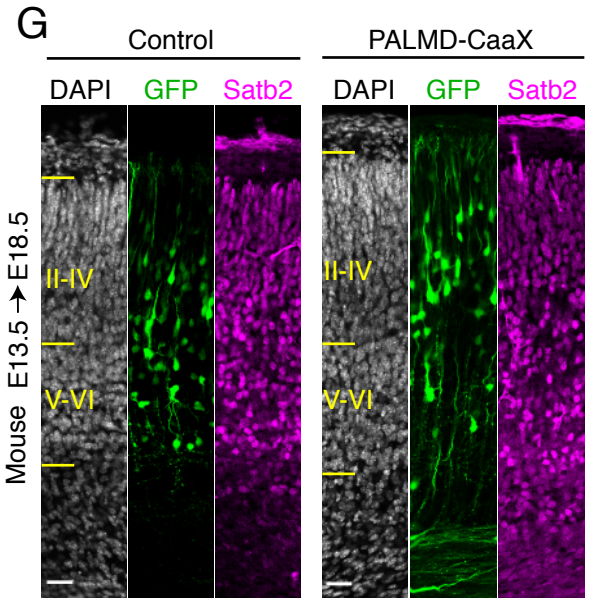

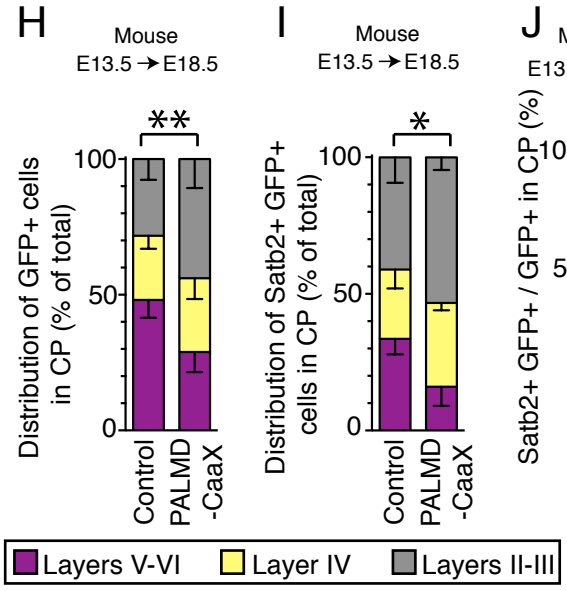

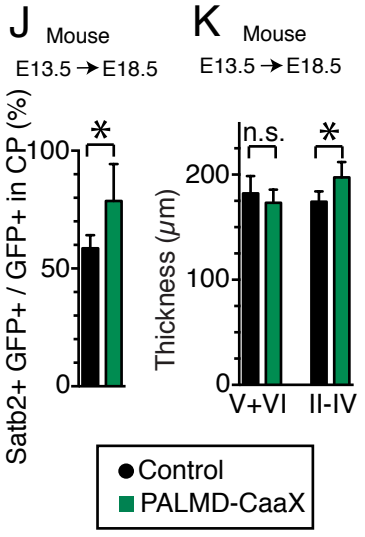

Figure 7

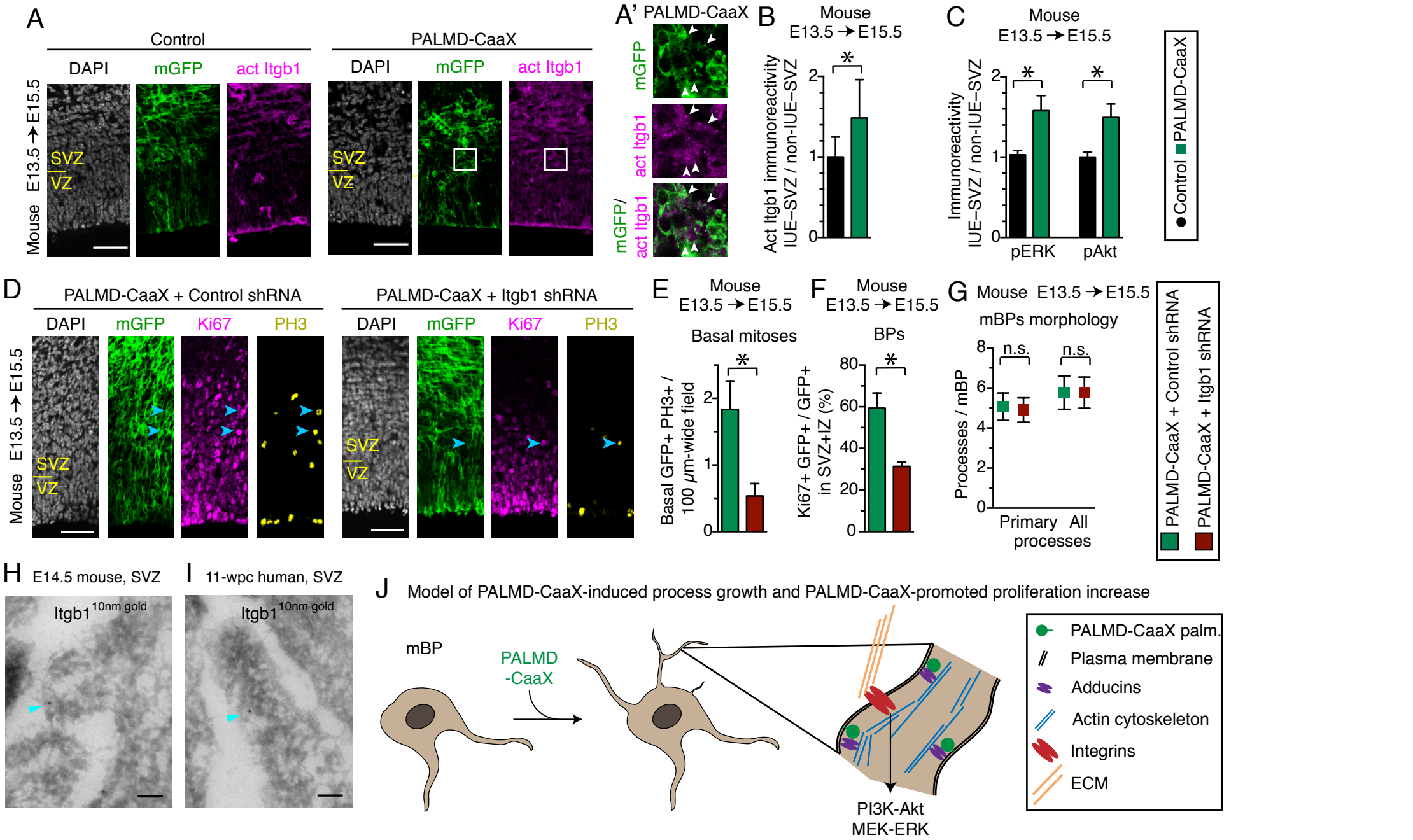
A
Control
PALMD-CaaX
DAPI
mGFP
act Itgb1
Mouse E13.5→E15.5
SVZ
VZ
A' PALMD-CaaX
mGFP
act Itgb1
mGFP/ act Itgb1
B
Mouse E13.5→E15.5
Act Itgb1 immunoreactivity IUE–SVZ / non-IUE–SVZ
C
Mouse E13.5→E15.5
Immunoreactivity IUE–SVZ / non-IUE–SVZ
pERK
pAkt
Control
PALMD-CaaX
D
PALMD-CaaX + Control shRNA
PALMD-CaaX + Itgb1 shRNA
DAPI
mGFP
Ki67
PH3
E
Mouse E13.5→E15.5
Basal mitoses
Basal GFP+ PH3+ / 100 μm-wide field
F
Mouse E13.5→E15.5
BPs
Ki67+ GFP+ / GFP+ in SVZ+IZ (%)
G
Mouse E13.5→E15.5
mBPs morphology
Processes / mBP
n.s.
Primary processes
All processes
PALMD-CaaX + Control shRNA
PALMD-CaaX + Itgb1 shRNA
H
E14.5 mouse, SVZ
Itgb1 10nm gold
I
11-wpc human, SVZ
Itgb1 10nm gold
J
Model of PALMD-CaaX-induced process growth and PALMD-CaaX-promoted proliferation increase
mBP
PALMD -CaaX
PI3K-Akt
MEK-ERK
PALMD-CaaX palm.
Plasma membrane
Adducins
Actin cytoskeleton
Integrins
ECM

Figure S1

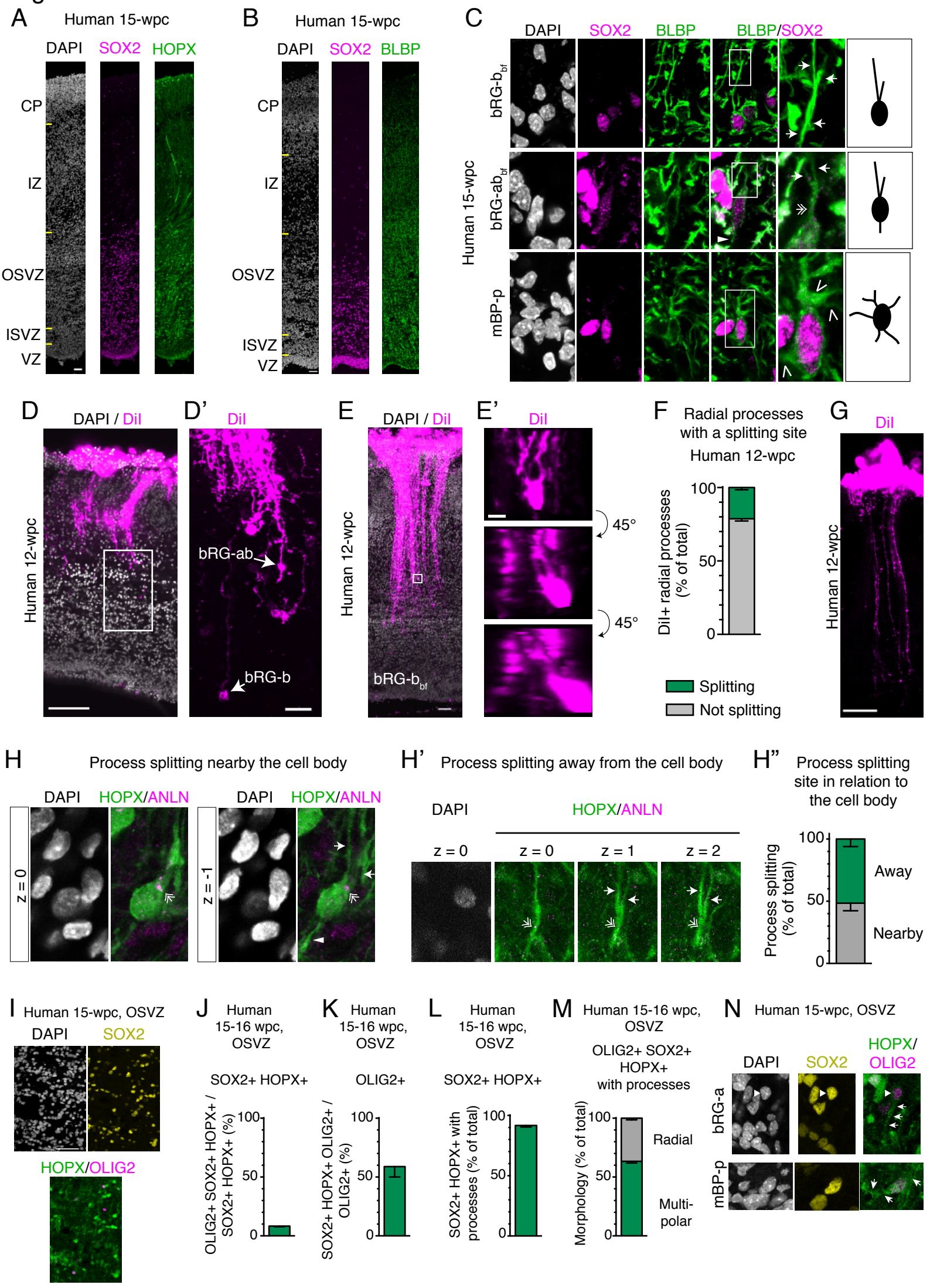
A
Human 15-wpc
DAPI SOX2 HOPX
CP
IZ
OSVZ
ISVZ
VZ
B
Human 15-wpc
DAPI SOX2 BLBP
CP
IZ
OSVZ
ISVZ
VZ
C
DAPI SOX2 BLBP BLBP/SOX2
Human 15-wpc
bRG-b_bf
bRG-ab_bf
mBP-p
D
DAPI / DiI
Human 12-wpc
D'
DiI
bRG-ab
bRG-b
E
DAPI / DiI
Human 12-wpc
bRG-b_bf
E'
DiI
45°
45°
F
Radial processes with a splitting site
Human 12-wpc
DiI+ radial processes (% of total)
100
50
0
Splitting
Not splitting
G
DiI
Human 12-wpc
H
Process splitting nearby the cell body
DAPI HOPX/ANLN
z = 0
DAPI HOPX/ANLN
z = -1
H'
Process splitting away from the cell body
DAPI
HOPX/ANLN
z = 0
z = 0
z = 1
z = 2
H"
Process splitting site in relation to the cell body
Process splitting (% of total)
100
50
0
Away
Nearby
I
Human 15-wpc, OSVZ
DAPI SOX2
HOPX/OLIG2
J
Human 15-16 wpc, OSVZ
SOX2+ HOPX+
OLIG2+ SOX2+ HOPX+ / SOX2+ HOPX+ (%)
100
50
0
K
Human 15-16 wpc, OSVZ
OLIG2+
SOX2+ HOPX+ OLIG2+ / OLIG2+ (%)
100
50
0
L
Human 15-16 wpc, OSVZ
SOX2+ HOPX+
SOX2+ HOPX+ with processes (% of total)
100
50
0
M
Human 15-16 wpc, OSVZ
OLIG2+ SOX2+ HOPX+ with processes
Morphology (% of total)
100
50
0
Radial
Multi-polar
N
Human 15-wpc, OSVZ
DAPI SOX2 HOPX/ OLIG2
bRG-a
mBP-p

Figure S2

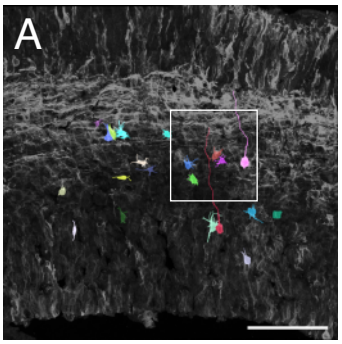

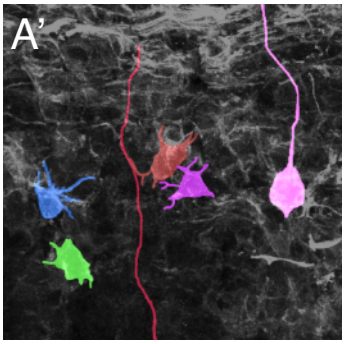

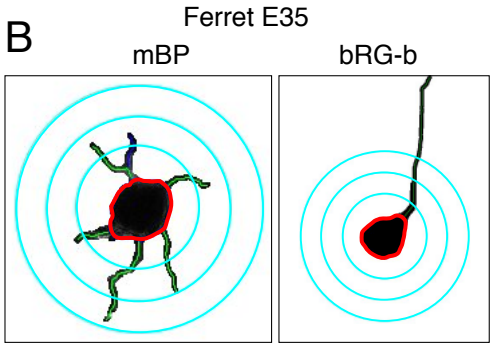

Parameter	mBP	bRG-b
No. prim. proc.:	5	1
No. all proc.:	6	1
branching index:	1.2	1.0
Sholl 2r:	6	1
Sholl 3r:	1	1
Sholl 4r:	0	1

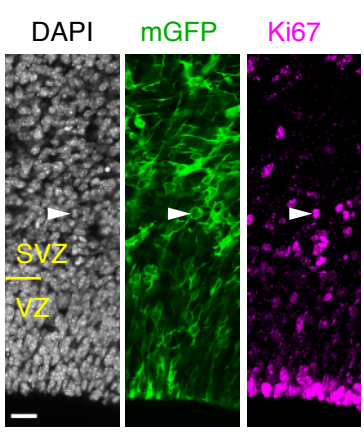

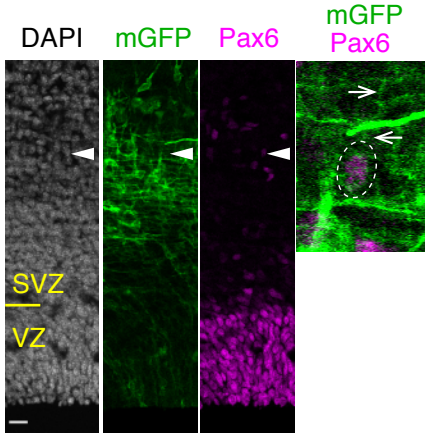

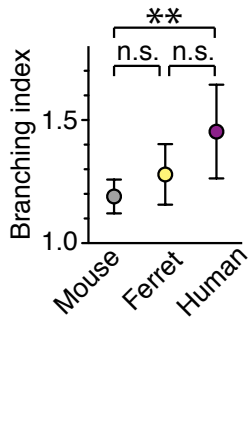

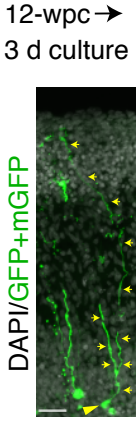

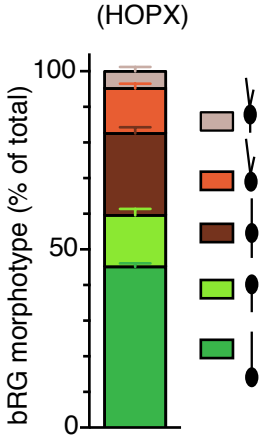

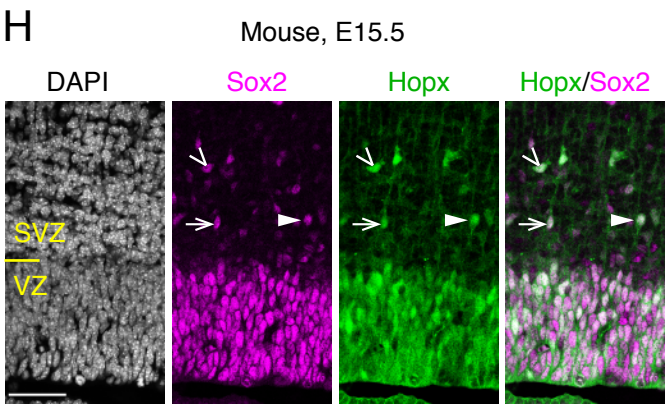

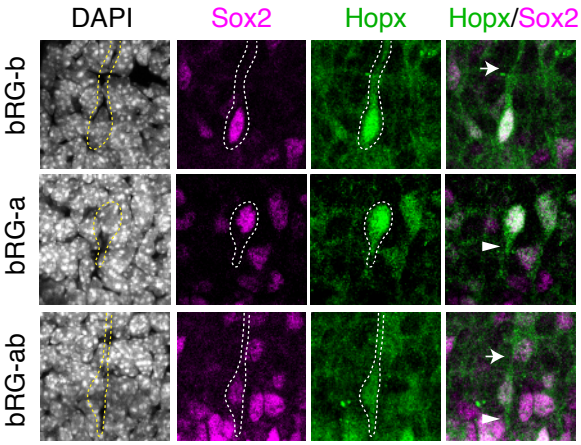

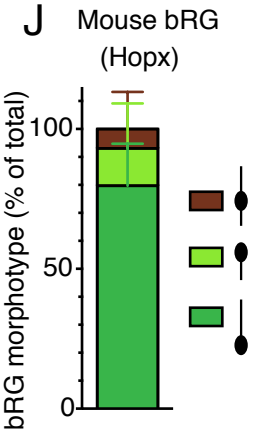

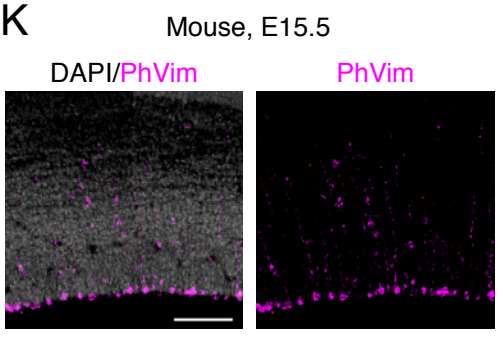

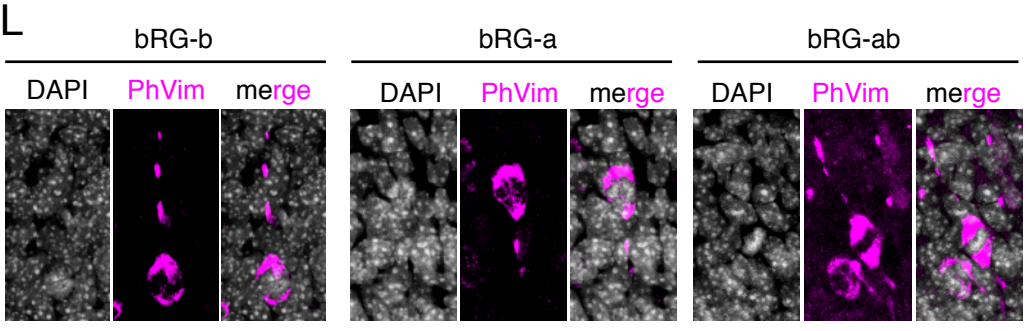

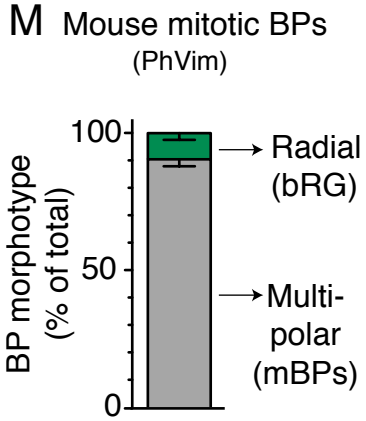

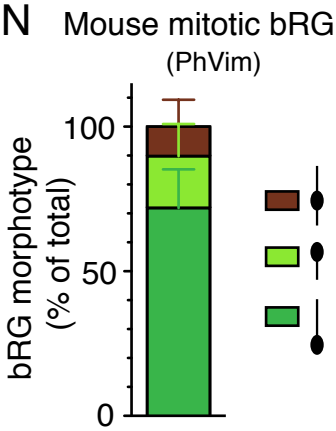

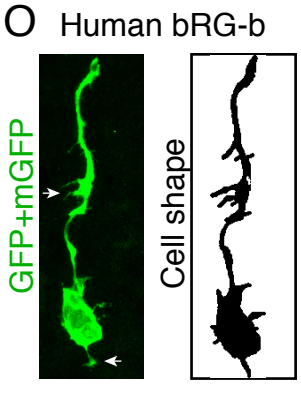

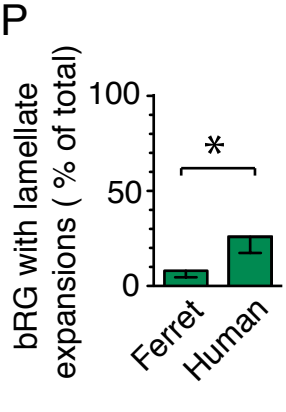

Figure S3

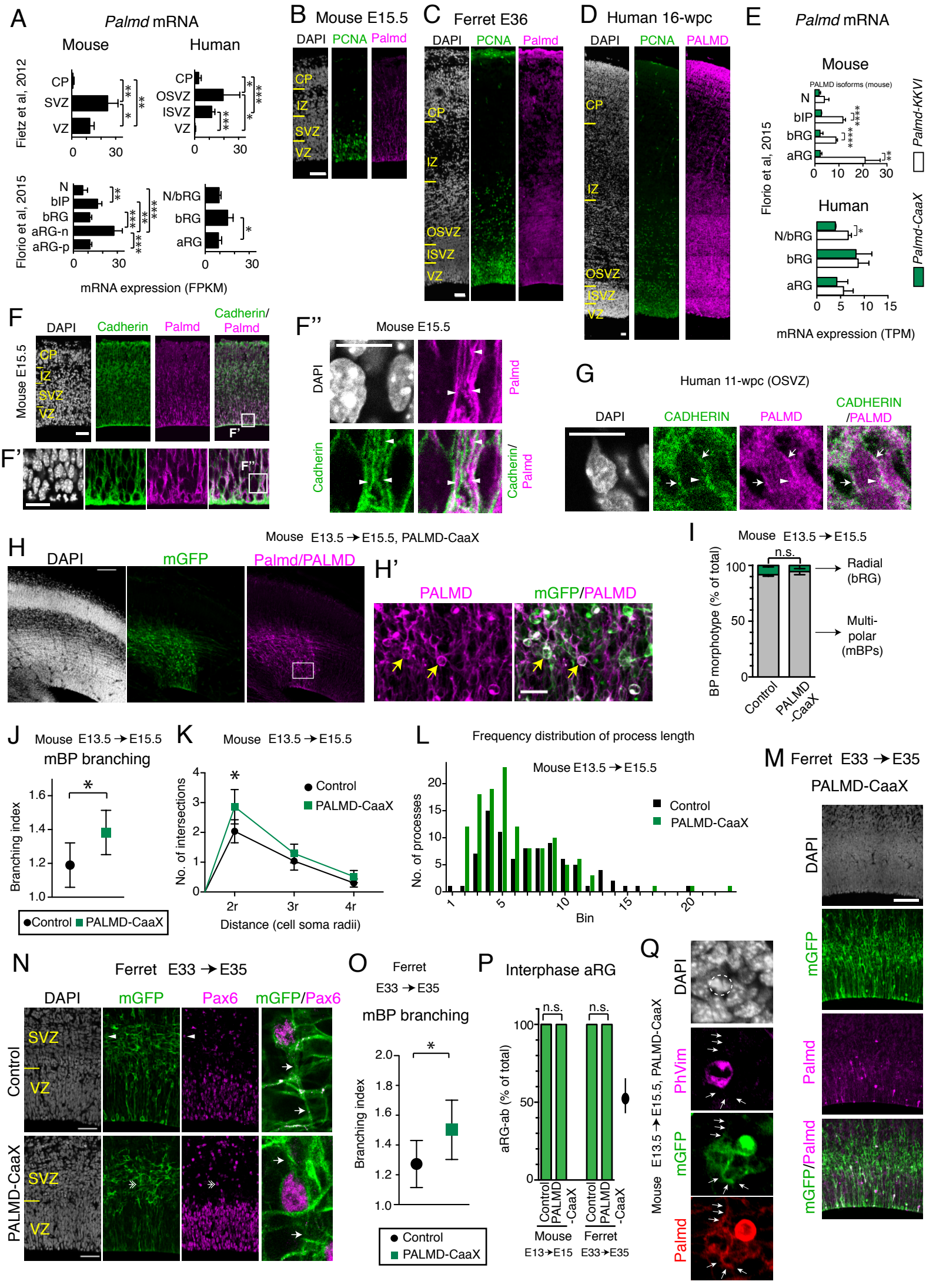
A
Palmd mRNA
Mouse
Human
Fietz et al, 2012
CP
SVZ
VZ
OSVZ
ISVZ
Florio et al, 2015
N
bIP
bRG
aRG-n
aRG-p
N/bRG
aRG
mRNA expression (FPKM)
B Mouse E15.5
DAPI PCNA Palmd
CP
IZ
SVZ
VZ
C Ferret E36
DAPI PCNA Palmd
OSVZ
ISVZ
D Human 16-wpc
DAPI PCNA PALMD
E
Palmd mRNA
Mouse
PALMD isoforms (mouse)
Florio et al, 2015
Palmd-KKVI
Palmd-CaaX
Human
N/bRG
bRG
aRG
mRNA expression (TPM)
F
DAPI Cadherin Palmd Cadherin/ Palmd
Mouse E15.5
F'
F''
F'' Mouse E15.5
DAPI
Palmd
Cadherin
Cadherin/ Palmd
G
Human 11-wpc (OSVZ)
DAPI CADHERIN PALMD CADHERIN /PALMD
H
Mouse E13.5→E15.5, PALMD-CaaX
DAPI mGFP Palmd/PALMD
H'
PALMD mGFP/PALMD
I
Mouse E13.5→E15.5
BP morphotype (% of total)
n.s.
Radial (bRG)
Multi-polar (mBPs)
Control
PALMD -CaaX
J
Mouse E13.5→E15.5
mBP branching
Branching index
Control PALMD-CaaX
K
Mouse E13.5→E15.5
No. of intersections
Control
PALMD-CaaX
Distance (cell soma radii)
L
Frequency distribution of process length
Mouse E13.5→E15.5
No. of processes
Control
PALMD-CaaX
Bin
M
Ferret E33→E35
PALMD-CaaX
DAPI
mGFP
Palmd
mGFP/Palmd
N
Ferret E33→E35
DAPI mGFP Pax6 mGFP/Pax6
Control
PALMD-CaaX
SVZ
VZ
O
Ferret
E33→E35
mBP branching
Branching index
Control
PALMD-CaaX
P
Interphase aRG
aRG-ab (% of total)
n.s.
Control
PALMD -CaaX
Mouse E13→E15
Ferret E33→E35
Q
Mouse E13.5→E15.5, PALMD-CaaX
DAPI
PhVim
mGFP
Palmd

Figure S4

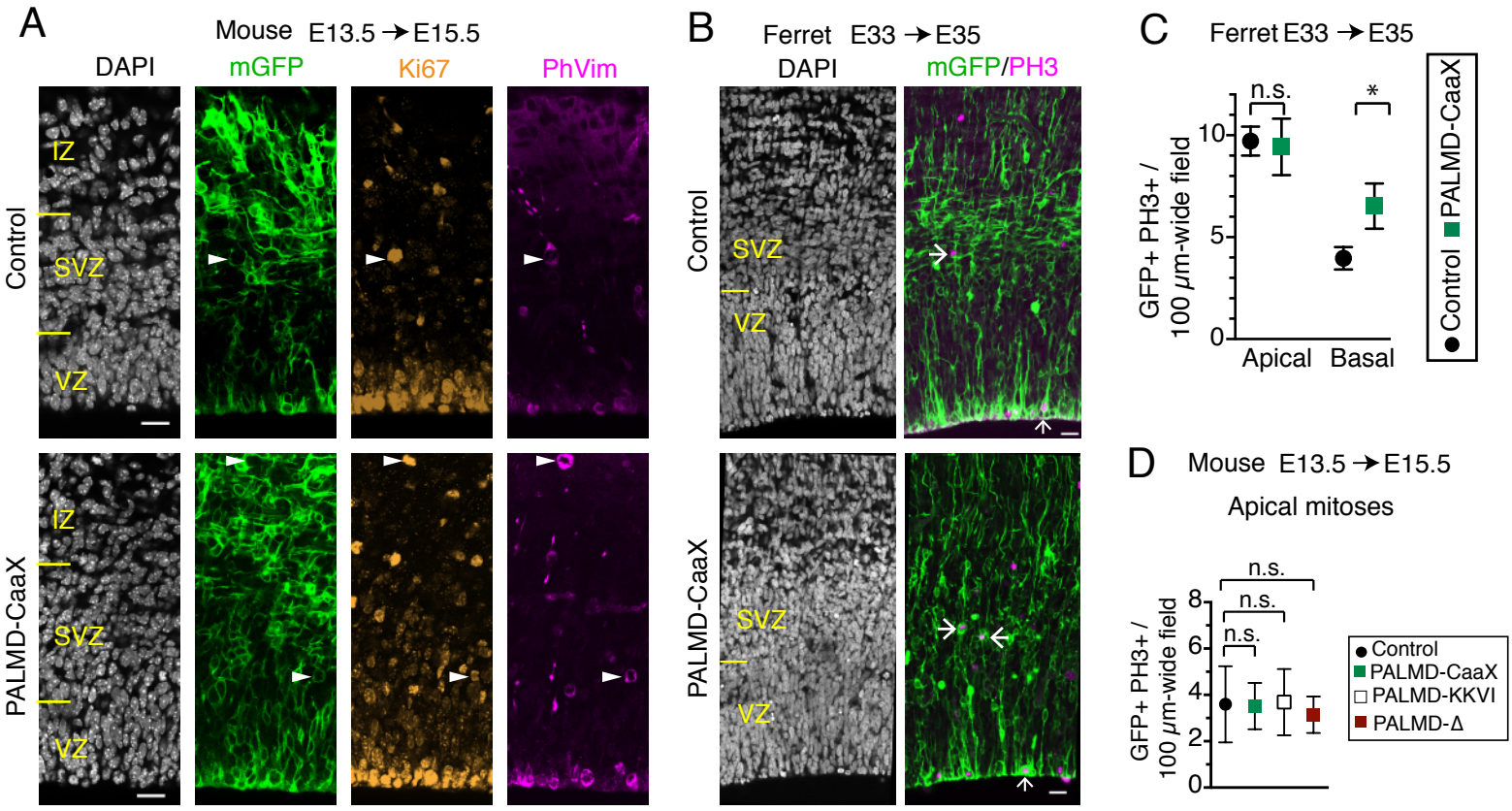
A
Mouse E13.5 → E15.5
DAPI
mGFP
Ki67
PhVim
Control
PALMD-CaaX
IZ
SVZ
VZ
B
Ferret E33 → E35
DAPI
mGFP/PH3
C
Ferret E33 → E35
n.s.
*
GFP+ PH3+ / 100 μm-wide field
Apical
Basal
Control
PALMD-CaaX
D
Mouse E13.5 → E15.5
Apical mitoses
n.s.
GFP+ PH3+ / 100 μm-wide field
Control
PALMD-CaaX
PALMD-KKVI
PALMD-Δ

Figure S5

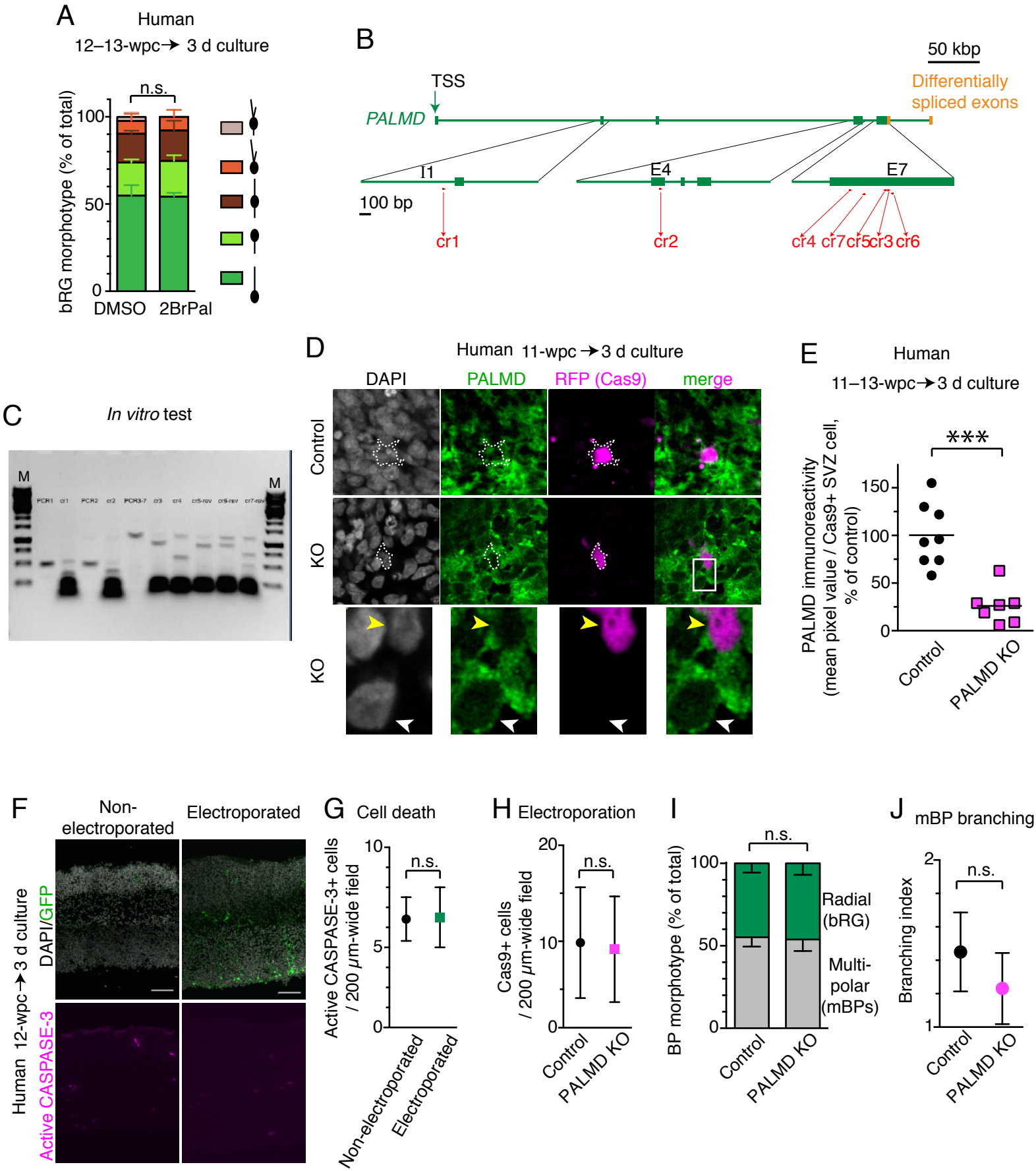
A
Human
12–13-wpc→ 3 d culture
n.s.
bRG morphotype (% of total)
100
50
0
DMSO
2BrPal
B
50 kbp
TSS
PALMD
Differentially spliced exons
I1
E4
E7
100 bp
cr1
cr2
cr4 cr7 cr5 cr3 cr6
C
In vitro test
M
M
D
Human 11-wpc→3 d culture
DAPI
PALMD
RFP (Cas9)
merge
Control
KO
KO
E
Human
11–13-wpc→3 d culture
***
PALMD immunoreactivity (mean pixel value / Cas9+ SVZ cell, % of control)
150
100
50
0
Control
PALMD KO
F
Non-electroporated
Electroporated
Human 12-wpc→3 d culture
DAPI/GFP
Active CASPASE-3
G
Cell death
Active CASPASE-3+ cells / 200 μm-wide field
10
5
0
n.s.
Non-electroporated
Electroporated
H
Electroporation
Cas9+ cells / 200 μm-wide field
20
10
0
n.s.
Control
PALMD KO
I
n.s.
BP morphotype (% of total)
100
50
0
Radial (bRG)
Multi-polar (mBPs)
Control
PALMD KO
J
mBP branching
Branching index
2
1
n.s.
Control
PALMD KO

Figure S6

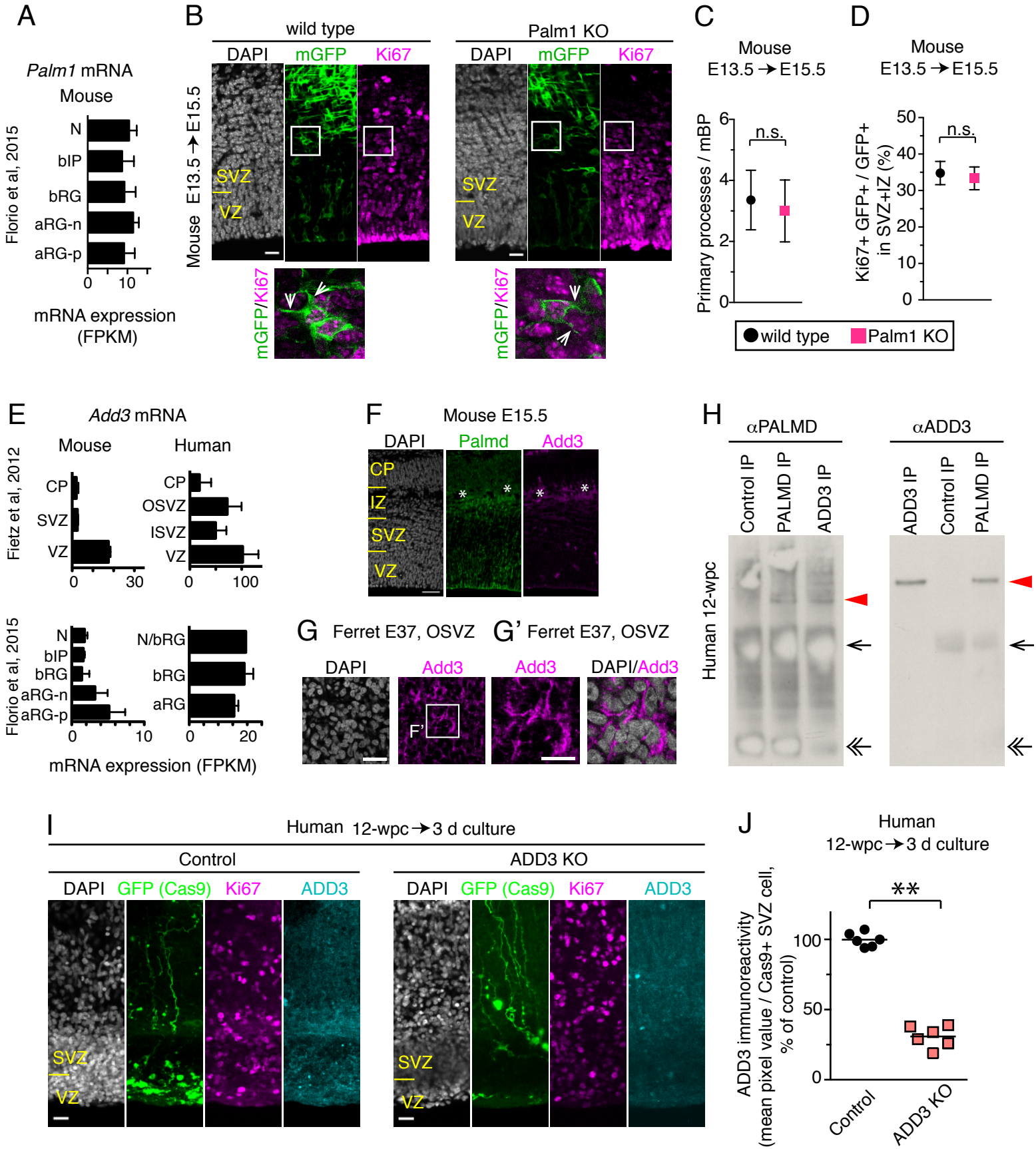
A
Palm1 mRNA
Mouse
Florio et al, 2015
N
bIP
bRG
aRG-n
aRG-p
0
10
mRNA expression (FPKM)
B
wild type
Palm1 KO
DAPI
mGFP
Ki67
Mouse E13.5 → E15.5
SVZ
VZ
mGFP/Ki67
C
Mouse E13.5 → E15.5
Primary processes / mBP
n.s.
D
Mouse E13.5 → E15.5
Ki67+ GFP+ / GFP+ in SVZ+IZ (%)
n.s.
wild type
Palm1 KO
E
Add3 mRNA
Mouse
Human
Fietz et al, 2012
CP
SVZ
VZ
OSVZ
ISVZ
Florio et al, 2015
N
bIP
bRG
aRG-n
aRG-p
N/bRG
bRG
aRG
mRNA expression (FPKM)
F
Mouse E15.5
DAPI
Palmd
Add3
CP
IZ
SVZ
VZ
G
Ferret E37, OSVZ
G'
Ferret E37, OSVZ
DAPI
Add3
DAPI/Add3
F'
H
αPALMD
αADD3
Control IP
PALMD IP
ADD3 IP
Human 12-wpc
I
Human 12-wpc → 3 d culture
Control
ADD3 KO
DAPI
GFP (Cas9)
Ki67
ADD3
SVZ
VZ
J
Human
12-wpc → 3 d culture
ADD3 immunoreactivity (mean pixel value / Cas9+ SVZ cell, % of control)
**
Control
ADD3 KO

Figure S7

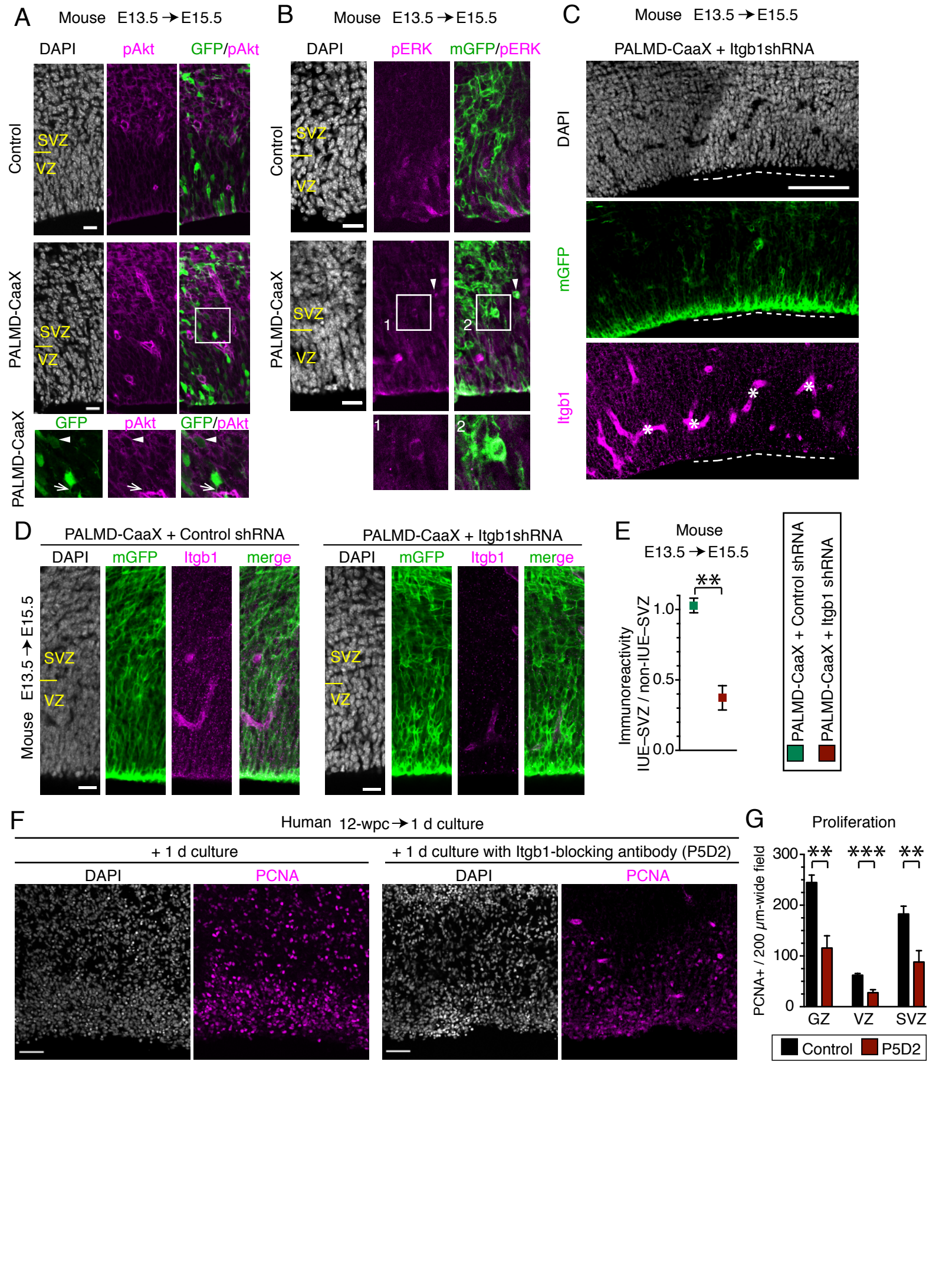
A
Mouse E13.5 → E15.5
DAPI
pAkt
GFP/pAkt
Control
PALMD-CaaX
SVZ
VZ
GFP
B
Mouse E13.5 → E15.5
DAPI
pERK
mGFP/pERK
1
2
C
Mouse E13.5 → E15.5
PALMD-CaaX + Itgb1shRNA
DAPI
mGFP
Itgb1
D
PALMD-CaaX + Control shRNA
PALMD-CaaX + Itgb1shRNA
DAPI
mGFP
Itgb1
merge
Mouse E13.5 → E15.5
E
Mouse
E13.5 → E15.5
**
Immunoreactivity
IUE–SVZ / non-IUE–SVZ
1.0
0.5
0.0
PALMD-CaaX + Control shRNA
PALMD-CaaX + Itgb1 shRNA
F
Human 12-wpc → 1 d culture
+ 1 d culture
+ 1 d culture with Itgb1-blocking antibody (P5D2)
DAPI
PCNA
G
Proliferation
PCNA+ / 200 μm-wide field
300
200
100
0
**
***
**
GZ
VZ
SVZ
Control
P5D2

Table S1 Related to Figure 3. Genes enriched in the fetal human OSVZ/ISVZ vs. VZ/CP.

Ensembl Gene ID	Gene name	VZ	ISVZ	OSVZ	CP
ENSG00000099260	*PALMD*	0,207	11,673	19,459	2,744
ENSG00000214595	*EML6*	0,192	9,379	15,604	1,005
ENSG00000099250	*NRP1*	0,642	22,726	47,852	4,285
ENSG00000213906	*LTB4R2*	0,060	1,225	3,369	0,028
ENSG00000123243	*ITIH5*	0,131	3,738	4,850	0,742
ENSG00000091664	*SLC17A6*	0,372	19,615	13,617	0,103
ENSG00000232044	*AC073479.1*	0,830	29,970	25,053	6,437
ENSG00000137491	*SLCO2B1*	0,213	5,236	5,782	1,586
ENSG00000182379	*NXPH4*	0,695	33,174	16,629	6,028
ENSG00000100314	*CABP7*	0,437	9,916	9,203	3,330
ENSG00000137801	*THBS1*	4,044	47,078	73,338	5,144
ENSG00000124785	*NRN1*	4,446	147,496	76,222	29,823
ENSG00000233863	*AC012215.1*	1,842	22,950	30,273	6,220
ENSG00000183775	*KCTD16*	0,222	2,667	3,405	0,803
ENSG00000044524	*EPHA3*	2,886	32,716	43,142	12,004
ENSG00000106341	*C7orf16*	7,034	189,600	105,121	0,842
ENSG00000173930	*SLCO4C1*	0,108	2,061	1,474	0,000
ENSG00000244055	*AC007566.10*	0,565	5,786	7,666	2,538
ENSG00000204624	*PTCHD2*	5,283	69,449	66,439	11,801
ENSG00000117971	*CHRNB4*	0,278	4,494	3,366	0,186
ENSG00000134531	*EMP1*	0,227	2,340	2,538	0,487
ENSG00000080644	*CHRNA3*	0,186	3,504	2,017	0,000
ENSG00000154133	*ROBO4*	0,268	3,218	2,793	0,752
ENSG00000137142	*IGFBPL1*	23,305	263,791	240,633	65,951
ENSG00000130429	*ARPC1B*	0,471	10,586	4,739	1,307

Table S2 Related to Figure 6. List of Palmd interactors in hNcx, fNcx and mNcx

HUMAN IP										
Protein name	**Gene name**	**MW (kDa)**	**Exp. 1**		**Exp. 2**		**Exp. 3**		**Ferret IP**	**Mouse IP**
			UP	TS	UP	TS	UP	TS		
Beta-adducin	*ADD2*	81	30	140	21	68	23	115	yes	yes
Alpha-adducin	*ADD1*	84	17	139	17	83	14	100	yes	yes
Kinesin KIF4A	*KIF4A*	140	18	23	17	22	9	13	no	no
Flightless-1 homolog	*FLII*	138	8	8	10	11	6	6	yes	no
Gamma-adducin	*ADD3*	79	6	10	5	6	3	4	yes	no
Leucine-rich repeat flightless interactin protein 1	*LRRFIP1*	86	6	10	5	6	1	1	no	no
Clathrin heavy chain 1	*CLTC*	188	1	1	8	9	3	3	yes	no
Palmdelphin	*PALMD*	63	8	8	3	5	1	2	yes	yes
MAP2	*MAP2*	199	11	13	1	1	1	1	no	no
Protein O-GlcNAcase	*MGEA5*	103	5	7	7	10	1	1	no	no
ADE2	*PAICS*	47	2	2	3	3	1	1	no	no
TFIID subunit 5	*TAF5*	87	1	1	3	4	2	2	yes	no
CSTF subunit 3	*CSTF3*	83	4	5	1	1	1	1	yes	no
Pyruvate kinase	*PKM*	58	4	4	1	1	8	8	no	no
EPS15L1	*EPS15L1*	66	4	4	1	1	1	2	no	no
TFIID subunit 6	*TAF6*	110	2	3	1	1	1	1	no	no
Epididymis luminal protein 4	*YWHAZ*	28	1	2	1	1	6	14	no	no
Alpha-2-macroglobulin	*A2M*	163	1	1	1	2	1	1	no	no
Immunoglobulin heavy variable 3-72	*IGHV3-72*	13	1	5	1	6	1	4	no	no
Stathmin	*STMN1*	20	1	1	1	2	1	2	no	no
40S ribosomal protein S14	*RPS14*	13	1	1	1	1	1	2	no	no

FERRET IP			
Protein name	**Gene name**	**MW (kDa)**	**UP**
PTPRF interacting protein alpha	*Ppfia3*	137	17
Beta-adducin	*Add2*	80	16
Alpha-adducin	*Add1*	85	13
Meningioma expressed antigen 5	*Mgea5*	103	7
Ceruloplasmin	*Cp*	124	6
Flightless-1 homolog	*Fliil*	145	6
Malonyl-CoA decarboxylase	*Mlycd*	39	6
Complement C3	*C3*	188	5
Kinesin-like protein	*Kif2c*	81	5
TATA-box binding protein assoc. factor 5	*Taf5*	87	5
WD repeat domain 11	*Wdr11*	134	5
Nucleotide binding protein like	*Nubpl*	35	5
Gamma-adducin	*Add3*	79	4

MOUSE IP			
Protein name	**Gene name**	**MW (kDa)**	**UP**
Nestin	*Nes*	207	73
Treacle protein	*Tcof1*	139	33
Band 4.1-like protein 2	*Epb41l2*	110	23
Alpha-adducin	*Add1*	81	19
Beta-adducin	*Add2*	81	17
ASH2 like	*Ash2l*	68	16
BAG6	*Bag6*	121	15
Annexin A2	*Anxa2*	39	12
Gamma-tubulin complex comp. 3	*Tubgcp3*	103	11
Transglutaminase I	*Tgm1*	90	11
Rb-binding protein 5	*Rbbp5*	59	9
Gamma-tubulin complex comp. 2	*Tubgcp2*	103	9
Lamin-B receptor	*Lbr*	71	8

Table S3 Related to STAR Methods. List of oligonucleotides used.

Oligonucleotide	Sequence
Palmd cloning primers	
Palmd cloning primer Palmd_SpHI_Fw	AGATGCATGCGCCGCCATGGAAGAAGCTGAG
Palmd cloning primer KKVI_BsrGI_Rev	CCCGCTGTACATTAGATCACCTT
Palmd cloning primer CAAX_BsrGI_Rev	CCCGCTGTACATCACATGACTG
Palmd mutagenesis primers	
Palmd mutagen. primer Del-C-sense	CTGAGGATCCATCCTTAACAGCTTTAAGGATGAGAATGG
Palmd mutagen. primer Del-C-antisense	CCATTCTCATCCTTAAAGCTGTTAAGGATGGATCCTCAG
Palmd gRNAs	
Palmd gRNA cr1	TGCCAAAAAAATATCAGTAACGG
Palmd gRNA cr2	AGAAACTAAAGTCAATTGAGCGG
Palmd gRNA cr3	AGCTTCACACCCCGCAAAAAAGG
Palmd gRNA cr4	GCAGCATACAATGGCACCGATGG
Palmd gRNA cr5	GCTTGTTGAATCACTGATCGGGG
Palmd gRNA cr6	GAGTCATTAGCCTTTTTTGCGGG
Palmd gRNA cr7	TGGGGTTGTAGGCCTGTAAAAGG
CRISPR test primers	
CRISPR test Primer for PCR1 Fw	GCTAGACTAATGGGGAAGAAGGA
CRISPR test Primer for PCR1 Rev	GTTGGCCTCCCCTATGGTTA
CRISPR test Primer for PCR2 Fw	ACTCCGCATTTGTACTGTGTT
CRISPR test Primer for PCR2 Rev	GGACTTTGGAAGGTCAGGGA
CRISPR test Primer for PCR3 Fw	CTTTGCCCACTGTGATGCAC
CRISPR test Primer for PCR3 Rev	TCACTGTCTTCTGCCTGCTG

Figure S1 Related to Figure 1. Analyses of human proliferative BP morphology.

(A) DAPI staining and IF for SOX2 and HOPX of 15-wpc hNcx.

(B, C) DAPI staining and IF for SOX2 and BLBP of 15-wpc hNcx. (B) Overview. (C) Examples of bRG-b_{bf}, bRG-ab_{bf} and mBP-p (see schemes). The 4 left-most images in each row are 50 µm wide, whereas each right image represents the area indicated by the respective box and is 9.25 µm (bRG-b_{bf}), 7 µm (bRG-ab_{bf}) or 10 µm (mBP-p) wide. Double arrow, single basal process leaving the cell body and bifurcating more basally into two processes; arrows, two basal processes either beyond the bifurcation point (bRG-ab_{bf}) or intertwined around each other (bRG-b_{bf}); solid arrowhead, apical process; open arrowheads, short processes of the mBP-p. All images are oriented with the apical side facing down.

(D-G) Sparse DiI labeling of 12-wpc hNcx from the basal side, combined with DAPI staining (in D and E). Boxes in (D) and (E), areas shown at higher magnification in (D') and (E'), respectively. (E') Enlarged view of the bRG-b_{bf}; top, same orientation as in (E); middle and bottom, rotations by 45° and 90°, respectively, to demonstrate the 3-dimensional structure of the processes. See also supplemental movies 2 and 3. (F) Quantification of DiI+ radial processes of bRG with respect to the presence of a splitting site (for details, see Methods). (G) An example of a SOpS section of DiI-labeled 12-wpc hNcx.

(H-H") Cell biological analysis of the human bRG morphotypes identified here – bRG-b_{bf} and bRG-ab_{bf} (collectively termed bRG-(a)b_{bf}). The IF and DiI labeling described in (A-G) and in Figure 1 had revealed that bRG-(a)b_{bf} come in two different forms, (i) with two independent basal processes leaving the cell body (Figures 1A and S1E), and (ii) with a single basal process leaving the cell body, which then splits into two processes (Figures 1B and S1C middle). From a cell biological point of view, two basal processes can result from either splitting the originally single basal process in the apical direction, as previously reported for mouse neuroepithelial cells (Kosodo et al., 2008), or growing two separate processes from the cell body in the basal direction. Our observations suggest that both mechanisms might be occurring in human bRG. On the one hand, a cluster of anillin, a component of the cell cytokinesis machinery found at the basal process bifurcation site of mouse neuroepithelial cells (Kosodo et al., 2008), was readily found at the bifurcation site of human bRG-(a)b_{bf} (H, H'). On the other hand, thick growth cone-like structures could sometimes be observed at the distal ends of basal processes of human bRG-(a)b_{bf} (for a bRG-b_{bf} example, see Figure 2C"), suggesting an active basally directed growth mechanism. (H, H') DAPI staining and IF for HOPX and ANILLIN (ANLN) of bRG-

(a)b_{bf} in the OSVZ of 15-wpc hNcx. (H) Example of a cell with the basal process splitting nearby the cell body. (H') Example of a cell with the basal process splitting away from the cell body. Double arrows, bifurcation points with ANILLIN signal; arrows, two basal processes beyond the bifurcation point; arrowhead, apical process. All images are oriented with the apical side facing down. Images are two (H) or three (H') consecutive optical sections and are 25 µm wide. (H") Quantification of the position of the process splitting site in relation to the cell body of bRG-(a)b_{bf} determined using the cluster of anillin. Note that about half of the bRG-(a)b_{bf} split their basal process near the cell body and the other half away from the cell body. Of note, anillin spots were also present elsewhere in the cell including the cell body and as such cannot *per se* be used to predict process splitting sites.

(I-N) In 15-16–wpc hNcx, the vast majority of progenitors is neurogenic, and gliogenic progenitors are not yet abundant (Jakovcevski et al., 2009). To label the gliogenic progenitors in the OSVZ of 15-16–wpc hNcx, we performed an IF for the transcription factor OLIG2. (I) DAPI staining and IF for SOX2, HOPX and OLIG2. All images are oriented with the apical side facing down. (J) Percentage of SOX2+ and HOPX+ cells that are OLIG2+. Note that at this stage only 10% of proliferative BPs were gliogenic (K) Percentage of OLIG2+ cells that are SOX2+ and HOPX+. (L) Percentage of SOX2+ and HOPX+ cells that exhibit processes. (M) Distribution of mBP vs. bRG morphotypes of OLIG2+, SOX2+ and HOPX+ cells. Note that 60% of gliogenic progenitors exhibited a multipolar and 40% a radial morphology. (N) DAPI staining and IF for SOX2, HOPX and OLIG2 of a bRG-a and a mBP-p. All images are oriented with the apical side facing down. Arrowheads, cell body; arrows, processes. All images are 35 µm wide.

(A-E', G, I, N) MIPs (A, 37 optical sections; C, bRG-ab$_{bf}$ and mBP-p, 3 optical sections; D'; E; E'; I, 6 optical sections; N, 6 optical sections), SOpS (B; C, bRG-b_{bf}; D), StIs. Scale bars, 100 µm (D, G), 50 µm (A, B, E, I), 20 µm (D'), 10 µm (E').

(F, H", J-M) Mean of 2 (J-M), 4 (H", two 12-wpc and two 15-wpc hNcx) or 5 (F) experiments. Total number of cells scored: 58 (H"), 132 (L). Error bars, SD (F, H") or range (J-M).

Figure S2 Related to Figure 2. Quantitative analyses of BP morphotypes across different mammals.

(A-F) E13.5 mNcx, E33 fNcx and 10-13–wpc hNcx tissue were electroporated as detailed in Figure 2A-C.

(A, A') Example of cell tracking (segmentation). IF for mGFP (grey) of E15.5 mNcx. BPs in the SVZ and IZ were tracked and cell masks representing cell shape were generated (colored). (A) Overview. Box (100 µm x 100 µm), area shown at higher magnification in (A').

(B) Examples of BP process analysis. Cell masks representing cell shape of an E35 ferret mBP (left) and bRG-b (right) were generated by tracking the mGFP IF (see Figure 2B), and cell processes were analyzed using the Progenitors Process Analysis (PPA) software (see Methods). Red contour, cell soma; green, primary processes; dark blue, branches (secondary processes). Concentric circles with their midpoints at the center of the cell soma and gradually increasing by the soma radius (2r, 3r and 4r) were used for the Sholl analysis – the quantification of the number of process intersections with the concentric circles. List of parameters and measurements is given in the table on the right. Number of all processes equals the number of all primary processes plus all the branches. Branching index is calculated by dividing the number of all processes by the number of primary processes and can be 1.0 or higher. Additionally, the PPA software measures also the length of each process (not shown).

(C, D) DAPI staining and IF for mGFP and Ki67 (C) or Pax 6 (D) of E15.5 mNcx. Arrowheads, examples of mGFP+ BPs. (D right, low magnification panels, 30 µm wide), an mGFP+ Pax6+ radially-oriented cell indicated with arrowheads. Arrows, basal process; dashed line, cell body.

(E) Quantification of mBP branching expressed as the branching index (see B) per single mGFP-tracked mBP.

(F) DAPI staining and IF for GFP of a bRG-b_{bf} in 12-wpc hNcx. Arrows, basal processes; arrowhead, cell body. Note that one of the basal processes reaches the basal lamina.

(G-J) IF for Hopx to analyze bRG morphology and for Sox2 to identify proliferative BPs of E15.5 mNcx and 12-15–wpc hNcx, followed by analyses as indicated. (G) Distribution of the 5 bRG morphotypes in 12-15–wpc hNcx, as shown schematically on the right. Note that the distribution bRG morphotypes is comparable to the one obtained by mGFP tracking (compare to Figure 2F right). (H, I) DAPI staining and IF for Sox2 and Hopx of E15.5 mNcx. (H) Overview images. Arrows, example of a bRG-b; solid arrowheads, example of a bRG-a; open arrowheads, example of an mBP-p. (I) Three mouse bRG morphotypes. All images are oriented with the apical side facing down and are 50 µm wide. Dashed lines, cell contours; arrows, basal process; arrowheads, apical process. (J) Distribution of the three bRG morphotypes in E15.5 mNcx, as shown schematically on the right. Note that this analysis showed that indeed mouse lacks

bRG-b_{bf} and bRG-ab_{bf} and that the relative proportion of the other three bRG morphotypes is very similar to that obtained by mGFP tracking (compare to Figure 2F left).

(K-N) Analysis of mitotic BPs in mNcx. DAPI staining and IF for PhVim of E15.5 mNcx, followed by analyses as indicated. (K) Overview images. (L) Three mouse mitotic bRG morphotypes. Images are are 30 µm wide. (M) Distribution of mitotic bRG vs. mitotic mBP morphotypes in the SVZ+IZ of E15.5 mNcx (20 consecutive optical sections of 400-µm wide fields). Note that the proportion of mBPs and bRG is comparable to the one obtained by mGFP tracking reflecting BPs in all stages of the cell cycle (compare to Figure 2D left). (N) Distribution of three different mouse mitotic bRG morphotypes, as shown schematically on the right. Note that the distribution bRG morphotypes is comparable to the one obtained by mGFP tracking (compare to Figure 2F left) and by IF for Hopx (compare to Figure S2J), both reflecting BP at all stages of the cell cycle.

(O, P) Analysis of lamellate expansions in fNcx and hNcx. E33 fNcx and 10-13–wpc hNcx tissue were electroporated as detailed in Figure 2B, C. (O) IF for GFP of a bRG-b in 12-wpc hNcx. The cell shape as tracked by GFP IF is depicted in the right panel. Arrows, lamellate expansions extending from the cell soma and along the basal process. Image is 25 µm wide. (P) Percentage of bRG with lamellate expansions in E35 fNcx and 10-13–wpc hNcx.

(A, C, D, F, H, I, K, L, O) MIPs (A, 35 optical sections; F and K, 20 optical sections; I, 3 optical sections; L, 4 (bRG-b), 6 (bRG-a) and 7 (bRG-ab) optical sections; O, 5 optical sections), SOpS (H), StIs. Scale bars, 100 µm (A, K), 50 µm (H), 30 µm (F), 20 µm (C, D).

(E, G, J, M, N, P) Mean of 8 (E, mouse; M; N), 4 (E and P, ferret; J) 7 (E and P, human), 3 (G, one 12-wpc and two 15-wpc hNcx) experiments. Total number of cells scored: 197 (M), 169 (G), 80 (E, mouse), 43 (E, ferret), 48 (E, human), 29 (J), 19 (N). Error bars, CI (E, G, J, M, N) or SEM (P); **, P <0.01; *, P <0.05; n.s., not statistically significant; Student's *t*-test (E), 2-way ANOVA (P).

Figure S3 Related to Figure 3. The morpho-regulatory protein PALMD-CaaX induces BP process growth in mNcx and fNcx.

(A) mRNA expression of the *Palmdelphin* (*Palmd*) gene, analyzed by RNA-seq in mNcx and hNcx. RNA-seq data for germinal zones (upper panels) are from (Fietz et al., 2012) and for cell types (lower panels) are from (Florio et al., 2015). Developmental stages: E14.5 mouse (Fietz et al, 2012 and Florio et al, 2015); 12-13–wpc human (Florio et al, 2015), 13-16–wpc human

(Fietz et al, 2012). All the comparisons that are not marked by asterisks are not statistically significant. Note that in the hNcx, *PALMD* mRNA was most highly expressed in the ISVZ and OSVZ , and accordingly in bRG . In the mNcx, *Palmd* mRNA was found in both the VZ and SVZ, with the highest relative expression in APs.

(B-D) DAPI staining and IF for PCNA and Palmd of E15.5 mNcx (B), E36 fNcx (C) and 16-wpc hNcx (D).

(E) mRNA expression of the two *Palmd* isoforms, *Palmd-CaaX* and *Palmd-KKVI*, analyzed by RNA-seq in mNcx and hNcx. RNA-seq data are from (Florio et al., 2015). All the comparisons that are not marked by asterisks are not statistically significant. Note that in human progenitors both *PALMD* isoforms are present, whereas mouse progenitors virtually lack the expression of the PM-associated isoform (*Palmd-CaaX*).

(F-G) DAPI staining and IF for cadherin and Palmd of E15.5 mNcx (F) and 11-wpc hNcx (G); (G) shows a cell in the OSVZ. Arrowheads, lack of colocalization of cytoplasmic Palmd/PALMD with PM-bound cadherin; arrows, co-localization of PALMD with CADHERIN on the PM (human). Boxes (50 x 50 µm and 15 x 15 µm) in (F) and (F'), areas shown at higher magnification in (F') and (F''), respectively.

(H-Q) Analyses of mNcx (H-L, P left, Q) and fNcx (M-O, P right) upon IUE with mGFP and control or PALMD isoforms as indicated. (I-L, O, P) Quantification of processes of mouse and ferret BPs and APs as tracked by mGFP IF.

(H) DAPI staining and IF for GFP and PALMD of E15.5 mNcx upon PALMD-CaaX IUE as indicated. Boxes indicate areas shown at higher magnification in H'. (H') Arrows, co-localization of PALMD-CaaX and mGFP on the PM.

(I) Distribution of BP morphotypes.

(J) Quantification of mBP branching expressed as the branching index per single mBP.

(K) Sholl analysis of mBPs. Note that PALMD-CaaX induces preferentially short processes (2r distance).

(L) Histogram of the frequency distribution of process length upon control and PALMD-CaaX IUE. The length of all the processes tracked on 25 mBPs (Control) or 28 mPBs (PALMD-CaaX) were binned into 24 bins (X axis), with bin 1 indicating the shortest and bin 24 the longest processes. The number of processes in each bin is presented on the Y axis. Compared to control, PALMD-CaaX induces preferentially short processes (bins 2 - 6). Total number of processes scored: control 87, PALMD-CaaX 127.

(M) DAPI staining and IF for GFP and PALMD of E35 fNcx upon PALMD-CaaX IUE as indicated.
(N) DAPI staining and IF for GFP and Pax6 of E35 fNcx. Arrowheads, example of a bRG-a; double arrows, example of a bRG-ab. Higher magnification images (20 µm wide) of the indicated bRG are shown on the right; arrows indicate the process(es) of the bRG-a from the control condition (top) and the bRG-ab from the PALMD-CaaX condition (bottom).
(O) Quantification of mBP branching expressed as the branching index per single mBP.
(P) Quantification of AP (aRG, apical radial glia) morphotypes in interphase in E15.5 mNcx and E35 fNcx. Interphase cells were defined as those aRG whose cell body is located away from the ventricle. Confining the quantification to aRG in interphase allowed determining the effects of PALMD-CaaX expression on aRG morphology in steady state, while excluding changes in their morphology due to entry into mitosis. Note that all cells exhibit bipolar morphology (aRG-ab, shown schematically on the right) in both conditions in both species.
(Q) DAPI staining and IF for GFP, PhVim and PALMD in E15.5 mNcx upon PALMD-CaaX IUE as indicated. Arrows, PALMD-CaaX present in short processes that do not contain PhVim. Images are 30 µm wide. Note that similarly to interphase mBPs, PALMD-labeled processes of mitotic mBPs appeared to be short and relatively thin as they appeared to lack cytoplasmic PhVim immunoreactivity.
(B-D, F-H', M, N, Q) MIPs (B-D, 7 optical sections; H and H', 5 optical sections; M, 3 optical sections), SOpS (F-G, N, Q), StIs. Scale bars, 100 µm (H, M), 50 µm (B-D, F, N), 20 µm (F', H'), 10 µm (F'', G).
(A, E, I-L, O, P) Mean of 4 (E), 4-6 (A) biological replicates or 3 (L, P), 5 (O), 8 (I-K) experiments. Total number of cells scored: 88 (I, control), 87 (I, PALMD), 80 (J and K, control), 79 (J and K, PALMD), 31 (O, control), 34 (O, PALMD), 12 (P, mouse), 10 (P, ferret). Error bars, SD (A, E) or CI (I-K, O, P); ****, P <0.0001; ***, P <0.001; **, P <0.01; *, P <0.05; not statistically significant; two-way ANOVA(I, P), one-way ANOVA with Dunnett's multiple comparisons test (A), Student's *t*-test (E, J, K, O).

Figure S4 Related to Figure 4. **PALMD-CaaX promotes BP proliferation in mNcx and fNcx.**
Analyses of mNcx (A, DF) and fNcx (B, C) upon IUE with mGFP and control or PALMD isoforms as indicated.
(A) DAPI staining and IF for GFP, Ki67 and PhVim of E15.5 mNcx. Arrowheads, examples of GFP+ mitotic BPs.

(B) DAPI staining and IF for GFP and PH3 of E35 fNcx. Vertical arrows, examples of apical mitoses; horizontal arrows, examples of basal mitoses.

(C) Quantification of apical and basal mGFP+ PH3+ mitoses.

(D) Quantification of apical mGFP+ PH3+ mitoses (see Figure 4H for microscopy images).

(A, B) SOpS, StIs. Scale bars, 20 μm.

(C, D) Mean of 5 (C), 8 (D, control and PALMD-CaaX), 4 (D, PALMD-KKVI and PALMD-Δ) experiments. Error bars indicate SD; *, P <0.05; n.s., not statistically significant; Mann-Whitney *U*-test.

Figure S5 Related to Figure 5. **PALMD is required for BP process growth and proliferation in hNcx.**

(A) hNcx tissue was electroporated *ex vivo* with mGFP and soluble GFP, kept in culture and incubated in the absence (DMSO) or presence of 2BrPal as indicated in Figure 5E. Analysis of the 5 bRG morphotypes, as shown schematically on the right.

(B) Schematic representation of the transcribed region of the *PALMD* gene. Green boxes, exons; green arrow, transcription start site (TSS); orange box, differentially spliced last protein-coding exon (CaaX or KKVI). Bottom schemes show magnifications of the three regions of *PALMD* with the positions of the individual gRNAs (cr1-7, red). Cr1 guides cutting in intron 1 (I1), cr2 in exon 4 (E4) and cr3-7 in exon 7 (E7).

(C) Agarose gel showing the effects of the gRNAs cr1-7 described in (B) to direct Cas9-mediated cutting of three *PALMD* PCR products *in vitro*. PCR1, PCR2 and PCR3-7 indicate template-only control with no gRNA added (cr1, cr2, cr3, respectively); M, DNA size marker. gRNAs selected for the *ex vivo* experiments are: cr1 (located most 5' within the *PALMD* gene, which increases the probability of obtaining disruption of gene expression), cr2 and cr3 (both have stronger efficiency of cutting the respective PCR product according to the *in vitro* test presented than cr4-7).

(D -J) hNcx tissue was electroporated *ex vivo* with mGFP and soluble GFP together with plasmids encoding *Cas9_T2A_RFP* and gRNA targeting either *LacZ* (Control) or *PALMD* (PALMD KO), as indicated.

(D) DAPI staining and IF for PALMD and RFP (reflecting Cas9) of 11-wpc hNcx. Dashed lines, cell outline reflecting the region of interest (ROI) used for the quantification of IF intensity; yellow arrowheads, lack of PALMD signal on the PM of the Cas9+ cell; white arrowheads,

PALMD signal on the membrane of a Cas9– cell. Upper two images are 50 µm wide. Box (10 µm wide), area shown at higher magnification below.

(E) Quantification of PALMD immunoreactivity, measured as mean pixel intensity value per RFP+ SVZ cell. The mean of the data points of the control condition was set to 100%, and the data points of the KO condition were expressed relative to this. Each data point indicates the average value obtained per one tissue section.

(F, G) Analysis of cell death. (F) DAPI staining and IF for GFP and active CASPASE-3. (G) Quantification of cell death, shown as abundance of active CASPASE-3+ cells in a 200 µm-wide field. Note that the present approach of *ex vivo* manipulation did not cause an increase in cell death.

(H) Quantification of the efficiency of electroporation, shown as abundance of Cas9+ cells in a 200 µm-wide field. Note that the present approach of *ex vivo* manipulation was equally efficient for both PALMD KO and control constructs.

(I, J) Quantification of processes of BPs as tracked by mGFP IF. (I) Distribution of bRG vs. mBP morphotypes. (J) Quantification of mBP branching expressed as the branching index per single mBP.

(D, F) SOpS , StI (F). Scale bar, 100 µm (F).

(A, E, G-J) Mean of 7 (H), 6 (I, J), 5 (G), 3 (A, E) experiments. Total number of cells scored: 66 (I, control), 59 (I, PALMD KO), 35 (J, control), 31 (J, PALMD KO), 33 (A, control), 25 (A, 2BrPal). Error bars, CI (A, I, J) or SD (G, H); ***, P <0.001; n.s., statistically not significant; two-way ANOVA (A, I), Mann-Whitney *U*-test (E), Student's *t*-test (G, H, J).

Figure S6 Related to Figure 6. **Specificity of PALMD and identification of adducin 3 as essential component in the PALMD-induced increase in BP processes.**

(A-D) Analysis of specificity of PALMD-CaaX on BP morphology and BP proliferation. To examine if another paralemmin was able to recapitulate the effects of PALMD-CaaX on BP morphology and proliferation, we focused on Palm1, the founding member of this family, which also contains a CaaX domain (Kutzleb et al., 1998). As Palm1 is expressed in mouse BPs (A), we used the Palm1 KO mouse line (Albrecht et al., 2013). Our analyses (B) showed that Palm1 is not required to maintain the normal levels of mBP process number (C) and of BP proliferation (D) in mNcx. Hence, although Palm1 has been shown to promote cell process formation in neurons (Gauthier-Campbell et al., 2004; Kutzleb et al., 1998), its lack of effects

in mouse BPs suggests that the ability of human PALMD-CaaX to promote BP process growth and proliferation may well be a specific feature of PALMD-CaaX. (A) mRNA expression of the *paralemmin 1* (*Palm1*) gene, analyzed by RNA-seq in mNcx. RNA-seq data are from (Florio et al., 2015). (B-D) Wild type and homozygous Palm1 KO mNcx upon IUE of mGFP at E13.5, followed by analysis at E15.5. (B) DAPI staining and IF for GFP and Ki67. Boxes (30 µm x 30 µm), areas shown at higher magnification on the right. Arrows, cell processes. (C) Quantification of primary processes per single mBP. (D) Percentage of mGFP+ cells in SVZ+IZ that are Ki67+.

(E-J) Identification of adducin 3 as essential component in the PALMD-induced increase in BP processes. (E) mRNA expression of the *adducin3* (*Add3*) gene, analyzed by RNA-seq in mNcx and hNcx. RNA-seq data for germinal zones (upper panels) are from (Fietz et al., 2012) and for cell types (lower panels) are from (Florio et al., 2015). Note that in mNcx *Add3* mRNA is found in only low quantities and mostly in the VZ and in aRG, whereas in hNcx, *ADD3* mRNA is highly expressed in the VZ, ISVZ and OSVZ and in both aRG and bRG, that is, in the most proliferative zones and cell populations of these two species. (F) DAPI staining and IF for Palmd and adducin-γ (Add3) of E15.5 mNcx. Asterisks, background staining in the IZ. (G) DAPI staining amd IF for Add3 of OSVZ of E37 fNcx. Box, area shown at higher magnification in (G'). Note that Add3 was observed at the cell periphery, consistent with an association with the PM. (H) Entire immunoblots, using anti-PALMD (left) and anti-ADD3 (right) antibodies, of 12-wpc hNcx tissue immunoprecipitates (IP) obtained using control, anti-PALMD and anti-ADD3 antibodies. Arrowheads, PALMD band (left) and ADD3 band (right); arrows, IgG heavy chain; double arrows, IgG light chain. Note that a cropped section of this immunoblot is shown in Figure 6B. (I, J) hNcx tissue was electroporated *ex vivo* with mGFP together with plasmids encoding *Cas9_T2A_GFP* and gRNA targeting either *LacZ* (Control) or *ADD3* (ADD3 KO), as indicated. (I) DAPI staining and IF for GFP (reflecting Cas9), Ki67 and ADD3. (J) Quantification of ADD3 immunoreactivity, measured as mean pixel intensity value per GFP+ SVZ cell. The mean of the data points of the control condition was set to 100%, and the data points of the KO condition were expressed relative to this. Each data point indicates the average value obtained per one tissue section.

(B, F-G', I) SOpS, StIs (B, F, I). All images are oriented with the apical side facing down. Scale bars, 50 µm (F), 20 µm (B, G, I), 10 µm (G').

(A, C-E, J) Mean of 3 experiments (C, D, J) or 4-6 biological replicates (A, E). Total number of cells scored: 17 (C, control and Palm1KO). Error bars, SD (A, D) or CI (C); **, P <0.01; n.s., not statistically significant; Student's *t*-test (C), Mann-Whitney *U*-test (D, J).

Figure S7 Related to Figure 7. The PALMD-CaaX–promoted increase in BP proliferation requires integrin-β1.

(A, B) Analyses of mNcx upon IUE with mGFP and control or PALMD-CaaX as indicated. DAPI staining and IF for GFP and phospho-Akt (pAkt, A) or phospho-ERK (pERK, B). Boxes in (A) (50 µm x 50 µm) and the numbered boxes in (B) (30 x 30 µm), areas shown at higher magnification below respective panels. Arrows, pAkt signal in the process of a GFP+ cell (A), arrowheads, pAkt (A) and pERK (B) signal in the cell body of a GFP+ cell. Immunoreactivity is quantified in Figure 7C.

(C-E) Analyses of mNcx upon IUE with mGFP and PALMD-CaaX together with a plasmid encoding either scrambled shRNA (Control) or shRNA targeting *Itgb1* as indicated. (C, D) DAPI staining and IF for GFP and Itgb1. (C) Overview images. (D) Images of electroporated areas. In (C), the dashed lines indicate the center of the electroporated area; note the reduced Itgb1 signal in the electroporated area and the stronger Itgb1 signal outside (to the left) of the electroporated area; asterisks, Itgb1 staining of blood vessels. (E) Quantification of Itgb1 immunoreactivity, determined as described in Methods.

(F, G) 12–wpc hNcx tissue was kept in culture for one day and subsequently incubated for one day with Itgb1-blocking antibody (P5D2) as described in Methods. (F) DAPI staining and IF for PCNA. (G) Quantification of PCNA+ cells in both germinal zones (GZ, left), in the VZ (middle) and in the SVZ (right).

(A-D, F) SOpS, StIs. Scale bars, 100 µm (C), 50 µm (F), 20 µm (A, B, D).

(E, G) Mean of 4 (E) or 3 (G) experiments. Error bars, SD; ***, P <0.001; **, P <0.01; Mann-Whitney *U*-test (E), Student's *t*-test (G).

Table S1 Related to Figure 3. Genes enriched in the fetal human OSVZ/ISVZ vs. VZ.

List of the 25 genes with at least 10-fold greater mRNA expression in the fetal human OSVZ and ISVZ than the VZ (Fietz et al., 2012). The list comprises Ensembl Gene IDs, gene names and average FPKM values in VZ, ISVZ, OSVZ and CP. Genes are listed in descending order by the fold-increase OSVZ/VZ. Seven genes related to cell morphology are highlighted in green.

Table S2 Related to Figure 6. List of PALMD interactors in hNcx, fNcx and mNcx.

Upper part. List of the proteins, with their respective gene name and molecular weight (MW), identified by MS in the three PALMD IPs (Exp. 1-3) and in neither of the control IPs from hNcx. For each protein and experiment, the number of unique peptides (UP) and the number of total spectra (TS) are given. Proteins are listed in descending order by their average UP number in the three experiments. The last two columns indicate whether the specific orthologue was found in the PALMD IP from fNcx (Ferret IP) or mNcx (Mouse IP), but not in the respective control. Members of the adducin family are highlighted in green, and the bait, PALMD, is highlighted in blue.

Lower part. List of the top (see below) 13 proteins identified by MS in the Palmd IPs, but not in the control IPs, from fNcx (left) and mNcx (right). For each protein, the respective gene name, molecular weight (MW) and the number of unique peptides (UP) are given. Proteins are listed in descending order by the number of UPs. Note that the bait, Palmd, matched with lower number of UPs than the presented proteins, but it was specifically detected in Palmd but not control IP from both fNcx and mNcx. Note also that Add3 was not detected in the IP from mNcx.

Table S3 Related to STAR Methods. List of oligonucleotides used.

Movie S1

Click here to access/download

Supplemental Videos and Spreadsheets

Supplemental movie S1.mp4

Movie S2

Click here to access/download

Supplemental Videos and Spreadsheets

Supplemental movie S2.mp4

Movie S3

Click here to access/download

Supplemental Videos and Spreadsheets

Supplemental movie S3.mp4

Movie S4

Click here to access/download

Supplemental Videos and Spreadsheets

Supplemental movie S4.mp4